

UNIVERSITY OF OKLAHOMA
GRADUATE COLLEGE

BIOPHYSICAL INVESTIGATIONS OF THE THREE-WAY JUNCTION IN PHI29-
LIKE BACTERIOPHAGE PROHEAD RNA

A DISSERTATION
SUBMITTED TO THE GRADUATE FACULTY
in partial fulfillment of the requirements for the
Degree of
DOCTOR OF PHILOSOPHY

By
ALYSSA C. HILL
Norman, Oklahoma
2017

BIOPHYSICAL INVESTIGATIONS OF THE THREE-WAY JUNCTION IN PHI29-
LIKE BACTERIOPHAGE PROHEAD RNA

A DISSERTATION APPROVED FOR THE
DEPARTMENT OF MICROBIOLOGY AND PLANT BIOLOGY

BY

Dr. Susan Schroeder, Chair

Dr. Laura Bartley

Dr. Anne Dunn

Dr. Douglas Gaffin

Dr. Scott Russell

© Copyright by ALYSSA C. HILL 2017
All Rights Reserved.

Acknowledgements

I thank Prof. Susan Schroeder for her unwavering support and guidance during my doctoral studies. Prof. Schroeder has been an outstanding mentor to me not only as a scientist, but also as a young woman. I am inspired equally by her enthusiasm for science, her dedication, and her kindness, and I am looking forward to many more exciting conversations about RNA, about travel, and about life.

I thank the past and present members of the Schroeder Lab, especially Dr. Xiaobo Gu, who provided invaluable insight into many of my early experiments on pRNA, and Andy Phan, who contributed to my knowledge of UV optical melting.

I thank Prof. Kelly Standifer, without whom the work presented in Chapter 4 would not be possible. Prof. Standifer provided the NG108-15 cells for uptake studies, and on more than one occasion, Prof. Standifer generously provided her time and insight to help me design my cell experiments, which were performed in her lab. I am grateful to have had the privilege of working in the Standifer Lab and for the opportunity to cultivate new skills. I also thank Cindy Simpson-Durand and Hannah Taff for their patience and help in growing cells for these experiments, and Prof. Dr. Hibah Awwad for her assistance with cells and for lovely conversations during our late nights in the lab.

I thank Greg Strout for his significant contribution to the transmission electron microscopy (TEM) work presented in Chapter 5. Greg devoted countless hours to teaching me microscopy and to the project of visualizing small RNAs using TEM, and I am grateful to have had his technical expertise and his patience in this endeavor. The results presented on a helix-extended 3WJ would not be possible without his efforts. I

also thank Prof. Scott Russell for his insights into my TEM experiments. I am thankful to both Greg and Prof. Russell for their pleasant company and conversation, which often were the highlight of my time in the microscopy lab.

I thank Prof. Laura Bartley for her mentorship in the later stages of my graduate career. Prof. Bartley generously gave of her time and keen insight into RNA to help support some of my final experiments, and I am grateful for her guidance and example as a woman in science.

I also am grateful to the Office of Technology Development at the University of Oklahoma. In particular, I would like to extend a sincere thank you to James Bratton and Dr. Christopher Corbett for their support and encouragement.

Finally, I thank Prof. Paul Sims, who I am fortunate to call both a mentor and a friend. Prof. Sims has been an invaluable source of support during my pre-doctoral and doctoral studies, and I cannot express enough gratitude for the conversations we have shared, about life and travel, about science, and perhaps most importantly, about books! I look forward to many more.

Table of Contents

Acknowledgements	iv
Table of Contents	vi
List of Tables	xi
List of Figures.....	xii
Abstract.....	xiv
Chapter 1: Introduction.....	1
Overview	1
Significance of the pRNA 3WJ	2
Towards a Better Understanding of 3WJ Stability.....	5
References	8
Chapter 2: Prohead RNA: A Noncoding Viral RNA of Novel Structure and Function. 13	
Abstract.....	13
Φ29-like Bacteriophages	13
The Φ29-like Phage Packaging Motor	16
Overview of the Packaging Motor	16
Structures of the Packaging Motor Protein Components	19
Prohead RNA.....	20
Prohead RNA Primary and Secondary Structure	20
Prohead RNA Tertiary Structure and Function	23
Prohead RNA Self-Association.....	25
Prohead RNA Interlocking Loops	25
Prohead RNA Multibranch Loop	27

Applications and Future Directions.....	28
Prohead RNA in Nanobiotechnology.....	28
Unanswered Questions.....	29
Conclusion.....	30
References.....	32
Chapter 3: Thermodynamic Stabilities of Three-Way Junction Nanomotifs in Prohead	
RNA.....	41
Abstract.....	41
Introduction.....	41
Results.....	45
pRNA 3WJ Nanomotif Stabilities.....	45
Metal Ion Binding.....	49
Electrophoretic Gel Mobility Shift Assays.....	49
Discussion.....	51
3WJ Stabilities in Relation to Loop-Loop Interaction Stabilities and Self- Assembly.....	51
Structure-Energetics Relationships in the pRNA 3WJ.....	53
Future Improvements in Predicting RNA 3WJ Stabilities.....	56
Materials and Methods.....	57
pRNA 3WJ Construct Design.....	57
UV Optical Melting.....	58
pRNA 3WJ Secondary Structure and Free Energy Predictions.....	60
Electrophoretic Gel Mobility Shift Assays.....	61

References	62
Chapter 4: Phi29-Alternative 3WJs as Viable Candidates in the	68
Development of Nanoparticles for Therapeutic Drug Delivery	68
Abstract.....	68
Introduction	69
Results	71
Stabilities of 3WJs in Human Blood Serum.....	71
Uptake of 3WJs in Neuroblastoma Cells.....	73
Discussion.....	74
Stabilities of 3WJs in Human Blood Serum.....	74
Serum Stabilities in Relation to Metal Ion Binding and Structure.....	77
Cellular Uptake of 3WJs	78
Cellular Uptake Over Time	80
Other Factors Affecting Cell Uptake.....	82
Future Prospects for Improving Cell Uptake and Specificity	82
Conclusion.....	83
Materials and Methods	83
Serum Stability Assays.....	83
Cellular Uptake Assays	85
Statistical Analysis	86
References	87
Chapter 5: Preliminary Investigations of pRNA 3WJ Conformation Using Transmission	
Electron Microscopy	94

Abstract.....	94
Introduction	94
Results	97
3WJ Helix-Extended Construct Design and Initial Characterization.....	97
3WJ Conformation Predictions Using Junction Explorer	99
Electrophoretic Mobility Shift Assay.....	100
3WJ Helix Lengths and Interhelical Angles.....	101
Discussion.....	102
Helical Coaxial Stacking Predictions	102
Helical Arrangement in the Phi29HE _{DNA} 3WJ.....	103
Limitations and Future Directions for Determining 3WJ Conformation	105
Conclusion	106
Materials and Methods	106
Helix-Extended 3WJ Construct Design.....	106
Secondary Structure and Family/Helical Coaxial Stacking Predictions	107
Dynamic Light Scattering (DLS)	108
Electrophoretic Mobility Shift Assays	108
Transmission Electron Microscopy	108
References	110
Chapter 6: Conclusion	114
References	119
Appendix I.....	122

Supplementary Information for “Thermodynamic Stabilities of Three-Way Junction Nanomotifs in Prohead RNA”	122
Appendix II.....	132
Supplementary Information for “Preliminary Investigations of pRNA 3WJ Conformation Using Transmission Electron Microscopy”	132
References	137

List of Tables

Chapter 3

Table 1 Thermodynamic parameters for 3WJs	46
-------------------------------------------------	----

Chapter 4

Table 1 Endoribonuclease cut sites in 3WJs	78
--------------------------------------------------	----

Chapter 5

Table 1 Diameters of the phi29 and phi29HE _{DNA} 3WJs	100
----------------------------------------------------------------------	-----

Table 2 Family and helical coaxial stacking predictions for the phi29 and phi29HE _{DNA} 3WJs	101
----------------------------------------------------------------------------------------------------------------	-----

Appendix I

Table 1 Comparison of 3WJ predicted and experimental free energies	126
--------------------------------------------------------------------------	-----

Table 2 Thermodynamic parameters for 3WJs with metal ions	127
-----------------------------------------------------------------	-----

Table 3 Calculated ΔG_{37} and ΔH values for possible species formed by phi29, SF5, and M2 strands 3WJa, 3WJb, and 3WJc	130
--------------------------------------------------------------------------------------------------------------------------------------------------	-----

Appendix II

Table 1 Diameters of 3WJs	134
---------------------------------	-----

Table 2 Sequences for phi29HE _{DNA} component strands 3WJa, 3WJb, and 3WJc ..	135
----------------------------------------------------------------------------------------	-----

Table 3 Predicted free energies for phi29HE _{DNA}	136
------------------------------------------------------------------	-----

Table 4 Family and helical coaxial stacking predictions for 3WJs	137
------------------------------------------------------------------------	-----

List of Figures

Chapter 1

Figure 1 Primary, secondary, and tertiary structure of phi29 pRNA	4
-------------------------------------------------------------------------	---

Chapter 2

Figure 1 Phylogenetic tree for Φ 29-like bacteriophages	15
--------------------------------------------------------------------	----

Figure 2 Representation of the orientation of Φ 29 motor components	17
--------------------------------------------------------------------------------	----

Figure 3 Secondary structure of Φ 29 pRNA	22
------------------------------------------------------	----

Figure 4 Ball-and-stick model of pRNA	26
---------------------------------------------	----

Chapter 3

Figure 1 pRNA 3WJ constructs' primary and secondary structures	44
----------------------------------------------------------------------	----

Figure 2 Example melt curve and van't Hoff plot	47
-------------------------------------------------------	----

Figure 3 Measured stabilities and free energy predictions for 3WJs	49
--------------------------------------------------------------------------	----

Figure 4 Metal ion effects on 3WJs	50
------------------------------------------	----

Figure 5 Gel mobility of 3WJs	51
-------------------------------------	----

Figure 6 Interlocking loops and 3WJ stabilities	53
-------------------------------------------------------	----

Figure 7 Structure of the phi29 3WJ	56
-------------------------------------------	----

Chapter 4

Figure 1 Serum stabilities of 3WJs	73
------------------------------------------	----

Figure 2 Time-resolved serum stabilities of the phi29 and M2 3WJs	74
-------------------------------------------------------------------------	----

Figure 3 Cell uptake of 3WJs	76
------------------------------------	----

Figure 4 Uptake of single-stranded RNA and 3WJ	77
------------------------------------------------------	----

Figure 5 Family and helical coaxial stacking predictions for 3WJs	82
-------------------------------------------------------------------------	----

Chapter 5

Figure 1 Helix-extended phi29 3WJ construct	98
Figure 2 Gel mobility of phi29HE _{DNA}	101
Figure 3 Interhelical angles in the phi29HE _{DNA} 3WJ	102
Appendix I	
Figure 1 Single stranded optical melting data	124
Figure 2 Pairwise optical melting data	125
Figure 3 Gel mobility of 3WJs in TMS buffer	128
Figure 4 Possible species formed by phi29, SF5, and M2 strands 3WJa, 3WJb, and 3WJc	129

Abstract

The knowledge gained from biophysical studies of RNA can contribute to basic research and inform new directions for translational research. In particular, information that develops the relationships among RNA energetics, physiologic stability, and structure can contribute to better predictions of RNA structure from sequence and guide the rational design of functional supramolecular structures such as targeted therapeutics. A conserved three-way junction (3WJ) in noncoding viral prohead or packaging RNA (pRNA) uniquely captures many aspects of RNA structure and function and represents a model system for studying these relationships. This dissertation presents thermodynamics for pRNA 3WJs. Phylogenetically related 3WJs have a wide range of thermodynamic stabilities, and some sequences are more stable than a phi29 3WJ sequence that is used commonly in RNA nanotechnology. The range of thermodynamic stabilities observed is not explained fully by differences in sequence at the 3WJ core.

The prototype phi29 pRNA sequence is used commonly in nanotechnology, for example as a nanoparticle delivery vector for therapeutic drugs. Related sequences are underexplored. The successful translation of phi29-alternative 3WJs into clinical practice will depend on energetic stability and the ability to overcome several key physiological barriers. This dissertation also presents 3WJ stabilities in human blood serum and in cells. Energetic and physiologic stabilities are not always correlated, but some 3WJs are both more thermodynamically stable and more stable in serum than the phi29 3WJ. The results of cell uptake studies support the idea that phi29-alternative 3WJs may be useful in nanotechnology, for example, in stabilizing RNAs for drug delivery.

The coaxial stacking of helices across RNA 3WJs can be thermodynamically favorable and may account for some of the observed differences in 3WJ stabilities. Transmission electron microscopy (TEM) data for a helix-extended construct indicate that helices are distributed equally around the phi29 3WJ. The determination of the relative orientation of helices around the pRNA 3WJ can help shed light on how sequence and secondary structure at the 3WJ core influence global structure and may provide insight into why some 3WJs are more energetically and physiologically stable than others.

The work presented here contributes to parameters for better RNA structure prediction from sequence, expands the number of useful building blocks for RNA nanotechnology, and provides a method for further investigating structural mechanisms underlying pRNA stability and self-assembly.

Chapter 1: Introduction

Overview

Ribonucleic acid (RNA) is a fascinating and dynamic molecule. With the discovery of catalytic RNA in the early 1980s¹⁻², the passive role of RNA as codified by the Central Dogma of Molecular Biology³ was reimagined. Today, it is known that RNA is a key player in many processes associated with cellular life⁴. Ribozymes, riboswitches, small RNAs, and long noncoding RNAs are active in genome replication⁵, intron splicing⁶, metal ion sensing⁷, regulation of operons and gene expression⁸, and epigenetic modification and scaffolding⁹⁻¹⁰. New structural and functional roles for RNA are discovered at an accelerating pace, and at the same time, the diverse landscape of the natural RNA World inspires the design of novel systems with applications in nanotechnology and medicine. Recent engineering of CRISPR, an ancient form of RNA-based microbial immunity, has transformed thought on human health and disease with its potential for robust gene editing¹¹⁻¹³, and this year may see the first use of synthetic small interfering RNA (siRNA) as a therapeutic drug¹⁴. Indeed, the current frontier of RNA research illustrates that now is an exciting time to study RNA.

Certain natural systems may be uniquely positioned to impact both basic and translational RNA research. The prohead or packaging RNA (pRNA) of phi29-like bacteriophages is a model system at the nexus of biology and engineering. The indispensable function of pRNA in the phi29 viral molecular motor¹⁵ and its use as a building block in nanotechnology¹⁶⁻¹⁷ are highlighted below. In particular, a three-way junction (3WJ) that is a conserved substructure among phylogenetically related pRNAs¹⁸ offers a unique setting in which to study the relationships among RNA structure,

energetics, and function. Because the 3WJ is critical to the activity of the phi29 molecular machine ¹⁹⁻²⁰ and an important determinant of the stability and self-association properties ²¹⁻²² that are leveraged in pRNA-based nanotechnology, studies on the 3WJ can provide important information for guiding basic RNA research and for effectively leveraging pRNA as a nano-scale tool. Following is an introduction to pRNA, the pRNA 3WJ, and the motivations for investigating 3WJ stability and structure.

Significance of the pRNA 3WJ

Bacteriophages are viruses that infect bacteria. In the phi29-like family of bacteriophages, pRNA is an unusual but required component of a motor that packages genomic double-stranded DNA during viral replication in host *Bacillus* spp. ¹⁵. It is hypothesized that the role of pRNA has been assumed by a protein in other motors ²³⁻²⁴, making pRNA a ‘molecular fossil’ of an RNA World ²⁵. The phi29 motor comprises three concentric ring assemblies of connector proteins, pRNAs, and ATPases, which harness chemical energy in order to power encapsidation of the viral genome. It is suggested that in this context, pRNA absorbs stress imposed by moving parts in the motor and facilitates communication between the other motor components ²⁶. Although the particular role of pRNA in the phi29 motor remains to be determined, it is known that certain structural elements are critical to motor function. In particular, changes at the pRNA 3WJ can abolish packaging activity ²⁰, implicating the 3WJ as an important contributor to the role of pRNA *in vivo*.

Removed from its natural context in the packaging motor, pRNA is leveraged as a molecular ‘building block’ in nanotechnology. Base pairing between interlocking or

'kissing' loops in adjacent pRNA molecules permits their self-assembly into discrete shapes, such as rods ¹⁶ and prisms ²⁷, and certain studies have conceived these novel nanostructures as vehicles for diagnostic agents and therapeutic payloads, for example siRNAs directed against oncogenes in cancer cells ²⁸⁻²⁹. Recent studies have revealed that by correctly positioning the kissing loops in three-dimensional (3D) space, the pRNA 3WJ dictates the diverse self-association behaviors of related pRNAs ²¹⁻²². Additionally, when it is removed from the surrounding pRNA architecture, the 3WJ itself is a modular building block that can be functionalized with targeting and therapeutic moieties ³⁰. Thus, studies on the pRNA 3WJ can provide knowledge for guiding the rational design of functional supramolecular structures.

Figure 1 shows the primary and secondary structures of the prototype phi29 pRNA and the tertiary structure of the phi29 3WJ as determined by X-ray crystallography ³¹. RNA structure is defined on the primary, secondary, and tertiary levels, where an overall architecture is the result of hierarchical folding that tends to minimize free energy ³²⁻³³. Primary structure is the nucleotide sequence of an RNA. Watson-Crick base pairing between nucleotides forms RNA helices, while non-Watson-Crick base pairs maintain interspaced single-stranded motifs, such as hairpins, bulge loops, and junctions ³⁴⁻³⁵. A collection of these structural elements represented in two-dimensional space comprises an RNA secondary structure that may form additional stabilizing interactions (*i.e.*, tertiary structure) in 3D.

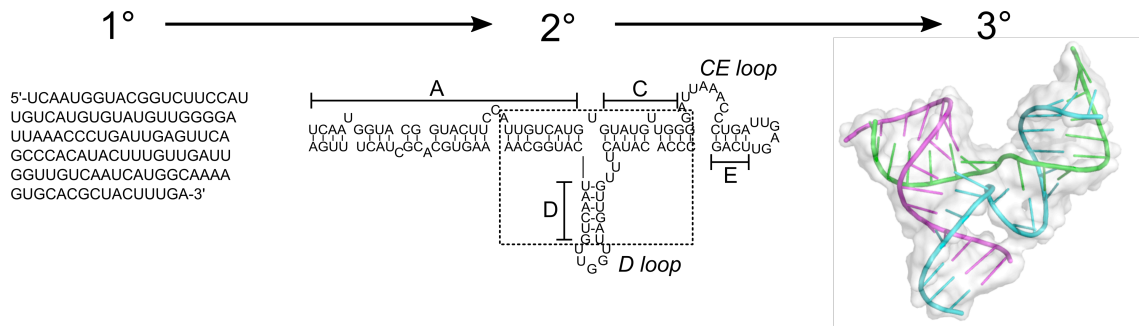


Figure 1 The primary (1°) structure of phi29 pRNA folds into a secondary (2°) structure¹⁸ comprising helices A, C, D, and E (labeled); interlocking CE and D loops (labeled); and a three-way junction, or 3WJ (boxed). A surface and cartoon rendering of the tertiary (3°) structure of the phi29 pRNA 3WJ (PDB ID: 4KZ2) determined to 3.05 Å by X-ray crystallography³¹ is shown.

The prototype phi29 pRNA sequence is 174 nucleotides (nt) long and folds into a secondary structure that is conserved among the members of its family¹⁸. A 120-nt construct that supports wild-type levels of packaging in the phi29 motor is used widely for *in vitro* studies³⁶ and is described here. Although related pRNAs are only 12% similar by sequence³⁷, they share a secondary structure that can be defined broadly by helices A, CE, and D; interlocking or kissing CE and D loops; and a three-way junction (3WJ)³⁸ (Figure 1). Three-way junctions are common motifs in RNA secondary structure that help achieve important RNA functions, such as catalysis in the hammerhead ribozyme³⁵. However, 3WJ structures are difficult to predict from sequence, and they become increasingly difficult for larger junctions with unpaired nucleotides³⁹. In pRNA, the 3WJ is hypothesized to balance the opposing demands of conformational flexibility and structural rigidity imposed on pRNA by the phi29 packaging motor²⁰. The putative roles of the 3WJ in pRNA self-association and in influencing the global structure of pRNA are described in more detail below. The biophysical study of the 3WJ can contribute to the development of new hypotheses

surrounding structure-energetics-function relationships, contribute to parameters for RNA secondary structure prediction from sequence, and establish new building blocks in the design of functional supramolecular structures.

Towards a Better Understanding of 3WJ Stability

The 3WJ is important for pRNA assembly, which may be reasonably visualized as hand-in-hand interactions, for example, among two, three, or more individuals around a ring⁴⁰. In this analogy, hand-in-hand interactions are base pairs that form between the interlocking CE and D loops of pRNA. Owing to the great sequence diversity among pRNAs, the number and character of the base pairs that form between the CE and D loops are different depending on the pRNA sequence. A recent study showed that despite these differences, the energetics of dimerization are conserved across related pRNAs³⁷. One hypothesis is that differences in loop-loop interaction energetics are counterbalanced by differences in energetics at the 3WJ core. UV optical melting is a robust method for determining thermodynamics and is used commonly to study RNA duplexes⁴¹. Chapter 3 describes a tripartite system for investigating the energetics of pRNA 3WJs using UV optical melting and reveals that related 3WJs have different thermodynamic stabilities. While for some pRNAs, 3WJ stabilities offset loop-loop stabilities, for others, both the 3WJ and loop-loop interactions are stabilizing. The combination of stabilizing interactions may contribute to the self-association behavior of certain pRNA sequences.

As a standalone structure, the pRNA 3WJ can be leveraged as a building block in nanotechnology, and its use in this capacity is enabled in part by its thermodynamic stability³⁰. An RNA-based drug delivery vector, for example, must stay intact at body

temperature. A nanoparticle system based on the prototype phi29 3WJ has been developed and used successfully at the proof-of-concept level, such as in the targeting and treatment of cancer cells ⁴²⁻⁴⁴. To date, only the phi29 sequence has been evaluated in the bottom-up fabrication of supramolecular structures, and related 3WJs are comparatively underexplored. It is suggested that the rich sequence and energetic diversity among pRNA 3WJs may contribute to the development of new nanoparticle systems for therapeutic drug delivery ⁴⁵. However, the translation of 3WJs into clinical practice will hinge on their abilities to overcome key physiological barriers, such as degradation by nucleases in the blood and cell uptake. Chapter 4 describes studies that tested a possible correlation between 3WJ energetic and physiologic stabilities. Although energetic and physiologic stabilities are not always correlated, certain 3WJs are both thermodynamically stable and stable in human blood serum. Additionally, 3WJs enter and accumulate in cells to 20% over 24 hours. Uptake by specific cells is promoted with RNA functionalization, such as with homing molecules appended to the 3WJ; therefore, minimal uptake of a ‘naked’ 3WJ may translate to greater specificity in uptake following its functionalization.

As discussed above, the 3WJ is critical for the packaging activity of the phi29 viral molecular machine and is an important determinant of the stability and self-association of pRNA, which are leveraged in nanotechnology. An underlying structural mechanism may help explain these features. RNA 3WJs typically adopt a conformation such that two helices leading into the junction form a coaxial stack, or ‘superhelix’, while the third helix is positioned at an angle to the stack ³⁵. It is suggested that a coaxial stack between helices A and D maintains the functional form of pRNA in the

phi29 motor²⁰. Indeed, two crystal structures of the phi29 3WJ indicate the formation of an A/D superhelix^{31,46}, and interruption of this structure abolishes packaging activity²⁰. In solution, related 3WJs have different thermodynamic stabilities⁴⁵ and different propensities for self-assembly^{21,37} that may be explained partially by differences in helical coaxial stacking. Recent results support the hypothesis that the *in vitro* conformation of certain 3WJs predisposes pRNA to self-association²². Chapter 5 describes preliminary studies on a 3WJ system designed for the direct measurement of A, CE, and D interhelical angles in a phi29 3WJ using transmission electron microscopy (TEM). In line with previous data for the phi29 3WJ in solution²², the presented TEM data reveal that helices A, CE, and D are distributed evenly around the junction. This method may be extended to related 3WJs in order to fully examine the hypothesis that conformation differs across pRNA 3WJs and develop the relationship between 3WJ energetics and structure.

The vast structural and functional landscapes of RNA and the current frontier of RNA research highlight that now is an exciting time to study RNA. A three-way junction (3WJ) nanomotif conserved in viral prohead or packaging RNA (pRNA) offers a unique system for developing knowledge that may have implications beyond the laboratory. In particular, biophysical studies aimed at understanding this 3WJ can contribute to the development of new hypotheses surrounding structure-energetics-function relationships, contribute to parameters for secondary structure prediction from sequence, and establish new building blocks in the design of functional RNA supramolecular structures.

References

1. Kruger, K.; Grabowski, P. J.; Zaug, A. J.; Sands, J.; Gottschling, D. E.; Cech, T. R., Self-splicing RNA: Autoexcision and autocyclization of the ribosomal RNA intervening sequence of *Tetrahymena*. *Cell* 1982, 31 (1), 147-57.
2. Guerrier-Takada, C.; Gardiner, K.; Marsh, T.; Pace, N.; Altman, S., The RNA moiety of ribonuclease P is the catalytic subunit of the enzyme. *Cell* 1983, 35 (3 Pt 2), 849-57.
3. Crick, F., Central dogma of molecular biology. *Nature* 1970, 227 (5258), 561-3.
4. Strobel, E. J.; Watters, K. E.; Loughrey, D.; Lucks, J. B., RNA systems biology: Uniting functional discoveries and structural tools to understand global roles of RNAs. *Current Opinion in Biotechnology* 2016, 39, 182-91.
5. Kuo, M. Y.; Sharmeen, L.; Dinter-Gottlieb, G.; Taylor, J., Characterization of self-cleaving RNA sequences on the genome and antigenome of human hepatitis delta virus. *Journal of Virology* 1988, 62 (12), 4439-44.
6. Lambowitz, A. M.; Zimmerly, S., Group II introns: Mobile ribozymes that invade DNA. *Cold Spring Harbor Perspectives in Biology* 2011, 3 (8), a003616.
7. Wedekind, J. E.; Dutta, D.; Belashov, I. A.; Jenkins, J. L., Metalloriboswitches: RNA-based inorganic ion sensors that regulate genes. *Journal of Biological Chemistry* 2017, 292 (23), 9441-9450.
8. Kim, P. B.; Nelson, J. W.; Breaker, R. R., An ancient riboswitch class in bacteria regulates purine biosynthesis and one-carbon metabolism. *Molecular Cell* 2015, 57 (2), 317-28.
9. Di Ruscio, A.; Ebralidze, A. K.; Benoukraf, T.; Amabile, G.; Goff, L. A.; Terragni, J.; Figueroa, M. E.; De Figueiredo Pontes, L. L.; Alberich-Jorda, M.; Zhang, P.; Wu, M.; D'Alo, F.; Melnick, A.; Leone, G.; Ebralidze, K. K.; Pradhan, S.; Rinn, J. L.; Tenen, D. G., DNMT1-interacting RNAs block gene-specific DNA methylation. *Nature* 2013, 503 (7476), 371-376.
10. Hacısuleyman, E.; Goff, L. A.; Trapnell, C.; Williams, A.; Henao-Mejia, J.; Sun, L.; McClanahan, P.; Hendrickson, D. G.; Sauvageau, M.; Kelley, D. R.; Morse, M.; Engreitz, J.; Lander, E. S.; Guttman, M.; Lodish, H. F.; Flavell, R.; Raj, A.; Rinn, J. L.,

Topological organization of multichromosomal regions by the long intergenic noncoding RNA Firre. *Nature Structural & Molecular Biology* 2014, 21 (2), 198-206.

11. Gasiunas, G.; Barrangou, R.; Horvath, P.; Siksnys, V., Cas9-crRNA ribonucleoprotein complex mediates specific DNA cleavage for adaptive immunity in bacteria. *Proceedings of the National Academy of Sciences* 2012, 109 (39), E2579–E2586.

12. Jinek, M.; Chylinski, K.; Fonfara, I.; Hauer, M.; Doudna, J. A.; Charpentier, E., A programmable dual-RNA-guided DNA endonuclease in adaptive bacterial immunity. *Science* 2012, 337 (6096), 816-21.

13. Cong, L.; Ran, F. A.; Cox, D.; Lin, S.; Barretto, R.; Habib, N.; Hsu, P. D.; Wu, X.; Jiang, W.; Marraffini, L. A.; Zhang, F., Multiplex genome engineering using CRISPR/Cas systems. *Science (New York, N.Y.)* 2013, 339 (6121), 819-823.

14. Garber, K., Worth the RISC? *Nature Biotechnology* 2017, 35 (3), 198-202.

15. Guo, P.; Erickson, S.; Anderson, D., A small viral RNA is required for in vitro packaging of bacteriophage phi 29 DNA. *Science* 1987, 236, 690-694.

16. Shu, D.; Moll, W. D.; Deng, Z.; Mao, C.; Guo, P., Bottom-up assembly of RNA arrays and superstructures as potential parts in nanotechnology. *Nano Letters* 2004, 4 (9), 1717-1723.

17. Jasinski, D.; Haque, F.; Binzel, D. W.; Guo, P., Advancement of the emerging field of RNA nanotechnology. *ACS Nano* 2017, 11 (2), 1142-1164.

18. Bailey, S.; Wichitwechkarn, J.; Johnson, D.; Reilly, B.; Anderson, D.; Bodley, J., Phylogenetic analysis and secondary structure of the *Bacillus subtilis* bacteriophage RNA required for DNA packaging. *Journal of Biological Chemistry* 1990, 265, 22365-22370.

19. Reid, R.; Zhang, F.; Benson, S.; Anderson, D., Probing the structure of bacteriophage phi29 prohead RNA with specific mutations. *Journal of Biological Chemistry* 1994, 269, 18656-18661.

20. Zhao, W.; Saha, M.; Ke, A.; Morais, M.; Jardine, P.; Grimes, S., A three-helix junction is the interface between two functional domains of prohead RNA in phi29 DNA packaging. *Journal of Virology* 2012, 86, 11625-11632.
21. Hao, Y.; Kieft, J. S., Diverse self-association properties within a family of phage packaging RNAs. *RNA* 2014, 20, 1-16.
22. Hao, Y.; Kieft, J. S., Three-way junction conformation dictates self-association of phage packaging RNAs. *RNA Biology* 2016, 13 (7), 635-45.
23. Koti, J.; Morais, M.; Rajagopal, R.; Owen, B.; McMurray, C.; Anderson, D., DNA packaging motor assembly intermediate of bacteriophage phi29. *Journal of Molecular Biology* 2008, 381 (5), 1114-32.
24. Rao, V.; Feiss, M., The bacteriophage DNA packaging motor. *Annual Review of Genetics* 2008, 42, 647-681.
25. Gilbert, W., Origin of life: The RNA world. *Nature* 1986, 319 (6055).
26. Hill, A. C.; Bartley, L. E.; Schroeder, S. J., Prohead RNA: A noncoding viral RNA of novel structure and function. *Wiley Interdisciplinary Reviews RNA* 2016, 7 (4), 428-37.
27. Hao, C.; Li, X.; Tian, C.; Jiang, W.; Wang, G.; Mao, C., Construction of RNA nanocages by re-engineering the packaging RNA of Phi29 bacteriophage. *Nature Communications* 2014, 5, 3890.
28. Guo, S.; Tschammer, N.; Mohammed, S.; Guo, P., Specific delivery of therapeutic RNAs to cancer cells via the dimerization mechanism of phi29 motor pRNA. *Human Gene Therapy* 2005, 16, 1097-1109.
29. Khaled, A.; Guo, S.; Li, F.; Guo, P., Controllable self-assembly of nanoparticles for specific delivery of multiple therapeutic molecules to cancer cells using RNA nanotechnology. *Nano Letters* 2005, 5 (9), 1797-808.
30. Shu, D.; Shu, Y.; Haque, F.; Abdelmawla, S.; Guo, P., Thermodynamically stable RNA three-way junction for constructing multifunctional nanoparticles for delivery of therapeutics. *Nature Nanotechnology* 2011, 6, 658-667.

31. Zhang, H.; Endrizzi, J.; Shu, Y.; Haque, F.; Sauter, C.; Shlyakhtenko, L.; Lyubchenko, Y.; Guo, P.; Chi, Y., Crystal structure of 3WJ core revealing divalent ion-promoted thermostability and assembly of the Phi29 hexameric motor pRNA. *RNA* 2013, 19, 1226-1237.
32. Brion, P.; Westhof, E., Hierarchy and dynamics of RNA folding. *Annual Review of Biophysics and Biomolecular Structure* 1997, 26, 113-37.
33. Mathews, D. H.; Turner, D. H., Prediction of RNA secondary structure by free energy minimization. *Current Opinion in Structural Biology* 2006, 16 (3), 270-8.
34. Batey, R. T.; Rambo, R. P.; Doudna, J. A., Tertiary motifs in RNA structure and folding. *Angewandte Chemie International Edition* 1999, 38 (16), 2326-2343.
35. Lescoute, A.; Westhof, E., Topology of three-way junctions in folded RNAs. *RNA* 2006, 12, 83-93.
36. Wichitwechkarn, J.; Bailey, S.; Bodley, J.; Anderson, D., Prohead RNA of bacteriophage phi29: Size, stoichiometry and biological activity. *Nucleic Acids Research* 1989, 17 (9), 3459-3468.
37. Gu, X.; Schroeder, S., Different sequences show similar quaternary interaction stabilities in prohead viral RNA self-assembly. *Journal of Biological Chemistry* 2011, 286, 14419-14426.
38. Zhang, C.; Tellinghuisen, T.; Guo, P., Use of circular permutation to assess six bulges and four loops of DNA-packaging pRNA of bacteriophage phi29. *RNA* 1997, 3, 315-323.
39. Tyagi, R.; Mathews, D. H., Predicting helical coaxial stacking in RNA multibranch loops. *RNA* 2007, 13 (7), 939-951.
40. Chen, C.; Zhang, C.; Guo, P., Sequence requirement for hand-in-hand interaction in formation of RNA dimers and hexamers to gear phi29 DNA translocation motor. *RNA* 1999, 5 (6), 805-18.
41. Schroeder, S. J.; Turner, D. H., Optical melting measurements of nucleic acid thermodynamics. *Methods in Enzymology* 2009, 468, 371-387.

42. Lee, T. J.; Haque, F.; Shu, D.; Yoo, J. Y.; Li, H.; Yokel, R. A.; Horbinski, C.; Kim, T. H.; Kim, S. H.; Kwon, C. H.; Nakano, I.; Kaur, B.; Guo, P.; Croce, C. M., RNA nanoparticle as a vector for targeted siRNA delivery into glioblastoma mouse model. *Oncotarget* 2015, 6 (17), 14766-76.
43. Cui, D.; Zhang, C.; Liu, B.; Shu, Y.; Du, T.; Shu, D.; Wang, K.; Dai, F.; Liu, Y.; Li, C.; Pan, F.; Yang, Y.; Ni, J.; Li, H.; Brand-Saberi, B.; Guo, P., Regression of gastric cancer by systemic injection of RNA nanoparticles carrying both ligand and siRNA. *Scientific Reports* 2015, 5, 10726.
44. Zhang, Y.; Leonard, M.; Shu, Y.; Yang, Y.; Shu, D.; Guo, P.; Zhang, X., Overcoming tamoxifen resistance of human breast cancer by targeted gene silencing using multifunctional pRNA nanoparticles. *ACS Nano* 2017, 11 (1), 335-346.
45. Hill, A. C.; Schroeder, S. J., Thermodynamic stabilities of three-way junction nanomotifs in prohead RNA. *RNA* 2017.
46. Ding, F.; Lu, C.; Zhao, W.; Rajashankar, K.; Anderson, D.; Jardine, P.; Grimes, S.; Ke, A., Structure and assembly of the essential RNA ring component of a viral DNA packaging motor. *Proceedings of the National Academy of Sciences* 2011, 108, 7357-7362.

Chapter 2: Prohead RNA: A Noncoding Viral RNA of Novel Structure and Function

The following chapter was published in similar form in *WIREs RNA* by the author of this dissertation. All text and figures are taken with the permissions of a Creative Commons license.

Abstract

Prohead RNA (pRNA) is an essential component of the powerful phi (Φ)29-like bacteriophage DNA packaging motor. However, the specific role of this unique RNA in the Φ 29 packaging motor remains unknown. This review examines pRNA as a noncoding RNA of novel structure and function. In order to highlight the reasons for exploring the structure and function of pRNA, we (1) provide an overview of Φ 29-like bacteriophage and the Φ 29 DNA packaging motor, including putative motor mechanisms and structures of its component parts; (2) discuss pRNA structure and possible roles for pRNA in the Φ 29 packaging motor; (3) summarize pRNA self-assembly; and (4) describe the prospective therapeutic applications of pRNA. Many questions remain to be answered in order to connect what is currently known about pRNA structure to its novel function in the Φ 29 packaging motor. The knowledge gained from studying the structure, function, and sequence variation in pRNA will help develop tools to better navigate the conformational landscapes of RNA.

Φ 29-like Bacteriophages

Bacteriophages are viruses that infect bacteria and may play an indirect role in human health and disease states¹⁻³. First discovered in 1915 in micrococci, phages are now known to infect a wide range of bacteria, including extreme acidophiles and

thermophiles⁴⁻⁶. Among the most ubiquitous phages are those that infect soil-dwelling bacteria. These include phages hosted by members of the *Bacillus* genus, which are aerobic, Gram-positive, spore-forming eubacteria that thrive in soil and decaying plant matter. To date, all bacteriophages isolated from *Bacillus* species have been found to share certain features, *i.e.*, they are all tailed phages that have double-stranded DNA (dsDNA) genomes and prolate icosahedral heads⁷. The Φ 29-like bacteriophages are phages that infect *Bacillus subtilis* and related species, including *Bacillus pumilis*, *Bacillus amyloliquefaciens*, and *Bacillus licheniformis*⁷.

In the order of tailed bacteriophages, Φ 29-like phages belong to the *Podoviridae* family, which are phages with dsDNA genomes and short, noncontractile tails⁷. The Φ 29-like bacteriophage genus encompasses several species, including Φ 15, B103, BS32, GA-1, M2, Nf, and PZA, which have been split into Groups I, II, and III on the basis of serological properties, DNA physical maps, peptide maps, and partial or complete DNA sequences⁷. In addition to Φ 29, Group I includes species Φ 15, BS32, and PZA; Group II includes B103, M2, and Nf; and Group III includes only GA-1⁷⁻⁸. These classifications reflect not only genetic relatedness, but also geographical distribution: Members of Group I were isolated in the United States, Group II in Japan, and Group III in Europe⁷. Figure 1 is a phylogenetic tree depicting the evolutionary relationships among the species in Groups I, II, and III⁸.

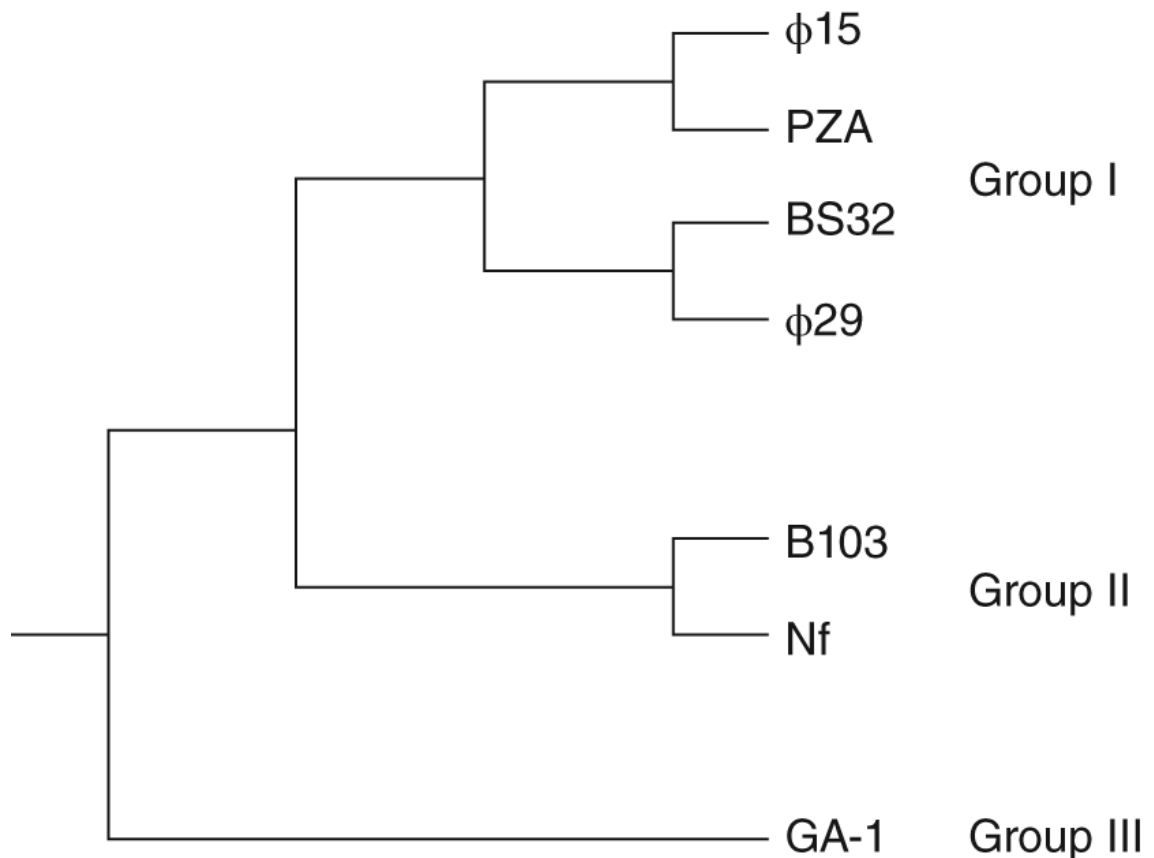


Figure 1 Phylogenetic tree depicting the evolutionary branching of the Φ 29-like bacteriophage genus into Groups I, II, and III. (Figure adapted from data in ⁸ and originally published in ⁹.)

The Φ 29-like phages have prolate, $T = 3$, $Q = 5$ icosahedral heads with fivefold rotational symmetry. The Φ 29 phage dimensions are approximately 540 Å by 450 Å, with a 16 Å-thick protein shell ¹⁰. The Φ 29 phage tail facilitates viral entry into the *Bacillus* host by binding and hydrolyzing the bacterial cell wall ¹⁰. It is approximately 380 Å long and exhibits pseudo-sixfold symmetry. All Φ 29-like bacteriophages have linear, dsDNA genomes approximately 20 kb in size, with a terminal protein (TP) covalently bound to each 5' end ⁸. This protein functions to prime replication via a mechanism that is also used by other phages, linear plasmids, and adenoviruses ⁷⁻⁸. For this reason, Φ 29 has long served as a system in which to study the mechanism of

protein-primed replication, as well as other molecular mechanisms, including transcription regulation, phage morphogenesis, and DNA packaging^{7, 10-12}.

The Φ 29-like Phage Packaging Motor

Overview of the Packaging Motor

During the Φ 29 phage replicative cycle, newly synthesized genomic DNA must be encapsidated to generate fully functional virus particles. This task is accomplished by the powerful Φ 29 packaging motor. Single-molecule optical tweezer experiments have shown that the Φ 29 motor packages DNA against an internal force greater than 50 pN, overcoming significant enthalpic, entropic, and DNA-bending energies to condense the 19.3 kb viral genome to near-crystalline densities within the capsid, all within about 5.5 min¹³⁻¹⁴. (As a point of reference, myosin moving across actin filaments generate approximately 1–5 pN.) The high internal pressure achieved by the Φ 29 motor, estimated to be approximately 60 atmospheres, propels initial DNA injection into the host cell^{13, 15}.

The motor complex comprises three coaxial rings through which DNA is threaded during packaging¹⁶. Proximal to the viral prohead is a ring of connector proteins, and distal to the prohead is a ring of ATPase proteins. A prohead RNA (pRNA) ring, unique to the Φ 29-like bacteriophage DNA packaging motor, forms the interface between the connector and ATPase motor proteins¹⁷⁻¹⁸. Figure 2 highlights the spatial orientation of these essential components, where the arrows indicate putative pRNA roles in the packaging motor. Motor function is driven by the ATPase (gene product, or gp 16), which converts the chemical energy of ATP into the mechanical energy needed to power encapsidation of the viral genome. Thus, the minimal

packaging motor consists of major capsid proteins (gp8), head–tail connector proteins (gp10), pRNA, ATPases (gp16), and genomic DNA linked to the TP (gp3) ¹⁰. However, the Φ 29 motor mechanism of DNA packaging remains to be determined.

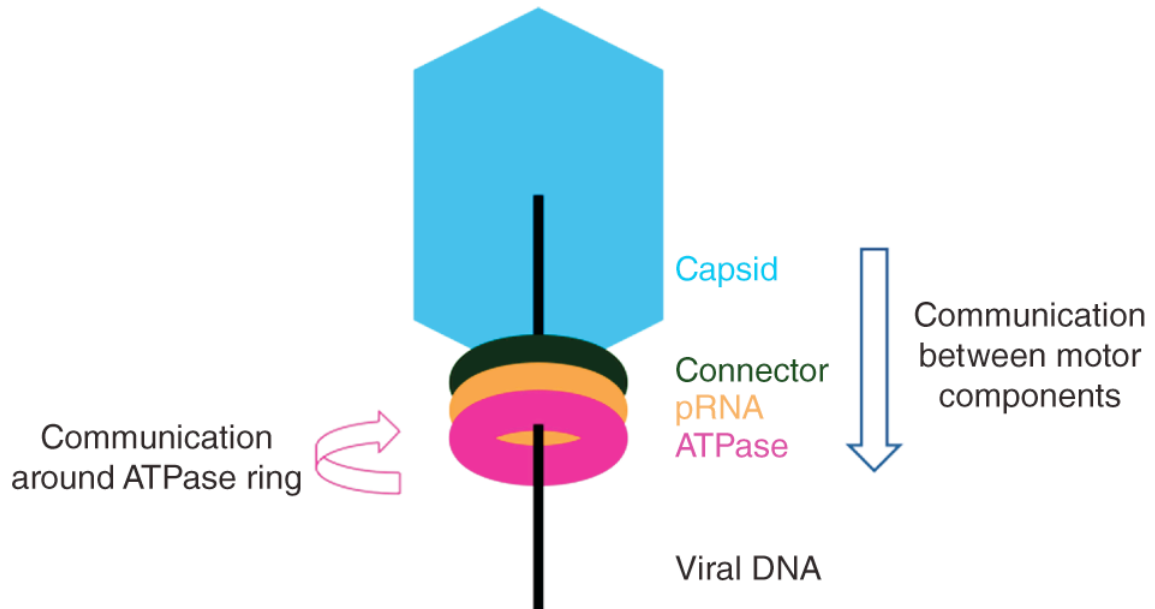


Figure 2 Representation of the orientation of Φ 29 motor components. The viral capsid is shown in blue, the connector protein in green, the pRNA in orange, the ATPase in pink, and viral DNA as a black line. The blue vertical arrow represents the role that pRNA may play in communicating from the viral capsid and connector to the ATPase during packaging. The pink circular arrow represents the role that pRNA may play in coordinating ATPase activity around the ring. Figure originally published in ⁹.

Two very different mechanisms for Φ 29 motor activity have been proposed, and each is supported by abundant experimental data. In the mechanism Liu *et al.* proposed ^{16, 19-21}, each ATPase in a fivefold symmetric ring releases an ADP and binds an ATP, in turn, during a ‘dwell’ phase. In a subsequent ‘burst’ phase, the ATPs are hydrolyzed, and 2.5 bp of DNA are packaged for each of four phosphates released, totaling 10 bp of DNA translocated per burst ^{16, 19-21}. In this model, one of the five ring ATPases plays a regulatory role, directly contacting the viral DNA, binding and hydrolyzing ATP, and

releasing phosphate, without contributing to DNA translocation, *per se* ^{20, 22}. The regulatory ATPase instead may play a role in initiating or concluding the ATP hydrolysis cascade ²⁰, or it may be responsible for realigning the viral DNA, which is approximately -14° out of register following the burst phase ^{16, 23}. It has also been suggested that this special subunit makes crucial electrostatic contacts that play a role in an underlying symmetry-breaking mechanism that is important for DNA packaging, reconciling the fivefold rotational symmetry of the viral prohead with the 12-fold rotational symmetry of the connector protein and sixfold symmetry of the tail ²⁴⁻²⁹. The strengths of this model are the supporting rigorous kinetic data and single-molecule force microscopy data. However, many questions remain to be answered about the regulatory ATPase. Most saliently, what physical or conformational features distinguish the regulatory subunit from the other subunits?

In a mechanism that Schwartz *et al.* proposed ³⁰, the $\Phi 29$ viral DNA revolves, rather than rotates, during packaging ³¹⁻³². Each ATPase in a sixfold symmetric ring binds ATP, thereby inducing a conformational change that increases ATPase affinity for dsDNA. Upon ATP hydrolysis, the ATPase undergoes another conformational change that reduces its affinity for dsDNA, thus promoting DNA handoff from one subunit to the next around the ring. Each ATP hydrolyzed moves the DNA 1.75 bp into the capsid ³⁰. Furthermore, contrary to studies that have indicated that the ATPase binds to pRNA on the prohead prior to binding viral DNA ³³, this model supports an alternative packaging motor assembly pathway in which the ATPase assembles around the viral DNA prior to docking on the prohead ^{13, 30}. The strengths of this revolution model include the following: that it accommodates stoichiometries of either five or six

ATPases; that all subunits have an equivalent, active role; and that revolution allows the viral DNA to be packaged in low-energy, nonsupercoiled conformations³⁰. However, the well-designed DNA and ATPase *in vitro* system used to determine stoichiometry and test the revolution mechanism may differ from the behavior of the Φ 29 motor *in vivo*. The *in vitro* system will be very useful for nanotechnology applications.

One model of the phi29 motor that may reconcile the differences proposed by Liu *et al.*¹⁶ and Schwartz *et al.*³⁰ is an asymmetrical hexameric ATPase in which four units exist as monomers and two units exist as a dimer, which may be a ‘special’ or regulatory subunit³⁴. In this model, noncovalent dimer formation is mediated by an arginine finger that extends from one ATPase unit to an adjacent unit. Mutation of the arginine finger abolishes ATPase oligomerization, ATP binding and hydrolysis, and DNA translocation³⁴. The presence of a dimer in a motor with hexameric ATPase stoichiometry could explain previous cryo-electron microscopy (cryo-EM) data that support a pentamer configuration, because cryo-EM reconstruction methods rely on the averaging of many images³⁴.

No model yet explains the role of pRNA in the Φ 29 packaging motor. More detailed structural information about the pRNA, ATPase, and the pRNA–ATPase and the ATPase–viral DNA interactions in the packaging motor may help discriminate between these two models or suggest new mechanisms.

Structures of the Packaging Motor Protein Components

In the Φ 29 motor, three-dimensional (3D) structures have been determined for the connector protein and pieces of the pRNA. The connector protein exists as a dodecameric assembly of 36 kDa gp10 protomers, forming the interface between the

prohead and the rest of the packaging motor³⁵. The assembled, 422 kDa superstructure is cone shaped and 75 Å long, with the wide end, formed by residues 42–129 and 248–285, measuring 138 Å, and the narrow end, formed by residues 158–202, measuring just 35 Å^{25,35}. A crystal structure of the connector protein assembly, refined to 2.1 Å, shows that the 35 Å-wide central channel is largely electronegative, but it possesses two rings of lysine residues (formed by K200 and K209) spaced 20 Å apart with neighboring lysine residues in the ring spaced 10 Å apart^{10,35}. This geometry would permit four points of electrostatic interactions between the phosphate backbone of the translocating DNA and the connector central channel³⁵. Structural comparisons between three connector protein crystal structures obtained by Simpson *et al.* suggest that flexibility exists in the wide end of the connector, presumably to allow for rotation within the portal during packaging²⁵.

No structural data yet exist for the full pRNA molecule, the ATPase, or the pRNA–ATPase complex. The ATPase can be modeled from homologous bacteriophage ATPases that do not require pRNA. However, high-resolution structural information will be essential for fully understanding the function of pRNA in the Φ29 packaging motor.

Prohead RNA

Prohead RNA Primary and Secondary Structure

To date, Φ29 and related bacteriophages are the only known phages to require a nucleic acid molecule, pRNA, for packaging activity³⁶ (Figure 2). Early experiments on the Φ29 bacteriophage packaging motor revealed sensitivity to ribonucleases (RNases) T1 and A³⁶. Pretreatment with RNase inhibitor restored Φ29 assembly³⁶⁻³⁷. Studies on the

motor determined that a phage-encoded RNA molecule, dubbed pRNA for its association with the prohead, is an essential component of the Φ 29 phage packaging motor¹⁷.

Φ 29 pRNA is a 174-nucleotide (nt) transcript encoded in the viral genome from 147 to 320 bp³⁷⁻³⁸. It comprises two distinct domains: Domain I, spanning the first 117 bases; and Domain II, spanning bases 131–174. These domains are linked by a 13-base stretch of unstructured, single-stranded RNA³⁹. Figure 3 depicts Domains I and II in folded Φ 29 pRNA^{37, 39}. A 120-base construct absent Domain II packages genomic DNA with wild-type activity *in vitro* and consequently is widely used for *in vitro* studies; however, Domain II is highly conserved among all Φ 29-like phages, suggesting that it plays an important role *in vivo*, potentially in phage morphogenesis^{10, 37-38}. Two regions of Domain I RNA are functionally important to the packaging motor. The first is a region deemed important for prohead binding, determined by ribonuclease footprinting to be bases 22–84, and by mutagenesis to be bases 40–91⁴⁰⁻⁴¹. The second region is required for DNA packaging, determined by *in situ* truncation and packaging assays to be bases 1–25 and furthered specified by mutagenesis studies to include bases 1–28 and 92–117^{10, 40-43}.

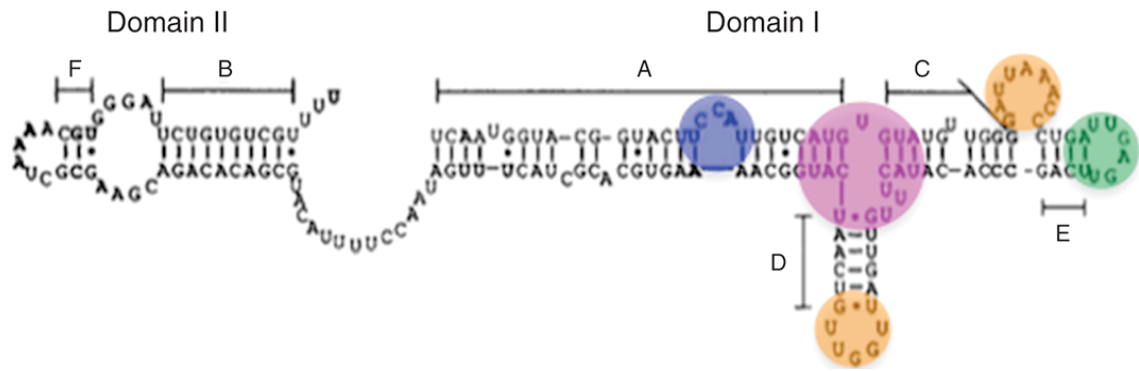


Figure 3 Secondary structure of $\Phi 29$ pRNA showing structured Domains I and II, an unstructured linker, and helices A through F^{37,39}. The bulge loop is highlighted in blue, the 3WJ in magenta, the CE (right hand) and D (left hand) loops in orange, and the E loop in green. (Reprinted with permission from³⁷. Copyright 1990 Elsevier). Figure originally published in⁹.

Although the sequence similarity among all $\Phi 29$ -like bacteriophage pRNAs is only 12%, pRNA secondary structure is highly conserved^{39, 44-45}. The secondary structure of pRNA comprises six helices, named A–F, all of which are found in Domain I with the exception of helices B and F³⁹ (Figure 3). In the 120-base $\Phi 29$ pRNA construct, there are five single-base bulges, two stem loops, one three-base bulge, one bifurcation bulge, and one bulge loop⁴⁶. All of the single-base bulges appear to be nonessential; however, deletion of U5 reduces DNA packaging activity by approximately 10-fold^{43, 46-47}. The three-base bulge (C₁₈C₁₉A₂₀) in helix A is necessary for DNA packaging, and C₁₈C₁₉ bind the $\Phi 29$ ATPase³³. The bulge loop and two stem loops are indispensable for procapsid binding, DNA packaging, and phage assembly⁴⁶. Studies on the $\Phi 29$ pRNA three-way junction (3WJ) have yielded conflicting results upon deletion of the polyuridine bifurcation bulge (U₂₉, U₇₁₋₇₃), with one study reporting loss of binding and packaging activity⁴⁷, and another reporting no loss of procapsid binding or DNA packaging activity⁴⁶. Yet another study reported that two of the four bulge uridine residues in the $\Phi 29$ 3WJ (U₂₉, U₇₂₋₇₄) must be retained for pRNA

binding to the viral prohead and for wild-type levels of packaging activity⁴⁸. All of these studies implicate the 3WJ as an important contributor to pRNA function. It is likely that the junction acts as a hinge that imparts flexibility on the RNA, correctly placing helices in the spatial orientation necessary for packaging⁴⁶. The results of *in vitro* self-assembly assays (see below) also support the hypothesis that the 3WJ is an important part of pRNA secondary structure⁴⁹.

Prohead RNA Tertiary Structure and Function

The pRNA assembles on the prohead in a magnesium ion-dependent fashion and serves as a scaffold for ring ATPase assembly^{33, 41, 50-51}. Its CE and D interlocking loops mediate self-association, while its A helices protrude from the motor like spokes, making contact with the ATPase^{33, 52}. In proheads isolated from infected cells, 5–6 copies of pRNA are present³⁸. The hairpin loop that binds the connector protein resembles ribosomal RNA protein-binding loops⁵³. Crystal structures of a 71-nt piece of Φ 29 pRNA (bases 25–95) and a Φ 29 3WJ construct were determined to 3.5 and 3.05 Å, respectively^{51, 54}. Although the 71-nt Φ 29 pRNA crystallized as a tetramer, fitting of the pRNA protomers into previous cryo-electron microscopy (EM) reconstructions supports a pentamer model in the context of the motor⁵¹. Electron paramagnetic resonance (EPR) spectroscopy experiments show that interhelical angles adopted by the tetramer are not representative of pRNA in a solution state and suggest the need for more complexity in modeling oligomeric pRNA⁵⁵. The Φ 29 pRNA 3WJ is a multibranch loop at the intersection of helices A, C, and D (Figure 3). The 54-nt 3WJ monomer structure revealed metal binding sites that altered the H1/H3 interhelical angle, and 3D modeling of the 3WJ structure is consistent with its existence as a

hexamer in the context of the motor⁵⁴. The structure of the 5′-C₁₈C₁₉A₂₀-3′ bulge loop in Φ29 pRNA has also been determined using nuclear magnetic resonance (NMR) spectroscopy. A 27-mer RNA fragment containing the bulge showed that it introduces a 33–35° bend in the helical axis, restricting interhelical motion⁵⁶. The loops in pRNA are the flexible joints that may have multiple, dynamic conformations during the packaging process.

Although the role of pRNA in the motor remains unknown, its absence prior to prohead assembly as well as in mature Φ29 phage indicates that it performs an essential role specifically in DNA packaging^{10, 18, 36, 38}. Current models for genome packaging, however, often ignore pRNA or contend that it serves a purely structural function^{16, 30, 57}. Several roles for pRNA in the Φ29 motor are possible. One possibility is that pRNA serves as a ‘molecular washer,’ *i.e.*, it helps absorb the stress imposed by the moving parts in the motor. Another possibility is that pRNA allows for communication between the motor components, *i.e.*, between the viral capsid and connector and the ATPase, during packaging⁵¹ (vertical arrow in Figure 2). The Φ29 motor has been shown to change packaging rates as pressure builds within the viral head^{13, 16}, suggesting communication between the viral head and the ATPase. As pRNA is located at the center of the packaging motor⁴⁸, it is possible that pRNA may play a role in communicating to the ATPase when the viral head is full. Yet another possibility is that pRNA helps coordinate the activity of the ATPase subunits, resulting in their sequential firing around the ring²⁰⁻²¹ (circular arrow in Figure 2). It is also possible that pRNA serves both communicative functions⁴⁸.

pRNA is unique to the Φ 29-like bacteriophage dsDNA packaging motor^{17-18, 39}. It is speculated that in other phages, a subdomain of another motor protein has assumed the role of pRNA. The large terminase protein found in other phages, *e.g.*, T4, is the structural equivalent of pRNA and the ATPase together⁵⁸. Furthermore, because pRNA is required for ATPase docking, it may be considered functionally analogous to a subdomain of the large terminase protein^{33, 58}. The idea that proteins could evolve to fulfill the role of RNA is consistent with the later stages of the RNA world hypothesis and evolution from an RNA-only world to an RNA-protein world⁵⁹⁻⁶⁰.

Prohead RNA Self-Association

Prohead RNA Interlocking Loops

Intermolecular Watson-Crick base pairing between nucleotides in the CE and D loops mediates self-association of pRNA molecules *in vivo* on the viral prohead as well as *in vitro*^{39, 44-45, 52} (Figure 4). NMR studies on 19- and 35-nt Φ 29 pRNA heterodimers, in which each molecule contained either a CE or a D loop, showed that two intermolecular G–C base pairs form between the loops in a Mg^{2+} -dependent fashion⁶¹. Disruption of the flexibility of the D loop via mutagenesis (U80C) also disrupted the G–C base pair formation and abolished heterodimer assembly, but interestingly did not affect prohead binding or DNA packaging⁶¹.

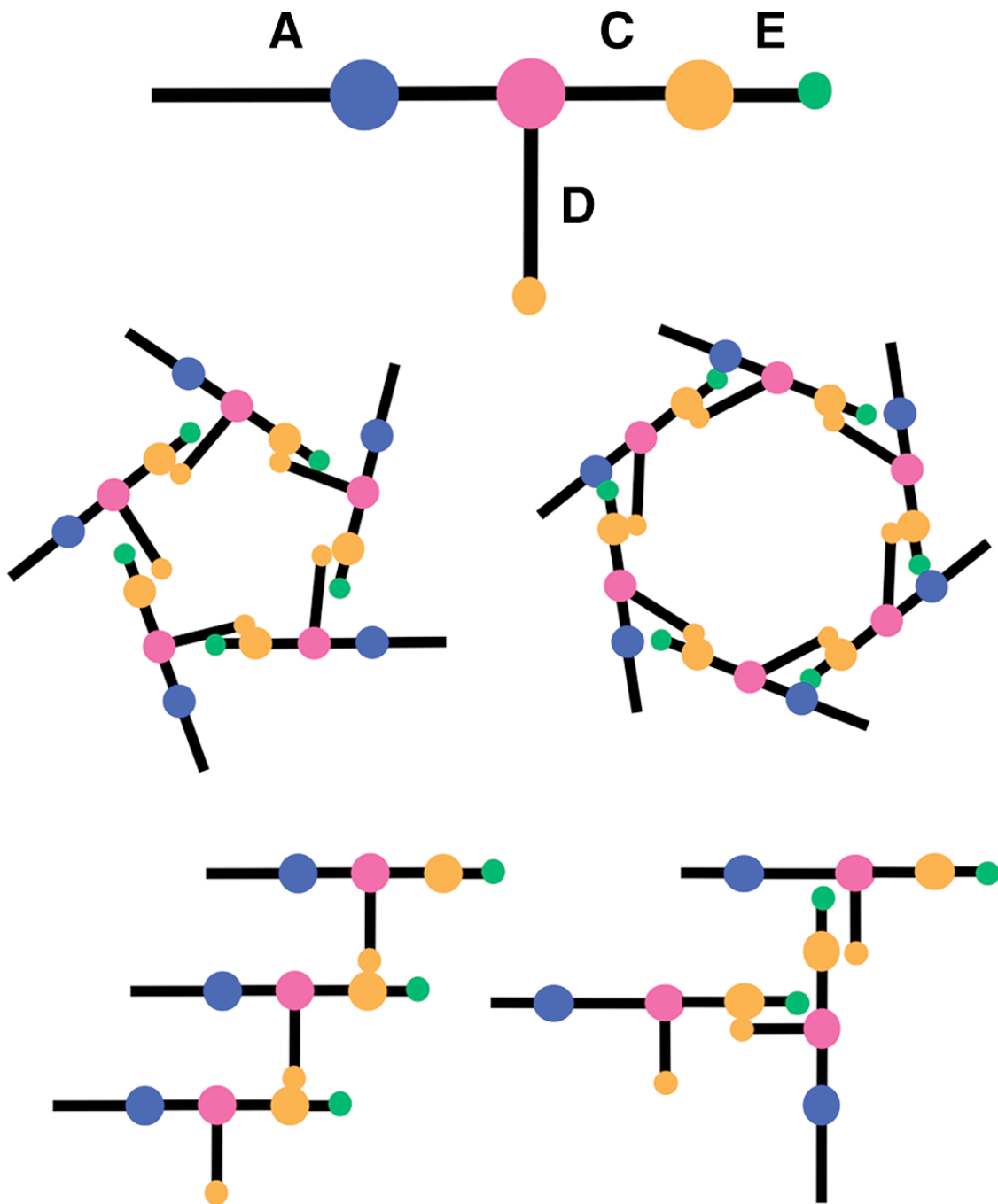


Figure 4 Ball-and-stick model of pRNA where balls are loops and sticks are helices. CE and D loops (orange) mediate self-assembly of pRNA into nanorings (as found on the prohead) and potentially linear and/or branched structures *in vitro*. Figure originally published in ⁹.

The value of *in vitro* self-association studies lies in providing fundamental biophysical data that inform hypotheses of *in vivo* mechanisms and guide rational

design of RNA assemblies. *In vitro* self-association studies have shown that pRNA–pRNA interaction varies by sequence and depends upon pRNA concentration as well as upon other factors, such as temperature and magnesium and sodium chloride concentration⁴⁴. Importantly, these studies indicate that different pRNAs have different self-association properties. For example, SF5 pRNA has the highest propensity for self-association, forming dimers, trimers, and several higher-order multimers at room temperature⁴⁴. However, more recent studies under different conditions indicate that SF5 pRNA forms only dimers, but that M2 pRNA assembles into highly thermostable multimeric species⁴⁹. These seemingly contradictory results suggest that the self-association behaviors of pRNA are more subtle than previously thought, and that these behaviors may be readily modulated by taking advantage of its sensitivity to salt, temperature, and other preparation conditions⁴⁹.

Prohead RNA Multibranch Loop

Many studies have taken steps toward addressing why different pRNAs exhibit different self-assembly properties. In a study by Gu *et al.*, pRNA sequences that showed different self-assembly properties had different base pairing stabilities in the CE and D interlocking loops but similar quaternary interaction stabilities, indicating that sequence variation outside of the interlocking loop sequences plays a role in pRNA self-assembly energetics⁴⁴. Studies on designer pRNA sequences retaining little to no sequence similarity to wild-type pRNA except in the paired CE and D loops and in the 3WJ indicate that helices do not contribute to pRNA assembly in a sequence-dependent fashion⁵¹. Investigations by Hao *et al.* revealed similar insights, demonstrating that mediocre CE and D loop ‘kissing’ interactions can be overcome with highly stable

scaffolds⁴⁹. These results implicate the 3WJ as an important contributor to pRNA–pRNA interactions. One hypothesis is that different nucleotide sequences at the 3WJ may be responsible for the observed differences in pRNA self-assembly properties⁴⁹. It is known that multibranch loops enable long-range contacts by determining the angles at which helices emerge. Furthermore, multibranch loops are key determinants of structural and functional roles in other RNAs, such as hairpin ribozymes⁶²⁻⁶⁵. EPR spectroscopy studies on pRNA monomers and dimers reveal that the interhelical angles in pRNA vary^{55, 66}, and single-molecule fluorescent resonance energy transfer (FRET) studies on the $\Phi 29$ pRNA 3WJ motif have shown that Mg^{2+} changes the interhelical angles⁵⁴. Thus, the sequence variation at pRNA 3WJs may confer variation in self-assembly by way of orienting these angles or shifting the distribution of angles in a dynamic ensemble of 3WJ conformations.

Applications and Future Directions

Prohead RNA in Nanobiotechnology

The study of nucleic acid folding and assembly has broad implications. DNA folding and assembly properties are widely used in the *de novo* construction of nanostructures⁶⁷⁻⁶⁹. Furthermore, rationally designed, self-assembling DNA ‘nanorobots’ are capable of delivering their molecular payloads according to an AND logic gate mechanism, suggesting that nucleic acids hold promise for rational nanoparticle design of delivery vehicles⁷⁰. Relative to DNA, RNA is suspected to have more potential as a raw material due to its more diverse catalytic and recognition properties and its capacity for robust tertiary and quaternary interaction, which rival those of proteins⁷¹⁻⁷². Proof-of-concept research into RNA engineering has yielded interesting results. For example,

studies exploiting RNA turn motifs demonstrated that RNA can be programmed to cotranscriptionally fold into desired nanostructures such as hexagonal lattices⁷³. Studies on self-assembling RNAi microsponges showed that RNA can be programmed as a delivery vehicle comprising both carrier and cargo, simultaneously maximizing small interfering RNA transfection efficiency and minimizing cytotoxicity and degradation during delivery⁷⁴. DNA–RNA hybrid nanomotifs have also been designed to form discrete tiles, fusing the functionality of RNA with the programmability of DNA to achieve a platform with RNA modalities including siRNAs, microRNAs, and aptamers for cell targeting and gene regulation⁷¹.

The unique and variable self-assembly properties of pRNA make it a ‘smart’ building block for rational design of 3D structures with nanotechnological and medical applications^{49, 75}. This has been demonstrated in several bottom-up fabrication studies. In a proof-of-concept study, Φ 29 pRNA dimers with a receptor-binding moiety on one arm and a gene-silencing molecule on another successfully targeted cancer cells⁷⁶. Additionally, thermodynamically stable X-shaped nanostructures using the Φ 29 pRNA scaffold can carry up to four siRNAs and elicit effective gene silencing compared to individual siRNA oligomers⁷⁷. Importantly, these nanostructures selectively target and remain localized in cancer cells in a mouse model⁷⁷. Corroborating these results, 14 other pRNA-based nanoparticles have been developed with cancer-targeting functionality⁷⁸.

Unanswered Questions

Whether pRNA assembles into hexamers or pentamers on the viral prohead is still debated. Competition inhibition assays, single fluorophore imaging, atomic force

microscopy, and cryo-EM studies indicate that pRNA assembles into hexamers on the prohead^{50, 52, 54, 79-80}. However, high-resolution cryo-EM data on complete proheads using relaxed or asymmetric reconstruction and difference maps of pRNA-truncated proheads support a pentamer model^{26, 81-82}. Crystal structures have done little to resolve this debate. Model-building of the Φ 29 pRNA 3WJ, which crystallized as a monomer, supported the hypothesis that pRNA assembles into hexamers on the viral prohead⁵⁴. Yet, a 71-nt pRNA construct with several deletions in the CE and D loops was shown to crystallize as a tetramer, and analysis of this structure and fitting into previously obtained cryo-EM reconstructions supported the hypothesis that pRNA forms a pentamer on the prohead⁵¹. EPR studies have suggested that pRNA oligomeric modeling requires more complexity⁵⁵. It is known that *in vitro*, pRNA is capable of forming both pentamers and hexamers^{44, 52, 83}. Until higher-resolution structural data and more information about the *in vivo* assembly mechanism of the Φ 29 motor are available, the biologically relevant stoichiometry remains to be determined.

The stoichiometry of the ATPase in the Φ 29 motor is also debated. As discussed above, the numbers of subunits engaged in motor activity in the foremost models of the Φ 29 motor mechanism are in conflict. Again, high-resolution structural data of the Φ 29 motor will be necessary to determine which stoichiometry is biologically relevant, as well as to distinguish between the currently proposed models.

Conclusion

The Φ 29 bacteriophage DNA packaging motor is a unique and powerful biomolecular motor that uses pRNA, a viral RNA of novel structure and function, to package its genome during replication. However, the specific indispensable function of pRNA is yet

unknown. Outside of the context of the motor, pRNA displays robust self-assembly behavior that is highly dependent on sequence and assembly conditions, with some species of pRNA capable of forming thermodynamically stable multimers. It has been shown that RNA, like DNA, can serve as a raw material in the rational design of functional 3D structures. The pRNA is uniquely positioned to serve as a platform for developing supramolecular structures with targeting and delivery functions due to its stability and self-association properties. However, much remains to be learned about pRNA, and elucidating its role in the Φ 29 viral molecular machine will hinge on high-resolution structural data to help inform new structure–function hypotheses.

References

1. Norman, Jason M.; Handley, Scott A.; Baldrige, Megan T.; Droit, L.; Liu, Catherine Y.; Keller, Brian C.; Kambal, A.; Monaco, Cynthia L.; Zhao, G.; Fleshner, P.; Stappenbeck, Thaddeus S.; McGovern, Dermot P.; Keshavarzian, A.; Mutlu, Ece A.; Sauk, J.; Gevers, D.; Xavier, Ramnik J.; Wang, D.; Parkes, M.; Virgin, Herbert W., Disease-specific alterations in the enteric virome in inflammatory bowel disease. *Cell* 2015, 160 (3), 447-460.
2. Denou, E.; Bruttin, A.; Barretto, C.; Ngom-Bru, C.; Brussow, H.; Zuber, S., T4 phages against *Escherichia coli* diarrhea: Potential and problems. *Virology* 2009, 388 (1), 21-30.
3. Summers, W. C., Bacteriophage therapy. *Annual Review of Microbiology* 2001, 55 (1), 437-451.
4. Tapia, P.; Flores, F.; Covarrubias, P.; Acuna, L.; Holmes, D.; Quatrini, R., Complete genome sequence of temperate bacteriophage AcaML1 from the extreme acidophile *Acidithiobacillus caldus* ATCC 51756. *Journal of Virology* 2012, 86 (22), 12452-12453.
5. Sakaki, Y.; Oshima, T., Isolation and characterization of a bacteriophage infectious to an extreme thermophile, *Thermus thermophilus* HB8. *Journal of Virology* 1975, 15 (6), 1449-1453.
6. Twort, F., An investigation on the nature of ultra-microscopic viruses. *Bacteriophage* 2011, 1 (3), 127-129.
7. Meijer, W.; Horcajadas, J.; Salas, M., Phi29 family of phages. *Microbiology and Molecular Biology Reviews* 2001, 65, 261-287.
8. Pecenkova, T.; Paces, V., Molecular phylogeny of phi29-like phages and their evolutionary relatedness to other protein-primed replicating phages and other phages hosted by gram-positive bacteria. *Journal of Molecular Evolution* 1999, 48 (2), 197-208.
9. Hill, A. C.; Bartley, L. E.; Schroeder, S. J., Prohead RNA: A noncoding viral RNA of novel structure and function. *Wiley Interdisciplinary Reviews RNA* 2016, 7 (4), 428-37.

10. Morais, M., Viral molecular machines chapter 23: The dsDNA packaging motor in bacteriophage phi29. *Advances in Experimental Medicine and Biology* 2012, 726, 511-547.
11. Grimes, S.; Jardine, P. J.; Anderson, D., Bacteriophage ϕ 29 DNA packaging. In *Advances in Virus Research*, Academic Press: 2002; Vol. Volume 58, pp 255-294.
12. Guo, P.; Grimes, S.; Anderson, D., A defined system for in vitro packaging of DNA-gp3 of the *Bacillus subtilis* bacteriophage phi 29. *Proceedings of the National Academy of Sciences* 1986, 83 (10), 3505-3509.
13. Smith, D.; Tans, S.; Smith, S.; Grimes, S.; Anderson, D.; Bustamante, C., The bacteriophage straight phi29 portal motor can package DNA against a large internal force. *Nature* 2001, 413, 748-752.
14. Cao, S.; Saha, M.; Zhao, W.; Jardine, P.; Zhang, W.; Grimes, S.; Morais, M., Insights into the structure and assembly of the bacteriophage phi29 double-stranded DNA packaging motor. *Journal of Virology* 2014, 88 (8), 3986-3996.
15. González-Huici, V.; Salas, M.; Hermoso, J. M., The push-pull mechanism of bacteriophage ϕ 29 DNA injection. *Molecular Microbiology* 2004, 52 (2), 529-540.
16. Liu, S.; Chistol, G.; Hetherington, C.; Tafuya, S.; Aathavan, K.; Schnitzbauer, J.; Grimes, S.; Jardine, P.; Bustamante, C., A viral packaging motor varies its DNA rotation and step size to preserve subunit coordination as the capsid fills. *Cell* 2014, 157 (3), 702-13.
17. Guo, P.; Erickson, S.; Anderson, D., A small viral RNA is required for in vitro packaging of bacteriophage phi 29 DNA. *Science* 1987, 236, 690-694.
18. Hendrix, R. W., Bacteriophage DNA packaging: RNA gears in a DNA transport machine. *Cell* 1998, 94 (2), 147-150.
19. Chemla, Y. R.; Aathavan, K.; Michaelis, J.; Grimes, S.; Jardine, P. J.; Anderson, D. L.; Bustamante, C., Mechanism of force generation of a viral DNA packaging motor. *Cell* 2005, 122 (5), 683-692.

20. Chistol, G.; Liu, S.; Hetherington, Craig L.; Moffitt, Jeffrey R.; Grimes, S.; Jardine, Paul J.; Bustamante, C., High degree of coordination and division of labor among subunits in a homomeric ring ATPase. *Cell* 2012, 151 (5), 1017-1028.
21. Moffitt, J.; Chemla, Y.; Aathavan, K.; Grimes, S.; Jardine, P.; Anderson, D.; Bustamante, C., Intersubunit coordination in a homomeric ring ATPase. *Nature* 2009, 457, 446-450.
22. Aathavan, K.; Politzer, A.; Kaplan, A.; Moffitt, J.; Chemla, Y.; Grimes, S.; Jardine, P.; Anderson, D.; Bustamante, C., Substrate interactions and promiscuity in a viral DNA packaging motor. *Nature* 2009, 461, 669-673.
23. Wang, J., Helical repeat of DNA in solution. *Proceedings of the National Academy of Sciences* 1979, 76 (1), 200-203.
24. Chistol, G., Dissecting the operating mechanism of a biological motor one molecule at a time. 2013.
25. Simpson, A. A.; Leiman, P. G.; Tao, Y.; He, Y.; Badasso, M. O.; Jardine, P. J.; Anderson, D. L.; Rossmann, M. G., Structure determination of the head–tail connector of bacteriophage ϕ 29. *Acta Crystallographica Section D* 2001, 57 (9), 1260-1269.
26. Morais, M.; Tao, Y.; Olson, N.; Grimes, S.; Jardine, P.; Anderson, D.; Baker, T.; Rossmann, M., Cryoelectron-microscopy image reconstruction of symmetry mismatches in bacteriophage phi29. *Journal of Structural Biology* 2001, 135 (1), 38-46.
27. Tang, J.; Olson, N.; Jardine, P. J.; Grimes, S.; Anderson, D. L.; Baker, T. S., DNA poised for release in bacteriophage ϕ 29. *Structure (London, England : 1993)* 2008, 16 (6), 935-943.
28. Xiang, Y.; Morais, M. C.; Battisti, A. J.; Grimes, S.; Jardine, P. J.; Anderson, D. L.; Rossmann, M. G., Structural changes of bacteriophage ϕ 29 upon DNA packaging and release. *The EMBO Journal* 2006, 25 (21), 5229-5239.
29. Tao, Y.; Olson, N. H.; Xu, W.; Anderson, D. L.; Rossmann, M. G.; Baker, T. S., Assembly of a tailed bacterial virus and its genome release studied in three dimensions. *Cell* 1998, 95 (3), 431-437.

30. Schwartz, C.; De Donatis, G. M.; Zhang, H.; Fang, H.; Guo, P., Revolution rather than rotation of AAA+ hexameric phi29 nanomotor for viral dsDNA packaging without coiling. *Virology* 2013, 443 (1), 10.1016/j.virol.2013.04.019.
31. Zhao, Z.; Khisamutdinov, E.; Schwartz, C.; Guo, P., Mechanism of one-way traffic of hexameric phi29 DNA packaging motor with four electropositive relaying layers facilitating antiparallel revolution. *ACS Nano* 2013, 7 (5), 4082-92.
32. Guo, P., Biophysical studies reveal new evidence for one-way revolution mechanism of bacteriophage varphi29 DNA packaging motor. *Biophysical Journal* 2014, 106 (9), 1837-8.
33. Koti, J.; Morais, M.; Rajagopal, R.; Owen, B.; McMurray, C.; Anderson, D., DNA packaging motor assembly intermediate of bacteriophage phi29. *Journal of Molecular Biology* 2008, 381 (5), 1114-32.
34. Zhao, Z.; De-Donatis, G. M.; Schwartz, C.; Fang, H.; Li, J.; Guo, P., An arginine finger regulates the sequential action of asymmetrical hexameric ATPase in the double-stranded DNA translocation motor. *Molecular and Cellular Biology* 2016, 36 (19), 2514-2523.
35. Guasch, A.; Pous, J.; Ibarra, B.; Gomis-Rüth, F. X.; Valpuesta, J. M. a.; Sousa, N.; Carrascosa, J. L.; Coll, M., Detailed architecture of a DNA translocating machine: The high-resolution structure of the bacteriophage ϕ 29 connector particle. *Journal of Molecular Biology* 2002, 315 (4), 663-676.
36. Guo, P.; Peterson, C.; Anderson, D., Initiation events in in-vitro packaging of bacteriophage phi 29 DNA-gp3. *Journal of Molecular Biology* 1987, 197 (2), 219-228.
37. Anderson, D.; Bodley, J., Role of RNA in bacteriophage phi29 DNA packaging. *Journal of Structural Biology* 1990, 104, 70-74.
38. Wichitwechkarn, J.; Bailey, S.; Bodley, J.; Anderson, D., Prohead RNA of bacteriophage phi29: Size, stoichiometry and biological activity. *Nucleic Acids Research* 1989, 17 (9), 3459-3468.
39. Bailey, S.; Wichitwechkarn, J.; Johnson, D.; Reilly, B.; Anderson, D.; Bodley, J., Phylogenetic analysis and secondary structure of the *Bacillus subtilis* bacteriophage RNA required for DNA packaging. *Journal of Biological Chemistry* 1990, 265, 22365-22370.

40. Reid, R.; Bodley, J.; Anderson, D., Identification of bacteriophage phi 29 prohead RNA domains necessary for in vitro DNA-gp3 packaging. *Journal of Biological Chemistry* 1994, 269, 9084-9089.
41. Reid, R.; Bodley, J.; Anderson, D., Characterization of the prohead-pRNA interaction of bacteriophage phi 29. *Journal of Biological Chemistry* 1994, 269, 5157-5162.
42. Zhang, C.; Lee, C.; Guo, P., The proximate 5' and 3' ends of the 120-base viral RNA (pRNA) are crucial for the packaging of bacteriophage phi 29 DNA. *Virology* 1994, 201 (1), 77-85.
43. Zhang, C.; Tellinghuisen, T.; Guo, P., Confirmation of the helical structure of the 5'/3' termini of the essential DNA packaging pRNA of phage phi 29. *RNA* 1995, 1 (10), 1041-1050.
44. Gu, X.; Schroeder, S., Different sequences show similar quaternary interaction stabilities in prohead viral RNA self-assembly. *Journal of Biological Chemistry* 2011, 286, 14419-14426.
45. Chen, C.; Zhang, C.; Guo, P., Sequence requirement for hand-in-hand interaction in formation of RNA dimers and hexamers to gear phi29 DNA translocation motor. *RNA* 1999, 5 (6), 805-18.
46. Zhang, C.; Tellinghuisen, T.; Guo, P., Use of circular permutation to assess six bulges and four loops of DNA-packaging pRNA of bacteriophage phi29. *RNA* 1997, 3, 315-323.
47. Reid, R.; Zhang, F.; Benson, S.; Anderson, D., Probing the structure of bacteriophage phi29 prohead RNA with specific mutations. *Journal of Biological Chemistry* 1994, 269, 18656-18661.
48. Zhao, W.; Saha, M.; Ke, A.; Morais, M.; Jardine, P.; Grimes, S., A three-helix junction is the interface between two functional domains of prohead RNA in phi29 DNA packaging. *Journal of Virology* 2012, 86, 11625-11632.
49. Hao, Y.; Kieft, J. S., Diverse self-association properties within a family of phage packaging RNAs. *RNA* 2014, 20, 1-16.

50. Trotter, M.; Guo, P., Approaches to determine stoichiometry of viral assembly components. *Journal of Virology* 1997, 71 (1), 487-494.
51. Ding, F.; Lu, C.; Zhao, W.; Rajashankar, K.; Anderson, D.; Jardine, P.; Grimes, S.; Ke, A., Structure and assembly of the essential RNA ring component of a viral DNA packaging motor. *Proceedings of the National Academy of Sciences* 2011, 108, 7357-7362.
52. Guo, P.; Zhang, C.; Chen, C.; Garver, K.; Trotter, M., Inter-RNA interaction of phage phi29 pRNA to form a hexameric complex for viral DNA transportation. *Molecular Cell* 1998, 2, 149-155.
53. Harris, S.; Schroeder, S., Nuclear magnetic resonance structure of the prohead RNA E-loop hairpin. *Biochemistry* 2010, 49 (29), 5989-97.
54. Zhang, H.; Endrizzi, J.; Shu, Y.; Haque, F.; Sauter, C.; Shlyakhtenko, L.; Lyubchenko, Y.; Guo, P.; Chi, Y., Crystal structure of 3WJ core revealing divalent ion-promoted thermostability and assembly of the Phi29 hexameric motor pRNA. *RNA* 2013, 19, 1226-1237.
55. Zhang, X.; Tung, C.-S.; Sowa, G. Z.; Hatmal, M. M.; Haworth, I. S.; Qin, P. Z., Global structure of a three-way junction in a phi29 packaging RNA dimer determined using site-directed spin labeling. *Journal of the American Chemical Society* 2012, 134 (5), 2644-2652.
56. Harjes, E.; Kitamura, A.; Zhao, W.; Morais, M.; Jardine, P.; Grimes, S.; Matsuo, H., Structure of the RNA claw of the DNA packaging motor of bacteriophage Phi29. *Nucleic Acids Research* 2012, 40 (19), 9953-63.
57. Guo, P.; Grainge, I.; Zhao, Z.; Vieweger, M., Two classes of nucleic acid translocation motors: Rotation and revolution without rotation. *Cell & Bioscience* 2014, 4 (54).
58. Rao, V.; Feiss, M., The bacteriophage DNA packaging motor. *Annual Review of Genetics* 2008, 42, 647-681.
59. Atkins, J.; Gesteland, R.; Cech, T., *RNA Worlds: From Life's Origins to Diversity in Gene Regulation*. Cold Spring Harbor Press: 2010.

60. Strulson, C. A.; Molden, R. C.; Keating, C. D.; Bevilacqua, P. C., RNA catalysis through compartmentalization. *Nature Chemistry* 2012, 4 (11), 941-946.
61. Kitamura, A.; Jardine, P. J.; Anderson, D. L.; Grimes, S.; Matsuo, H., Analysis of intermolecular base pair formation of prohead RNA of the phage ϕ 29 DNA packaging motor using NMR spectroscopy. *Nucleic Acids Research* 2008, 36 (3), 839-848.
62. Wilson, T. J.; Lilley, D. M., Do the hairpin and VS ribozymes share a common catalytic mechanism based on general acid–base catalysis? A critical assessment of available experimental data. *RNA* 2011, 17 (2), 213-221.
63. Walter, N.; Burke, J.; Millar, D., Stability of hairpin ribozyme tertiary structure is governed by the interdomain junction. *Nature Structural Biology* 1999, 6 (6), 544-9.
64. Tan, E.; Wilson, T.; Nahas, M.; Clegg, R.; Lilley, D.; Ha, T., A four-way junction accelerates hairpin ribozyme folding via a discrete intermediate. *Proceedings of the National Academy of Sciences of the United States of America* 2003, 100 (16), 9308-13.
65. Müller, S.; Appel, B.; Krellenberg, T.; Petkovic, S., The many faces of the hairpin ribozyme: Structural and functional variants of a small catalytic RNA. *IUBMB Life* 2012, 64 (1), 36-47.
66. Lescoute, A.; Westhof, E., Topology of three-way junctions in folded RNAs. *RNA* 2006, 12, 83-93.
67. Seeman, N., DNA in a material world. *Nature* 2003, 421, 427-431.
68. Lin, C.; Liu, Y.; Rinker, S.; Yan, H., DNA tile based self-assembly: Building complex nano-architectures. *ChemPhysChem* 2006, 7, 1641-1647.
69. Feldkamp, U.; Niemeyer, C., Rational design of DNA nanoarchitectures. *Angewandte Chemie International Edition* 2006, 45, 1856-1876.
70. Douglas, S.; Bachelet, I.; Church, G., A logic-gated nanorobot for targeted transport of molecular payloads. *Science* 2012, 335 (6070), 831-834.

71. Ko, S.; Su, M.; Zhang, C.; Rbbe, A.; Jiang, W.; Mao, C., Synergistic self-assembly of RNA and DNA molecules. *Nature Chemistry* 2010, 2, 1050-1055.
72. Ishikawa, J.; Furuta, H.; Ikawa, Y., RNA Tectonics (tectoRNA) for RNA nanostructure design and its application in synthetic biology. *Wiley Interdisciplinary Reviews: RNA* 2013, 4 (6), 651-664.
73. Geary, C.; Rothmund, P.; Andersen, E., A single-stranded architecture for cotranscriptional folding of RNA nanostructures. *Science* 2014, 345 (6198), 799-804.
74. Lee, J. B.; Hong, J.; Bonner, D. K.; Poon, Z.; Hammond, P. T., Self-assembled RNA interference microsponges for efficient siRNA delivery. *Nature Materials* 2012, 11 (4), 316-322.
75. Shu, D.; Moll, W. D.; Deng, Z.; Mao, C.; Guo, P., Bottom-up assembly of RNA arrays and superstructures as potential parts in nanotechnology. *Nano Letters* 2004, 4 (9), 1717-1723.
76. Guo, S.; Tschammer, N.; Mohammed, S.; Guo, P., Specific delivery of therapeutic RNAs to cancer cells via the dimerization mechanism of phi29 motor pRNA. *Human Gene Therapy* 2005, 16, 1097-1109.
77. Haque, F.; Shu, D.; Shu, Y.; Shlyakhtenko, L.; Rychahou, P.; Evers, B.; Guo, P., Ultrastable synergistic tetravalent RNA nanoparticles for targeting to cancers. *Nano Today* 2012, 7 (4), 245-257.
78. Shu, Y.; Haque, F.; Shu, D.; Li, W.; Zhu, Z.; Kotb, M.; Lyubchenko, Y.; Guo, P., Fabrication of 14 different RNA nanoparticles for specific tumor targeting without accumulation in normal organs. *RNA* 2013, 19 (6), 767-777.
79. Shu, D.; Zhang, H.; Jin, J.; Guo, P., Counting of six pRNAs of phi29 DNA-packaging motor with customized single-molecule dual-view system. *The EMBO Journal* 2007, 26, 527-537.
80. Ibarra, B.; Caston, J.; Llorca, O.; Valle, M.; Valpuesta, J.; Carrascosa, J., Topology of the components of the DNA packaging machinery in the phage phi29 prohead. *Journal of Molecular Biology* 2000, 298 (5), 807-15.

81. Morais, M.; Koti, J.; Bowman, V.; Reyes-Aldrete, E.; Anderson, D.; Rossmann, M., Defining molecular and domain boundaries in the bacteriophage phi29 DNA packaging motor. *Structure* 2008, 16, 1267-1274.
82. Simpson, A. A.; Tao, Y.; Leiman, P. G.; Badasso, M. O.; He, Y.; Jardine, P. J.; Olson, N. H.; Morais, M. C.; Grimes, S.; Anderson, D. L.; Baker, T. S.; Rossmann, M. G., Structure of the bacteriophage ϕ 29 DNA packaging motor. *Nature* 2000, 408 (6813), 745-750.
83. Zhang, F.; Lemieux, S.; Wu, X.; St.-Arnaud, D.; McMurray, C. T.; Major, F.; Anderson, D., Function of hexameric RNA in packaging of bacteriophage ϕ 29 DNA in vitro. *Molecular Cell* 1998, 2 (1), 141-147.

Chapter 3: Thermodynamic Stabilities of Three-Way Junction

Nanomotifs in Prohead RNA

The following chapter was published in similar form in *RNA* by the author of this dissertation. All text and figures are taken with the permissions of a Creative Commons license.

Abstract

The thermodynamic stabilities of four natural prohead or packaging RNA (pRNA) three-way junction (3WJ) nanomotifs and seven phi29 pRNA 3WJ deletion mutant nanomotifs were investigated using UV optical melting on a three-component RNA system. Our data reveal that some pRNA 3WJs are more stable than the phi29 pRNA 3WJ. The stability of the 3WJ contributes to the unique self-assembly properties of pRNA. Thus, ultrastable pRNA 3WJ motifs suggest new scaffolds for pRNA-based nanotechnology. We present data demonstrating that pRNA 3WJs differentially respond to the presence of metal ions. A comparison of our data with free energies predicted by currently available RNA secondary structure prediction programs shows that these programs do not accurately predict multibranch loop stabilities. These results will expand the existing parameters used for RNA secondary structure prediction from sequence in order to better inform RNA structure-function hypotheses and guide the rational design of functional RNA supramolecular assemblies.

Introduction

Multibranch loops are key determinants of structural and functional roles in RNA. In prohead RNA (pRNA), an essential component of the phi29-like bacteriophage DNA packaging motor², the three-way junction (3WJ) is a multibranch loop that is a flexible,

dynamic region in the RNA ⁴⁻⁶ that helps to correctly place helices in the spatial orientation necessary for packaging ⁷⁻¹⁰. *In vitro*, pRNA self-assembles, with some sequences capable of forming dimers, trimers, and higher order multimers depending on the assembly conditions used. Recent studies have shown that the SF5 and M2 pRNAs have the highest propensities for *in vitro* self-assembly ^{3, 11}. The shape, self-assembly properties, and stability of pRNA can be leveraged in the rational design of functional supramolecular structures, including polyvalent nanoscale delivery systems ¹³⁻²⁴. However, an important consideration in the design of functional nanostructures is the stability of the pRNA "building block" ²⁴⁻²⁶.

Different pRNAs share only 12% sequence similarity, but pRNA secondary structure and function are conserved ³. Although different pRNAs have different interlocking loop sequences and therefore different interlocking loop stabilities, the overall energetics for pRNA dimerization are also conserved, suggesting that another pRNA nanomotif plays a compensatory role in stabilizing the RNA ³. Studies on designer pRNA sequences, which retained only the wild-type (WT) interlocking loops and 3WJ sequences but changed the sequences in the Watson-Crick pairs, indicated that helices do not contribute to pRNA assembly in a sequence-dependent fashion ⁸. Studies that mixed pRNA interlocking loops and 3WJs revealed similar insights, demonstrating that mediocre loop-loop interactions can be overcome with highly stable scaffolds ¹¹. These results implicate the 3WJ as an important contributor to pRNA self-assembly.

Using a three-component RNA system designed for UV optical melting ²⁷⁻²⁸ (Figure 1), we measured the thermodynamic parameters for four natural pRNA 3WJs and seven mutated phi29 pRNA 3WJs. Here, we report the thermodynamic stabilities

for these pRNA 3WJ sequences. Our results show that the GA1, SF5, and M2 pRNA 3WJs are more stable than the WT phi29 pRNA 3WJ commonly used as a scaffold in RNA-based nanotechnology. Furthermore, we show that certain deletions at the phi29 pRNA 3WJ increase its stability relative to WT. Finally, we show that metal ions have a differential stabilizing effect on pRNA 3WJs, and we demonstrate the need for improved RNA secondary structure stability predictions for multibranch loops. This work extends our knowledge of the biophysical properties of pRNA and provides a foundation for further investigation into the viability of other, underexplored pRNA 3WJ nanomotifs in the rational design of functional RNA supramolecular structures.

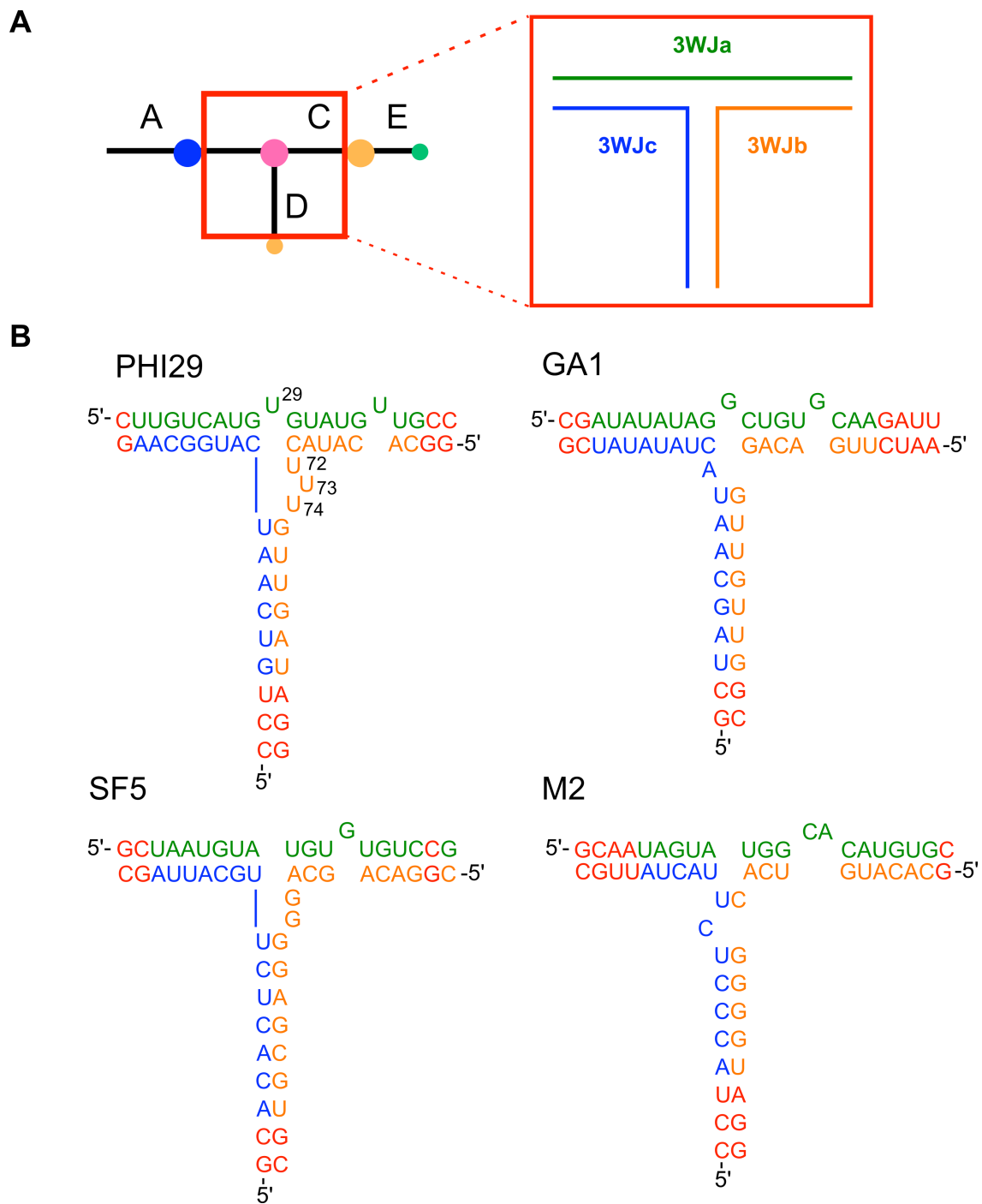


Figure 1 (A) Ball-and-stick model of pRNA, where balls represent loops and sticks represent helices. The pRNA 3WJ nanomotif, inset, comprises strands 3WJa (green), 3WJb (orange), and 3WJc (blue). **(B)** pRNA 3WJ constructs' primary and secondary structures²⁹ where strand 3WJa is in green, 3WJb is in orange, and 3WJc is in blue. Changes to WT sequences are indicated in red. Nucleotides deleted in the phi29 pRNA 3WJ are labeled. Figure originally published in¹².

Results

pRNA 3WJ Nanomotif Stabilities

Thermodynamic parameters determined by UV optical melting for each construct and its respective 3WJ nanomotif are reported in Table 1. The GA1, SF5, and M2 pRNA 3WJs showed greater stability than the phi29 pRNA 3WJ (Table 1).

Melt curves showed very sharp transitions, supporting the assumption of a cooperative transition from the RNA triplex to single-stranded RNAs (Figure 2A). None of the single strand or pairwise combination melts showed a significant transition that would compete with the 3WJ (Appendix I Figures 1 and 2). For example, a melt of phi29 strands 3WJa and 3WJb showed a transition with a melting temperature of 51°C, while the complete 3WJ (*i.e.*, strands 3WJa, 3WJb, and 3WJc together) showed a transition with a melting temperature of 56°C (Appendix I Figure 2). However, formation of the 3WJ is favored when all three strands are present. As previously shown for non-self-complementary RNA duplexes, the non-self-complementary duplex will form even when the T_m for an alternative conformation of a single strand forming a self-complementary duplex has a higher T_m if the enthalpy is more favorable for the non-self-complementary duplex³⁰ (Appendix I Table 3). Free energies for the constructs and their respective 3WJs were calculated from van't Hoff plots, where the goodness of linear fit was ≥ 0.90 for all melts (Figure 2B). The free energies for the investigated 3WJs range from -9.9 kcal/mol to 10.2 kcal/mol. By comparison, 1.4 kcal/mol at 37°C is approximately one order of magnitude in a binding constant. Thus, the range of free energies of formation for the investigated 3WJs spans 14 orders of magnitude in terms of binding constants.

Table 1 Thermodynamic parameters for pRNA constructs and 3WJ nanomotifs. Bulge nucleotides are underlined. The errors in enthalpy, entropy, and free energy are estimated to be 10%, 10%, and 5%, respectively.³¹.

Construct	Sequence	ΔH (kcal mol ⁻¹)	ΔS (kcal mol ⁻¹)	ΔG_{37} (kcal mol ⁻¹)	ΔG_{37} , 3WJ (kcal mol ⁻¹)
Phi29	5'-CUUGUCAUGU <u>UA</u> UGCC-3'	-230.8	-658.7	-26.5	4.6
	5'-GGCACAU <u>ACU</u> UUUU <u>GA</u> UAGG-3'				
	5'-CCUGUCA <u>AAU</u> CGGCAAG-3'				
GAI	5'-CGAU <u>AAU</u> AGGCGUGGCAAGUUU-3'	-317.9	-935.0	-27.9	1.9
	5'-AAUCU <u>GGAC</u> AGGUUGGCG-3'				
	5'-GCUAG <u>CAAU</u> ACU <u>AAU</u> AUUCG-3'				
SF5	5'-GCUAA <u>AGUA</u> UGUGUCCG-3'	-336.1	-970.7	-35.0	-4.3
	5'-CGGAC <u>AGCAG</u> GGGAGCGUUGC-3'				
	5'-GCAC <u>ACUCU</u> UGCAUAGC-3'				
M2	5'-GCAA <u>AGUA</u> GGCACAUUGC-3'	-350.7	-1002.1	-39.9	-9.9
	5'-GCAC <u>U<u>GU</u>CA</u> CGGGUAGG-3'				
	5'-CCU <u>ACCU</u> U <u>ACU</u> AUUUGC-3'				
Phi29 _{A129}	5'-CUUGUCAUGGUAUGUUGCC-3'	-215.6	-611.9	-25.8	5.3
	5'-GGCACAU <u>ACU</u> UUUU <u>GA</u> UAGG-3'				
	5'-CCUGCA <u>AAU</u> CAU <u>GGCA</u> AG-3'				
Phi29 _{A129/A172}	5'-CUUGUCAUGGUAUGUUGCC-3'	-201.6	-566.8	-25.8	5.3
	5'-GGCACAU <u>ACU</u> UUUU <u>GA</u> UAGG-3'				
	5'-CCUGCA <u>AAU</u> CAU <u>GGCA</u> AG-3'				
Phi29 _{A129/A172/33}	5'-CUUGUCAUGGUAUGUUGCC-3'	-302.3	-863.8	-34.4	-3.3
	5'-GGCACAU <u>ACU</u> UUUU <u>GA</u> UAGG-3'				
	5'-CCUGCA <u>AAU</u> CAU <u>GGCA</u> AG-3'				
Phi29 _{A129/A172/33/74}	5'-CUUGUCAUGGUAUGUUGCC-3'	-291.6	-841.7	-30.5	0.6
	5'-GGCACAU <u>ACU</u> UUUU <u>GA</u> UAGG-3'				
	5'-CCUGCA <u>AAU</u> CAU <u>GGCA</u> AG-3'				
Phi29 _{A172}	5'-CUUGUCAUGGUAUGUUGCC-3'	-225.4	-641.5	-26.4	4.7
	5'-GGCACAU <u>ACU</u> UUUU <u>GA</u> UAGG-3'				
	5'-CCUGCA <u>AAU</u> CAU <u>GGCA</u> AG-3'				
Phi29 _{A172/33}	5'-CUUGUCAUGGUAUGUUGCC-3'	-124.2	-333.1	-20.9	10.2
	5'-GGCACAU <u>ACU</u> UUUU <u>GA</u> UAGG-3'				
	5'-CCUGCA <u>AAU</u> CAU <u>GGCA</u> AG-3'				
Phi29 _{A172/33/74}	5'-CUUGUCAUGGUAUGUUGCC-3'	-209.5	-592.3	-25.8	5.3
	5'-GGCACAU <u>ACU</u> UUUU <u>GA</u> UAGG-3'				
	5'-CCUGCA <u>AAU</u> CAU <u>GGCA</u> AG-3'				

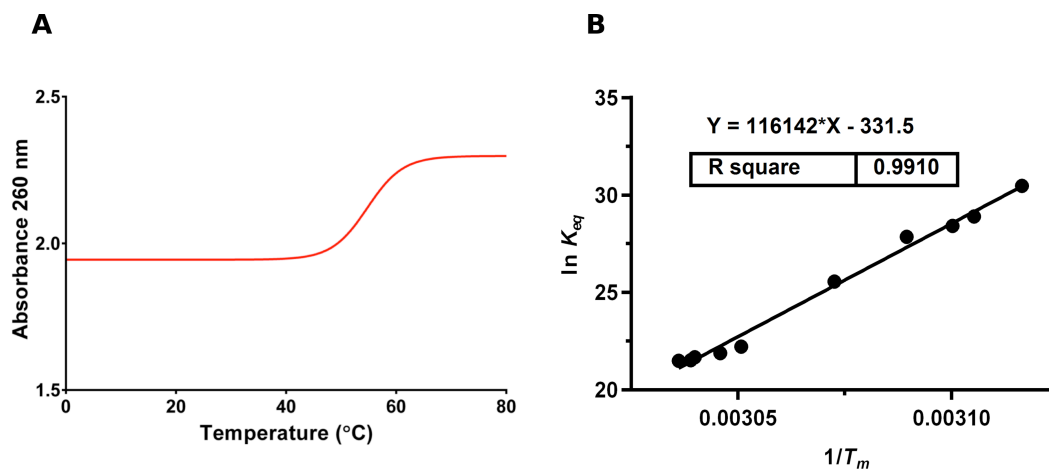


Figure 2 (A) Nonlinear melt curve fit ($R^2 > 0.99$) for the WT phi29 3WJ construct collected at 31.2 μM showing a sharp, cooperative transition. Data points were collected at a rate of 6/s with a heating rate of 1°C/min. (B) van't Hoff plot of phi29 3WJ melt data ($R^2 > 0.99$), where the slope is $-\Delta H/R$ and the y-intercept is $\Delta S/R$. Data were fit using the Marquardt-Levenberg method in Meltwin³². Figure originally published in¹².

The phi29 pRNA 3WJ is stabilized when certain uridine (U) residues are deleted from the junction. Specifically, the following two deletion combinations increased stability relative to the WT phi29 pRNA 3WJ: (1) Deletion of a single U bulge (U29) in strand 3WJa along with two of the three U residues in the tri-U bulge in strand 3WJb (*i.e.*, U72-73-74); and (2) Deletion of all bulge U residues at the 3WJ (*i.e.*, U29/U72-73-74)³³ (Table 1, Figure 1B). Other investigated deletions either did not significantly affect the stability of the phi29 pRNA 3WJ or actively destabilized it (Table 1).

Of the four RNA secondary structure prediction programs used, none accurately predicted either the actual free energies of the junctions or variations in phi29 pRNA mutant 3WJ stabilities (Figure 3, Appendix I Table 1). Best predictions ranged from within 1 kcal/mol of the measured free energy (for phi29 Δ U29/ Δ U72-73-74, by RNAsoft) to 9 kcal/mol (for phi29 Δ U72-73, by RNAfold), while worst predictions

ranged from within 1 kcal/mol (for phi29 Δ U29/ Δ U72-73-74, by RNAsoft) to 11 kcal/mol (for phi29 Δ U72-73, by RNAfold). At best, the prediction programs were off by an average of 4 (\pm 2) kcal/mol from measured free energies.

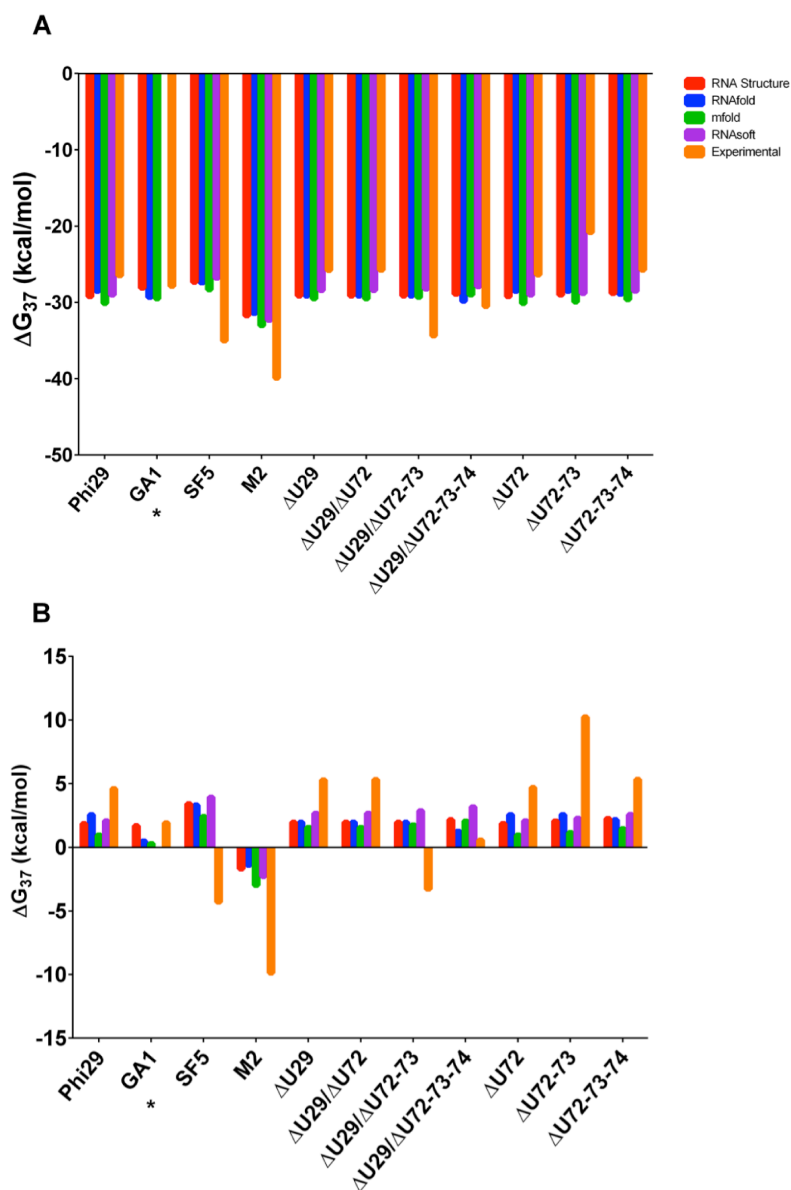


Figure 3 (A) Measured thermodynamic stabilities and secondary structure free energy predictions for pRNA 3WJ constructs using RNA Structure³⁴, RNAfold³⁵, mfold³⁶, and RNAsoft³⁷. (B) Calculated 3WJ nanomotif thermodynamic stabilities and secondary structure free energy predictions using the same programs. *RNAsoft did not output a secondary structure free energy for the GA1 pRNA 3WJ due to computer run-time limitations. Figure originally published in¹².

Metal Ion Binding

The effects of Na^+ , Mg^{2+} , and spermidine (a plus 3 charged species) on pRNA 3WJ stabilities are depicted in Figure 4. Complete thermodynamic parameters are provided in Appendix I Table 2. Relative to 100 mM NaCl, the phi29 pRNA 3WJ construct was nearly equally stabilized by Mg^{2+} and spermidine, while the GA1, SF5, and M2 pRNA 3WJs were differentially affected by these ions. Addition of Mg^{2+} stabilized both the SF5 and M2 pRNA 3WJs. The addition of spermidine had an increasing stabilizing effect on the GA1, SF5, and M2 pRNA 3WJs, respectively (Figure 4).

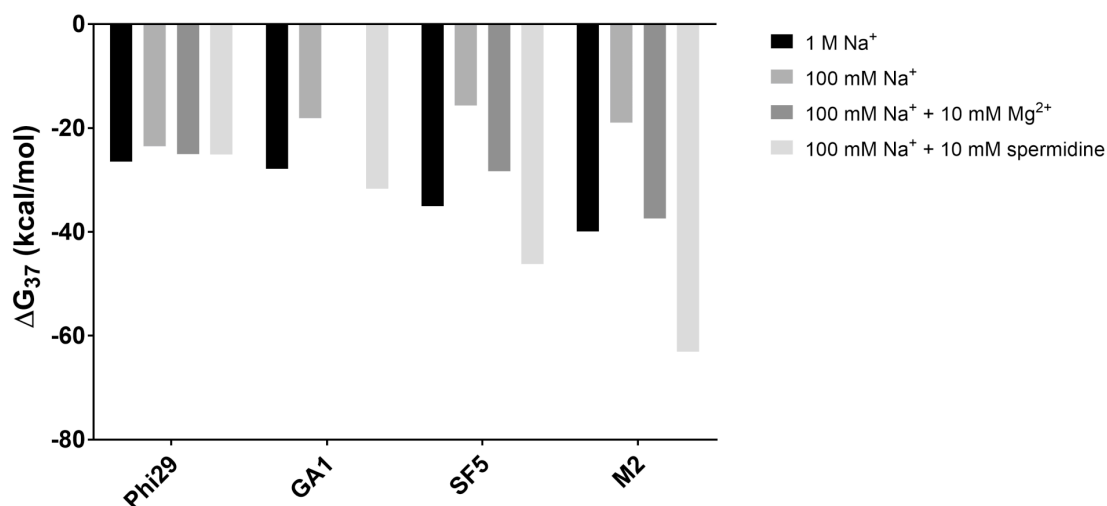


Figure 4 Metal ion effects on natural pRNA 3WJ constructs. Optical melts of the GA1 3WJ in 100 mM Na^+ and 10 mM Mg^{2+} did not meet the van't Hoff plot goodness of linear fit cutoff criterion of ≥ 0.90 . Figure originally published in ¹².

Electrophoretic Gel Mobility Shift Assays

A gel depicting the mobility of all pRNA 3WJs under standard melt buffer conditions (1 M sodium chloride, 10 mM sodium cacodylate, 0.5 mM EDTA, pH 7.0) relative to a single strand (phi29 3WJa) and a pairwise combination (phi29 3WJa + 3WJb) is shown in Figure 5. All assembled 3WJs run at approximately the same rate. Additionally, gels

depicting the mobility of each pRNA 3WJ construct relative to each single RNA strand and all pairwise combinations in TMS buffer (50 mM Tris-HCl, pH 7.8, 100 mM NaCl, 10 mM MgCl₂) are shown in Appendix I Figure 3 for the purpose of comparison to previous work published on the assembly and stabilities of various biological RNAs²⁵. For each gel, mobility decreased as more components of the RNA system were added. Single strands showed the fastest migration and pairwise combinations showed intermediate migration relative to a slow-migrating band that appeared when all three RNA 3WJ strands were present (Figure 5, Appendix I Figure 3), indicating that the three RNA components interact more favorably than any two components, and confirming formation of the pRNA 3WJ from strands 3WJa, 3WJb, and 3WJc.

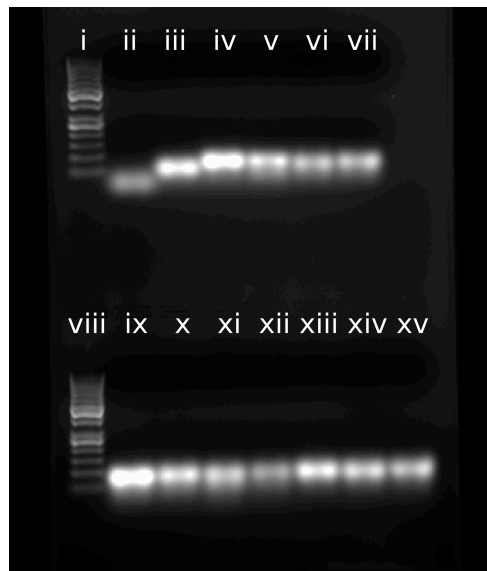


Figure 5 Gel mobility of 50 bp ladder (Lanes i and viii), Phi29 strand 3WJa (Lane ii), Phi29 strands 3WJa + 3WJb (Lane iii), Phi29 3WJ (Lane iv), GA1 3WJ (Lane v), SF5 3WJ (Lane vi), M2 3WJ (Lane vii), Phi29ΔU29 (Lane ix), Phi29ΔU29/ΔU72 (Lane x), Phi29ΔU29/ΔU72-73 (Lane xi), Phi29ΔU29/ΔU72-73-74 (Lane xii), Phi29ΔU72 (Lane xiii), Phi29ΔU72-73 (Lane xiv), and Phi29ΔU72-73-74 (Lane xv). Assembly was performed in standard melt buffer (1 M NaCl, 10 mM sodium cacodylate, 0.5 mM EDTA, pH 7) to confirm formation of the 3WJs under optical melting conditions. Phi29 strand 3WJa (Lane ii) and strands 3WJa + 3WJb (Lane iii) were included as references. All 3WJs run at approximately the same rate. Figure originally published in¹².

Discussion

3WJ Stabilities in Relation to Loop-Loop Interaction Stabilities and Self-Assembly

Among the investigated pRNA 3WJ constructs, the SF5 and M2 pRNA 3WJs were most thermodynamically stable, making them attractive alternatives to the phi29 pRNA 3WJ scaffold used in pRNA-based nanotechnology. Interestingly, these pRNAs also have shown the highest propensity for self-assembly under the laboratory conditions studied thus far^{3, 11}. Analyses of our measured 3WJ stabilities with loop-loop interaction stabilities calculated from sequences provided by Gu and Schroeder³ and Hao and Kieft¹¹ provide insights into whether the 3WJ nanomotif plays a compensatory role in stabilizing pRNA. The analyses indicated that while loop-loop interactions are all favorable, 3WJs have a wider range of stabilities (Figure 6). Specifically, the phi29 and GA1 pRNAs have unfavorable 3WJ stabilities, while the M2 and SF5 pRNAs have favorable 3WJ stabilities (Figure 6). For phi29 and GA1 pRNAs, the loop-loop interaction stabilities are offset by 3WJ stabilities, while for SF5 and M2 pRNAs, the loop-loop interactions and the 3WJ are both stabilizing. The combination of stabilizing nanomotifs may help explain why only SF5 and M2 pRNAs have shown *in vitro* self-assembly of higher order multimers^{3, 11}. Recently, the M2 pRNA 3WJ was shown to favor a conformation that promotes higher-order multimer assembly³⁸. Furthermore, a chimeric pRNA where the phi29 3WJ was placed in the M2 architecture showed reduced assembly³⁸. Consistent with their increased thermodynamic stabilities and propensities to assemble into higher-order multimers relative to phi29, the SF5 and M2 sequences may both adopt 3WJ pre-organizations that do not require the disruption of existing coaxial stacking or other favorable interactions in order to self-assemble.

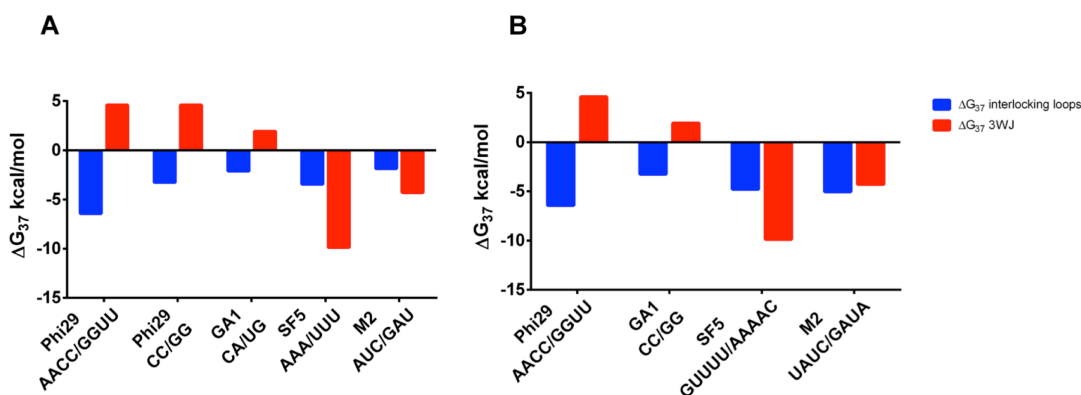


Figure 6 Experimental 3WJ data presented with interlocking loop stabilities calculated using the Nearest Neighbor Database¹ of sequences reported by (A) Gu and Schroeder³ and (B) Hao and Kieft¹¹. Interlocking loop sequences are provided for each pRNA. Both the experimental stability data and the calculated stability data were determined for RNA in 1 M NaCl. Figure originally published in¹².

In a recent study²⁶, a phi29 pRNA-derived construct retaining all U residues at the 3WJ was shown to be thermodynamically stable. Our results can be used to improve the efficiency of self-assembly in this system with specific U deletions at the 3WJ that increase its stability. Here we show that the $\Delta U29/\Delta U72-73$ and $\Delta U29/\Delta U72-73-74$ deletions at the phi29 pRNA 3WJ are stabilizing (Table 1), suggesting alternatives to WT phi29 pRNA scaffolds in the rational design of functional RNAs. Although no clear pattern emerges for any correlation between the number of nucleotides at the 3WJ and the stability of the 3WJ, the deletions may affect helix stacking such that favorable stacking stabilizes the junction, while unfavorable stacking destabilizes the junction. Favorable stacking may account for some, but not all, of the stability differences observed. For example, free energies of helix stacking in a two-component 3WJ

construct range from -3.4 to -5.2 kcal/mol²⁸. A previous packaging study³³ on phi29 pRNA 3WJ deletion mutants reported that deletion of any two of the four bulge U residues at the junction (*i.e.*, U29/U72-73-74) supports pRNA binding to the viral prohead as well as WT levels of DNA packaging. *In vivo*, it is possible that individual pRNAs are further stabilized by their interactions with other pRNAs, proteins, or metal ions.

Structure-Energetics Relationships in the pRNA 3WJ

Two crystal structures have captured snapshots of the structures of the phi29 pRNA 3WJ. The two crystal structures have different space groups, crystal packing, resolution, helix orientations, sequence modifications, and metal ion binding sites but share in common the coaxial stacking of helices A and D (Figure 1A). A truncated phi29 construct with interlocking loops at 3.5 Å shows metal ions bound near the GU closing pair of the 3WJ in the native sequence⁸. A three-component model for the phi29 pRNA 3WJ motif at 3.05 Å was stabilized by two divalent metal ions binding between two helices⁴. Comparison of the two metal-ion bound structures^{4,8} indicates a change in the A and D interhelical angle and helix distortion where the metal ions bind⁴. EPR methods determined another multibranch loop conformation in solution in a pRNA dimer in the presence of Mg²⁺⁵. Single molecule FRET analysis revealed the dynamic structural changes in this 3WJ when Mg²⁺ was added⁴. Despite the differences in techniques and constructs, metal ion binding at the 3WJ is a common feature in all of these structural studies.

Our thermodynamic data on constructs based on the 3-component model of the 3WJ show that Mg²⁺ and spermidine (an aliphatic amine and trivalent ion) nearly

equally stabilize the phi29 3WJ (Figure 4, Appendix I Table 2). An important consideration when comparing our data to the construct crystallized with divalent metal ions is a mutation in one of the four nucleotides shown to chelate the ions. In the crystallized construct, nucleotides G23/A90 and C24/A89 were shown to bind one divalent ion each ⁴. However, the cytidine at position 24 (C24) was mutated from the uridine found in WT phi29 pRNA and in the constructs used in this study ⁴ (Figure 1B). Metal ions may help stabilize different sequences in different ways, but they may ultimately serve a similar structural and energetic role.

The crystallized 3WJ core and the new thermodynamic data presented here provide a foundation for inferences about RNA structure-energetics relationships, especially for the four bulge U residues at the 3WJ. Non-Watson-Crick base pairing predominates in RNA 3D structure, forming motifs that facilitate RNA-RNA interactions and bind ligands ³⁹⁻⁴⁰. The phi29 3WJ crystal structure ⁴ revealed the formation of a *cis* base pair between the Watson-Crick edges of U29 and U72 as well as base stacking between U29 and U74 (Figure 7B) ^{4, 40}. By comparison, the phi29 pRNA 3WJ constructs in which U29 and at least one of the three U residues in the tri-U bulge (*i.e.*, U72-73-74) were retained did not appear to have equivalent thermodynamic stabilities (Appendix I Table 1), despite the possibility of base pair formation across these constructs' 3WJs. However, the stability of a 3WJ where U29 and two of the three U residues in the tri-U bulge were retained was nearly equal to that of the WT phi29 pRNA 3WJ (4.7 vs. 4.6 kcal/mol, respectively). This could suggest that base pair formation and base stacking are preserved in this 3WJ construct. Interestingly, notable increases in the stability of the phi29 pRNA 3WJ occurred only when one of the U

residues in the tri-U bulge was retained (-3.3 kcal/mol), or when all bulge U residues at the 3WJ were deleted (0.6 kcal/mol). Neither of these 3WJs would permit the observed base pairing or base stacking between U residues across the junction, suggesting that pairing and stacking are not the only favorable tertiary interactions stabilizing the junction. These mutations may allow for different, favorable helical coaxial stacking interactions, which may contribute to the stability differences observed ⁴¹. Coaxial stacking in multibranch loops is very difficult to predict accurately, and it becomes more difficult with larger junctions that contain unpaired nucleotides ⁴². Thus, structural data on these constructs will be necessary to form a more complete picture of why some 3WJ sequences are more stable than others.

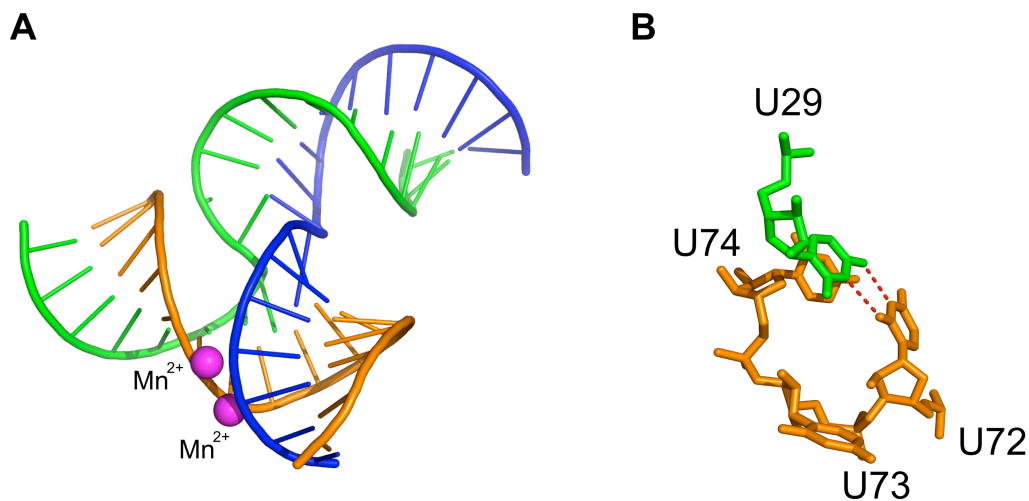


Figure 7 phi29 pRNA 3WJ structure ⁴. (A) 3WJa is in green, 3WJb is in orange, and 3WJc is in blue. Bound divalent metal ions (Mn²⁺) are in magenta. (B) Bulge residues at the 3WJ (*i.e.*, U29/U72-73-74) are shown as sticks. A cis base pair forms between the Watson-Crick edges ⁴⁰ of U29 and U72. U29 and U74 form a base stack. Figure originally published in ¹².

Future Improvements in Predicting RNA 3WJ Stabilities

Importantly, the free energy outputs by RNA secondary structure prediction programs can be improved for multibranch loops. While all of the programs implemented in this study utilize the same free energy database, the way that multibranch loops are predicted varies in different RNA structure prediction programs. The prediction may consider all possible conformations of coaxial stacking, include only the single most favorable coaxial stacking arrangement, or include knowledge-based parameters from analysis of known secondary structures^{34, 43-45}. None of the algorithms was able to account for the magnitude of differences observed among the measured stabilities of the investigated 3WJs. All programs overestimated the stabilities of the phi29 and GA1 pRNA 3WJ constructs and underestimated the stabilities of the SF5 and M2 pRNA 3WJ constructs (Figure 3, Appendix I Table 1). Furthermore, none of the programs' predictions discriminated between the stabilities of constructs with deletions at the phi29 pRNA 3WJ. For example, neither the mutant that was shown to have the highest stability, nor the mutant that was shown to have the lowest stability, was predicted as such (Figure 3, Appendix I Table 1). Instead, deletion mutants were all predicted to have roughly the same free energies (within ~1 kcal/mol). Compared to measured free energies, these predictions illustrate the need for refinement of the parameters used to make RNA secondary structure and free energy predictions from sequence. Our work sets the foundation for further studies on multibranch loops of different sizes, asymmetries, and sequences in order to develop more robust prediction rules.

Prohead RNA (pRNA) is an important component of the phi29-like bacteriophage DNA packaging motor. Due to its stability and self-assembling properties

in vitro, pRNA has been used successfully as a scaffold in the rational design of functional RNA supramolecular structures¹³⁻²⁴. Compared to phi29 pRNA, the stabilities of other natural and mutated pRNA sequences remain relatively underexplored²⁵⁻²⁶. In this study, we investigated the thermodynamic stabilities of four natural and seven mutated pRNA 3WJ nanomotifs. We show that the GA1, SF5, and M2 pRNA 3WJs, as well as two phi29 pRNA mutant 3WJs, are more stable than the WT phi29 pRNA 3WJ.

The results of our approach to determining 3WJ stabilities will be used to improve RNA secondary structure prediction from sequence. 3WJs are ubiquitous in natural RNA secondary structures but remain poorly predicted. Our work sets a foundation for better understanding the rules that govern 3WJ thermodynamic stabilities. Additionally, knowledge that the SF5 and M2 pRNA 3WJs and two phi29 pRNA mutant 3WJs are more stable relative to the WT phi29 pRNA 3WJ provides a solid foundation for increasing the sequence diversity and fine-tuning the stabilities of pRNA building blocks in RNA-based nanotechnology.

Materials and Methods

pRNA 3WJ Construct Design

The pRNA 3WJ can be assembled from three RNA oligomers mixed in equimolar concentrations^{4, 25-26, 46}. In contrast to UV optical melting studies performed on RNA 3WJs using only two strands²⁷⁻²⁸, the constructs investigated in this study were assembled from three RNA strands designated 3WJa, 3WJb, and 3WJc (Figure 1). Constructs were designed to encompass the 3WJ region of folded pRNA, excepting the A, CE, and D bulges, to form three helices of approximately equal free energies. The

designed pRNA 3WJ constructs retained as much sequence identity to WT pRNA as possible, and changes to WT sequences were made distal to the 3WJ "core" where necessary (Figure 1B) to ensure that the free energy of helix formation for each branch was within 0.1 kcal/mol. The predicted free energy for each branch duplex includes a helix initiation term that assumes two strands come together independently. This is an overestimation of the penalty of helix formation in the third branch because this branch should not have the same entropic penalty in the 3WJ. Thus, our calculated 3WJ free energies underestimate the stabilities of the 3WJs. Sequences for each construct are provided in Table 1. Oligonucleotides were purchased from IDT and prepared according to the manufacturer's instructions. Purity was confirmed to be >95% by ³²P labeling and gel electrophoresis.

UV Optical Melting

For each construct, the three RNA oligomers 3WJa, 3WJb, and 3WJc were mixed in equimolar concentrations spanning a 100-fold dilution range from 0.4 μ M to 40 μ M. UV optical melting was performed as described previously ⁴⁷, with variation in the analysis for a three-component RNA system ⁴⁸. Melts were carried out under standard melt buffer conditions (1 M sodium chloride, 10 mM sodium cacodylate, 0.5 mM EDTA, pH 7.0) ⁴⁹ using a Beckman Coulter DU-800 spectrophotometer. Absorbances at 260 and 280 nm were measured as a function of temperature from 4°C to 90°C, both the largest measurable temperature range and the range for which the midpoint and the constructs' expected T_m s were approximately equal ⁵⁰⁻⁵¹. In order to form reproducibly the lowest energy structure, RNA samples were heated to 90°C and slowly cooled prior to melting or the addition of magnesium ²⁷. The sodium chloride concentration was

reduced by an order of magnitude ⁵² for melts with 10 mM metal ions, but all other conditions remained the same. Due to the presence of EDTA, the effective Mg²⁺ concentration may have been slightly less than 10 mM. For each construct, optical melts of single RNA strands 3WJa, 3WJb, and 3WJc and all pairwise combinations were also performed (Appendix I Figures 1 and 2). Melt curves were fit using Meltwin ³² in order to determine melting temperatures, and thermodynamic parameters were determined from van't Hoff plots where the equilibrium constant K_{eq} was given by

$$\frac{1}{(C_T/2n)^{n-1}}$$

where C_T = total strand concentration and $n = 3$ for a trimolecular dissociation reaction with equilibria involving non-self-complementary sequences ⁴⁸, and where goodness of linear fit, a good estimate of error, was ≥ 0.90 ⁵⁰. Derivation of the equilibrium constant is provided in Supporting Information. The sharpness of the melting transition and the linearity of the van't Hoff plots suggest two-state melting; however, the assumption of $\Delta C_p = 0$ is not rigorously followed. Although the enthalpies show some temperature dependence, there is a large range of error in the enthalpy and heat capacity values. The errors in enthalpy and entropy are correlated, and thus, the free energy still provides a useful, predictive value. Furthermore, corrections for temperature-dependent changes in heat capacity have a small effect within error of the value for the final free energy of the multibranch loop motif, *i.e.*, < 0.5 kcal/mol ^{27, 53}. Thermodynamic stabilities of the pRNA 3WJ nanomotifs were calculated by subtracting the stability contributions of the RNA helices as calculated from the Nearest Neighbor Database ¹ (Table 1, Figure 3B).

pRNA 3WJ Secondary Structure and Free Energy Predictions

The secondary structure and stability of each pRNA construct was predicted using four RNA secondary structure prediction programs: RNA Structure³⁴, RNAfold³⁵, mfold³⁶, and RNAsoft³⁷. For predictions in RNA Structure, RNAfold, and mfold, pRNA strands 3WJa and 3WJb as well as 3WJb and 3WJc were joined with a 5' – aaaa – 3' hairpin and then the construct was folded as a single strand. Free energy predictions were not affected by the position of the hairpins, *i.e.*, whether the hairpins were placed between strands 3WJa and 3WJb and strands 3WJb and 3WJc, between strands 3WJb and 3WJc and strands 3WJc and 3WJa, or between strands 3WJc and 3WJa and strands 3WJa and 3WJb. For predictions in RNAsoft, pRNA strands 3WJa and 3WJb were joined with a 5' – aaaa – 3' hairpin and folded with strand 3WJc. Again, free energy predictions were not affected by the position of the hairpin, *i.e.*, whether the hairpin was placed between strands 3WJa and 3WJb, between strands 3WJb and 3WJc, or between strands 3WJc and 3WJa. For each construct, the most stable structure output by each program was the designed structure. No forced base pairs or single strand constraints were used. To correct for the added hairpins, two 5' – aaaa – 3' hairpin penalties were subtracted from the secondary structure stabilities output by RNA Structure, RNAfold, and mfold (Table S1). For stabilities predicted by RNAsoft, one 5' – aaaa – 3' hairpin penalty was subtracted¹ (Appendix I Table 1). Because the calculations made in Appendix I Table 1 take into account the initiation terms for the 3WJs, their free energies are accurate within error whether in the context of a single-stranded RNA, a duplex, or a three-component system. The entropic penalties for bringing together two oligomers are included in the free energy of initiation terms. The free energies of initiating an RNA

hairpin and RNA intermolecular interactions are 5.4 ± 0.2 kcal/mol to 6.4 ± 0.2 kcal/mol (spanning loop lengths $n=3$ to $n=9$) and 4.09 ± 0.2 kcal/mol, respectively ¹. Thus, while there is a substantial entropic energy difference in bringing together three oligonucleotide strands compared to a single strand self-folding, the calculation of the free energy of the multibranch loop accounts for this difference and makes comparison of the 3WJ motif comparable in different contexts.

Electrophoretic Gel Mobility Shift Assays

Formation of the pRNA 3WJ constructs was monitored using electrophoretic gel mobility shift assays (EMSAs). RNA at a concentration of 40 μ M in standard melt buffer (1 M sodium chloride, 10 mM sodium cacodylate, 0.5 mM EDTA, pH 7.0) was heated to 80°C for 10s and then cooled to 4°C at a rate of 0.1°C/s in an MJ Research PTC-200 Peltier Thermal Cycler. The RNA was mixed with sucrose loading dye and run in TAE buffer at 50V and 4°C in pre-cooled, 2% (w/v) agarose stained with ethidium bromide. Mobility of a single RNA strand (phi29 3WJa), a pairwise combination (phi29 3WJa + 3WJb), and all assembled pRNA 3WJs were monitored. RNA at a concentration of 10 μ M in TMS buffer (50 mM Tris-HCl, pH 7.8, 100 mM NaCl, 10 mM MgCl₂) was heated to 80°C for 10s and then cooled to 4°C at a rate of 0.1°C/s in an MJ Research PTC-200 Peltier Thermal Cycler. The RNA was mixed with sucrose loading dye and run in TAE buffer at 100V and 4°C in pre-cooled, 4% (w/v) agarose stained with ethidium bromide. Mobility of each single RNA strand, pairwise combinations, and the pRNA 3WJ construct were monitored.

References

1. Turner, D. H.; Mathews, D. H., NNDB: The nearest neighbor parameter database for predicting stability of nucleic acid secondary structure. *Nucleic Acids Research* 2010, 38 (Database issue), D280-D282.
2. Guo, P.; Erickson, S.; Anderson, D., A small viral RNA is required for in vitro packaging of bacteriophage phi 29 DNA. *Science* 1987, 236, 690-694.
3. Gu, X.; Schroeder, S., Different sequences show similar quaternary interaction stabilities in prohead viral RNA self-assembly. *Journal of Biological Chemistry* 2011, 286, 14419-14426.
4. Zhang, H.; Endrizzi, J.; Shu, Y.; Haque, F.; Sauter, C.; Shlyakhtenko, L.; Lyubchenko, Y.; Guo, P.; Chi, Y., Crystal structure of 3WJ core revealing divalent ion-promoted thermostability and assembly of the Phi29 hexameric motor pRNA. *RNA* 2013, 19, 1226-1237.
5. Zhang, X.; Tung, C.-S.; Sowa, G. Z.; Hatmal, M. M.; Haworth, I. S.; Qin, P. Z., Global structure of a three-way junction in a phi29 packaging RNA dimer determined using site-directed spin labeling. *Journal of the American Chemical Society* 2012, 134 (5), 2644-2652.
6. Lescoute, A.; Westhof, E., Topology of three-way junctions in folded RNAs. *RNA* 2006, 12, 83-93.
7. Zhang, C.; Tellinghuisen, T.; Guo, P., Use of circular permutation to assess six bulges and four loops of DNA-packaging pRNA of bacteriophage phi29. *RNA* 1997, 3, 315-323.
8. Ding, F.; Lu, C.; Zhao, W.; Rajashankar, K.; Anderson, D.; Jardine, P.; Grimes, S.; Ke, A., Structure and assembly of the essential RNA ring component of a viral DNA packaging motor. *Proceedings of the National Academy of Sciences* 2011, 108, 7357-7362.
9. Hoepflich, S.; Guo, P., Computer modeling of three-dimensional structure of DNA-packaging RNA (pRNA) monomer, dimer, and hexamer of Phi29 DNA packaging motor. *Journal of Biological Chemistry* 2002, 277, 20794-20803.

10. Hill, A. C.; Bartley, L. E.; Schroeder, S. J., Prohead RNA: A noncoding viral RNA of novel structure and function. *Wiley Interdisciplinary Reviews RNA* 2016, 7 (4), 428-37.
11. Hao, Y.; Kieft, J. S., Diverse self-association properties within a family of phage packaging RNAs. *RNA* 2014, 20, 1-16.
12. Hill, A. C.; Schroeder, S. J., Thermodynamic stabilities of three-way junction nanomotifs in prohead RNA. *RNA* 2017.
13. Guo, S.; Tschammer, N.; Mohammed, S.; Guo, P., Specific delivery of therapeutic RNAs to cancer cells via the dimerization mechanism of phi29 motor pRNA. *Human Gene Therapy* 2005, 16, 1097-1109.
14. Li, L.; Liu, J.; Diao, Z.; Shu, D.; Guo, P.; Shen, G., Evaluation of specific delivery of chimeric phi29 pRNA/siRNA nanoparticles to multiple tumor cells. *Molecular BioSystems* 2009, 5, 1361-1368.
15. Tarapore, P.; Shu, Y.; Guo, P.; Ho, S. M., Application of phi29 motor pRNA for targeted therapeutic delivery of siRNA silencing metallothionein-IIA and survivin in ovarian cancers. *Molecular Therapy* 2011, 19, 386-394.
16. Shu, Y.; Cinier, M.; Shu, D.; Guo, P., Assembly of multifunctional phi29 pRNA nanoparticles for specific delivery of siRNA and other therapeutics to targeted cells. *Methods* 2011, 54 (2), 204-214.
17. Haque, F.; Shu, D.; Shu, Y.; Shlyakhtenko, L.; Rychahou, P.; Evers, B.; Guo, P., Ultrastable synergistic tetravalent RNA nanoparticles for targeting to cancers. *Nano Today* 2012, 7 (4), 245-257.
18. Shu, D.; Moll, W. D.; Deng, Z.; Mao, C.; Guo, P., Bottom-up assembly of RNA arrays and superstructures as potential parts in nanotechnology. *Nano Letters* 2004, 4 (9), 1717-1723.
19. Guo, P., Bacterial virus phi29 DNA-packaging motor and its potential applications in gene therapy and nanotechnology. *Methods in Molecular Biology* 2005, 300, 285-324.

20. Guo, S.; Huang, F.; Guo, P., Construction of folate-conjugated pRNA of bacteriophage phi29 DNA packaging motor for delivery of chimeric siRNA to nasopharyngeal carcinoma cells. *Gene Therapy* 2006, 13, 814-820.
21. Chen, C.; Sheng, S.; Shao, Z.; Guo, P., A dimer as a building block in assembling RNA. *Journal of Biological Chemistry* 2000, 275, 17510-17516.
22. Shu, Y.; Haque, F.; Shu, D.; Li, W.; Zhu, Z.; Kotb, M.; Lyubchenko, Y.; Guo, P., Fabrication of 14 different RNA nanoparticles for specific tumor targeting without accumulation in normal organs. *RNA* 2013, 19 (6), 767-777.
23. Khisamutdinov, E. F.; Jasinski, D. L.; Guo, P., RNA as a boiling-resistant anionic polymer material to build robust structures with defined shape and stoichiometry. *ACS Nano* 2014, 8, 4771-4781.
24. Li, H.; Lee, T.; Dziubla, T.; Pi, F.; Guo, S.; Xu, J.; Li, C.; Haque, F.; Liang, X.-J.; Guo, P., RNA as a stable polymer to build controllable and defined nanostructures for material and biomedical applications. *Nano Today* 2015, 10 (5), 631-655.
25. Shu, D.; Shu, Y.; Haque, F.; Abdelmawla, S.; Guo, P., Thermodynamically stable RNA three-way junction for constructing multifunctional nanoparticles for delivery of therapeutics. *Nature Nanotechnology* 2011, 6, 658-667.
26. Li, H.; Rychahou, P. G.; Cui, Z.; Pi, F.; Evers, B. M.; Shu, D.; Guo, P.; Luo, W., RNA nanoparticles derived from three-way junction of phi29 motor pRNA are resistant to I-125 and Cs-131 radiation. *Nucleic Acid Therapeutics* 2015, 25 (4), 188-97.
27. Diamond, J. M.; Turner, D. H.; Mathews, D. H., Thermodynamics of three-way multibranch loops in RNA. *Biochemistry* 2001, 40 (23), 6971-81.
28. Liu, B.; Diamond, J. M.; Mathews, D. H.; Turner, D. H., Fluorescence competition and optical melting measurements of RNA three-way multibranch loops provide a revised model for thermodynamic parameters. *Biochemistry* 2011, 50 (5), 640-653.
29. Bailey, S.; Wichitwechkarn, J.; Johnson, D.; Reilly, B.; Anderson, D.; Bodley, J., Phylogenetic analysis and secondary structure of the *Bacillus subtilis* bacteriophage RNA required for DNA packaging. *Journal of Biological Chemistry* 1990, 265, 22365-22370.

30. Schroeder, S. J.; Turner, D. H., Factors affecting the thermodynamic stability of small asymmetric internal loops in RNA. *Biochemistry* 2000, 39 (31), 9257-74.
31. Xia, T.; SantaLucia, J., Jr.; Burkard, M. E.; Kierzek, R.; Schroeder, S. J.; Jiao, X.; Cox, C.; Turner, D. H., Thermodynamic parameters for an expanded nearest-neighbor model for formation of RNA duplexes with Watson-Crick base pairs. *Biochemistry* 1998, 37 (42), 14719-35.
32. McDowell, J. A.; Turner, D. H., Investigation of the structural basis for thermodynamic stabilities of tandem GU mismatches: solution structure of (rGAGGUCUC)₂ by two-dimensional NMR and simulated annealing. *Biochemistry* 1996, 35 (45), 14077-89.
33. Zhao, W.; Saha, M.; Ke, A.; Morais, M.; Jardine, P.; Grimes, S., A three-helix junction is the interface between two functional domains of prohead RNA in phi29 DNA packaging. *Journal of Virology* 2012, 86, 11625-11632.
34. Mathews, D. H.; Disney, M. D.; Childs, J. L.; Schroeder, S. J.; Zuker, M.; Turner, D. H., Incorporating chemical modification constraints into a dynamic programming algorithm for prediction of RNA secondary structure. *Proceedings of the National Academy of Sciences of the United States of America* 2004, 101 (19), 7287-92.
35. Lorenz, R.; Bernhart, S. H.; Honer zu Siederdissen, C.; Tafer, H.; Flamm, C.; Stadler, P. F.; Hofacker, I. L., Vienna Package 2.0. *Algorithms for Molecular Biology* 2011, 6 (1).
36. Zuker, M., Mfold web server for nucleic acid folding and hybridization prediction. *Nucleic Acids Research* 2003, 31 (13), 3406-15.
37. Andronescu, M.; Aguirre-Hernández, R.; Condon, A.; Hoos, H. H., RNAsoft: a suite of RNA secondary structure prediction and design software tools. *Nucleic Acids Research* 2003, 31 (13), 3416-3422.
38. Hao, Y.; Kieft, J. S., Three-way junction conformation dictates self-association of phage packaging RNAs. *RNA Biology* 2016, 13 (7), 635-45.
39. Westhof, E.; Masquida, B.; Jossinet, F., Predicting and modeling RNA architecture. *Cold Spring Harbor Perspectives in Biology* 2011, 3 (2).

40. Leontis, N. B.; Stombaugh, J.; Westhof, E., The non-Watson–Crick base pairs and their associated isostericity matrices. *Nucleic Acids Research* 2002, 30 (16), 3497-3531.
41. Walter, A. E.; Turner, D. H.; Kim, J.; Lyttle, M. H.; Muller, P.; Mathews, D. H.; Zuker, M., Coaxial stacking of helices enhances binding of oligoribonucleotides and improves predictions of RNA folding. *Proceedings of the National Academy of Sciences of the United States of America* 1994, 91 (20), 9218-9222.
42. Tyagi, R.; Mathews, D. H., Predicting helical coaxial stacking in RNA multibranch loops. *RNA* 2007, 13 (7), 939-951.
43. Kennedy, S. D., NMR methods for characterization of RNA secondary structure. *Methods in Molecular Biology* 2016, 1490, 253-64.
44. Gruber, A. R.; Bernhart, S. H.; Lorenz, R., The ViennaRNA Web Services. In *RNA Bioinformatics*, Picardi, E., Ed. Springer New York: New York, NY, 2015; pp 307-326.
45. Andronescu, M.; Condon, A.; Hoos, H. H.; Mathews, D. H.; Murphy, K. P., Computational approaches for RNA energy parameter estimation. *RNA* 2010, 16 (12), 2304-18.
46. Binzel, D. W.; Khisamutdinov, E. F.; Guo, P., Entropy-driven one-step formation of phi29 pRNA 3WJ from three RNA fragments. *Biochemistry* 2014, 53 (14), 2221-2231.
47. Schroeder, S. J.; Turner, D. H., Optical melting measurements of nucleic acid thermodynamics. *Methods in Enzymology* 2009, 468, 371-387.
48. Marky, L. A.; Breslauer, K. J., Calculating thermodynamic data for transitions of any molecularity from equilibrium melting curves. *Biopolymers* 1987, 26 (9), 1601-1620.
49. Gu, X.; Nguyen, M. T.; Overacre, A.; Seaton, S.; Schroeder, S. J., Effects of salt, polyethylene glycol, and locked nucleic acids on the thermodynamic stabilities of consecutive terminal adenosine mismatches in RNA duplexes. *The Journal of Physical Chemistry B* 2013, 117 (13), 3531-40.

50. Zhukov, A.; Karlsson, R., Statistical aspects of van't Hoff analysis: a simulation study. *Journal of Molecular Recognition* 2007, 20 (5), 379-385.
51. Tellinghuisen, J., Van't Hoff analysis of K° (T): How good...or bad? *Biophysical Chemistry* 2006, 120 (2), 114-120.
52. Bloomfield, V. A.; Crothers, D. M.; Tinoco, I., Jr., Interactions of nucleic acids and water and ions. In *Nucleic Acids Structures, Properties, and Functions*, University Science Books: Sausalito, CA, 2000; pp 475-534.
53. Mathews, D. H.; Turner, D. H., Experimentally derived nearest-neighbor parameters for the stability of RNA three- and four-way multibranch loops. *Biochemistry* 2002, 41 (3), 869-80.

Chapter 4: Phi29-Alternative 3WJs as Viable Candidates in the Development of Nanoparticles for Therapeutic Drug Delivery

Abstract

A three-way junction (3WJ) in viral prohead or packaging RNA (pRNA) is a building block in nanotechnology. The phi29 3WJ sequence is used commonly in proof-of-concept nanotechnology studies, but to date, other sequences remain unexplored. Rich sequence and structural diversity among phylogenetically related 3WJs may contribute to the development of new nanoparticles for therapeutic drug delivery. Recently, we reported that several 3WJs are more thermodynamically stable than the phi29 3WJ, and our results suggested new building blocks in the design of supramolecular structures such as drug delivery vectors. The further development of phi29-alternative 3WJs for clinical use will depend on their abilities to overcome key physiological barriers such as serum nuclease degradation, clearance from circulation, and cell uptake. Here, we present data showing that certain 3WJs are both thermodynamically stable and stable in human blood serum. For example, the thermodynamically stable M2 3WJ is up to 70% more stable in serum than the prototype phi29 3WJ. Preliminary data indicate that 3WJs accumulate in neuroblastoma cells to approximately 20% over 24 hours. Our results support the idea that 3WJs will benefit from functionalization to help achieve specific cell targeting *in vivo*. Our work expands the number of useful sequences in the development of RNA-based drug delivery vectors and provides a foundation for translational research with phi29-alternative 3WJs.

Introduction

Nanotechnology is an important tool in translational research for addressing the challenges associated with therapeutic drug delivery ¹. Significant extracellular and intracellular barriers, including stability and degradation in blood serum, organ uptake and distribution, hepato-renal clearance, immunogenic response, and off-target effects interfere with a drug's ability to reach its site of action and thus hinder efficacy ². Encapsulation within or conjugation to nanoparticles (NP) has led to significant advances in the stability, solubility, and biodistribution of drugs while simultaneously minimizing side effects such as immunogenicity and toxicity ³⁻⁴. An example is Doxil[®], the first FDA-approved nano-drug, which significantly reduces the life-threatening cardiotoxicity associated with the small-molecule chemotherapeutic agent doxorubicin by encapsulation in a liposome ⁵. Additionally, because they can shield drugs from undesirable interactions in biological milieu, NP can help realize the potential of potent but physiologically unstable classes of therapeutics, such as small interfering RNAs (siRNAs) ^{3, 6-7}. Indeed, at the time of this publication, the results of a Phase III clinical trial are expected for what might become the first FDA-approved siRNA drug, patisiran (Alnylam Pharmaceuticals), which is a lipid nanoparticle formulation for the treatment of transthyretin-mediated amyloidosis ⁸.

In recent years, NP comprising ribonucleic acid (RNA) have emerged as highly tunable platforms for therapeutic drug delivery ⁹⁻¹⁰. The advantages of nucleic acids as a NP material include defined base pairing and physicochemical properties that allow for precise control over size, shape, and surface chemistry and modifications that can be tailored to achieve particular functionalities in vivo ¹¹. Additionally, RNA may prove a

particularly useful platform for the delivery of siRNAs, as these molecules can be appended readily to an RNA scaffold core without the need for separate covalent linkages or complex chemistries². A system based on the robust three-way junction (3WJ) motif found naturally in viral prohead or packaging RNA (pRNA) has leveraged these principles for therapeutic drug delivery and has shown some success at the proof-of-concept level¹²⁻²⁷, for example in the delivery of siRNAs to cancer cells²⁸⁻³⁰. To date, only the prototype phi29 sequence has been evaluated for use in nanotechnology, while phylogenetically related 3WJs that share a conserved secondary structure but display rich sequence diversity are comparatively underexplored³¹⁻³². Recent studies have suggested that certain phi29-alternative sequences may be more useful as building blocks in nanotechnology³¹⁻³³, and our recent results showed that several 3WJs are more thermodynamically stable than the phi29 3WJ³⁴. The ability of 3WJs to stay intact and reach their intended targets under physiological conditions will be important for applications in vivo. The further development of phi29-alternative 3WJs as NP for therapeutic drug delivery therefore will hinge on their abilities to overcome key barriers, including degradation by blood serum nucleases and cell uptake.

Here, we report the stabilities of 3WJs in human blood serum, and we provide preliminary data for cellular uptake in neuroblastoma cells. Although energetic and physiologic stabilities are not always correlated, our results indicate that the SF5, SF5ΔG69, and M2 3WJs are both thermodynamically stable and stable in serum. In fact, the M2 3WJ is up to 70% more stable in serum than the prototype phi29 3WJ. Additional data show that the intracellular accumulation of these junctions reaches approximately 20% over 24 hours in neuroblastoma cells, suggesting that 3WJs will

benefit from functionalization to achieve active, specific cell targeting. Our work grows the number of viable sequences for use as stable building blocks in RNA nanotechnology and sets a foundation for translational research with certain phi29-alternative 3WJs.

Results

Stabilities of 3WJs in Human Blood Serum

Previously, we reported that certain 3WJs are more thermodynamically stable than the prototype phi29 3WJ used commonly as a building block in RNA nanotechnology³⁴. We measured stability in 1% (v/v) human blood serum and found that certain 3WJs are both more thermodynamically stable and more stable in serum than the phi29 3WJ (Figure 1). Figure 1 reports serum stabilities and melting temperatures (T_{ms}) for the phi29, phi29 Δ U29/ Δ U72-73, phi29 Δ U29/ Δ U72-73-74, GA1, SF5, SF5 Δ G31, SF5 Δ G69, SF5 Δ G31/ Δ G69, and M2 3WJs previously shown to be energetically stable³⁴. Although energetic and physiologic stabilities are not always correlated (Spearman's rank order correlation coefficient, $r_s = 0.49$), on average, the SF5, SF5 Δ G69, and M2 3WJs were more intact than the phi29 3WJ following a 10-minute incubation in serum (Figure 1A), suggesting that these junctions are both energetically and physiologically stable.

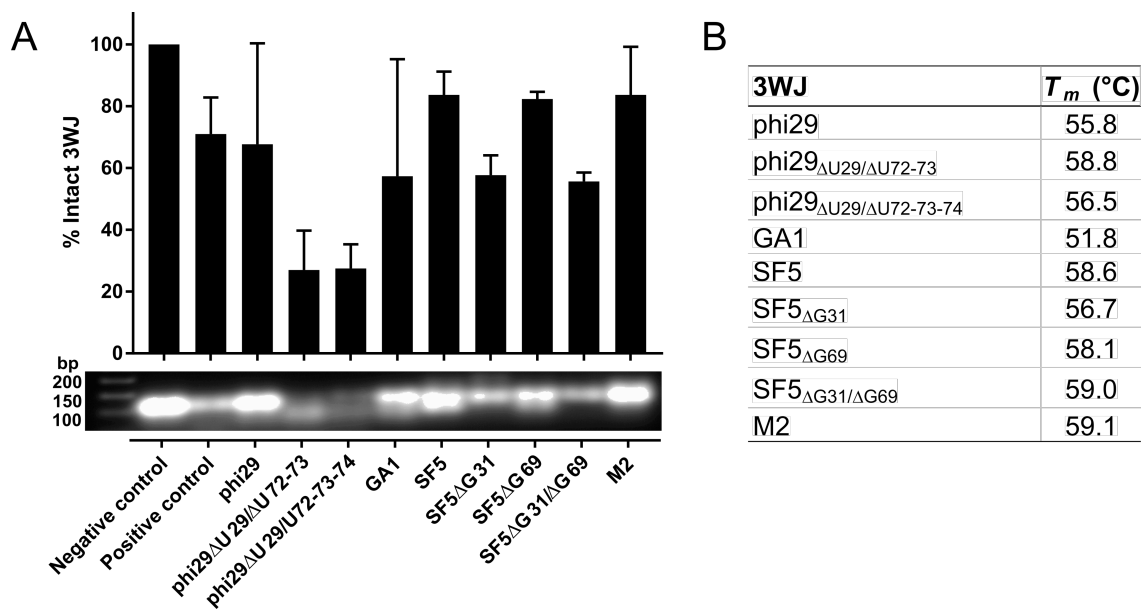


Figure 1 Serum stabilities of 3WJs. (A) Percent intact 3WJ following a 10-minute incubation in 1% (v/v) human blood serum. Results represent means \pm standard deviations ($n = 3$). A gel image from a representative trial shows intact 3WJs following incubation in serum. A negative degradation control, 3WJ incubated in standard melt buffer, and a positive degradation control with added RNase T1, are shown for reference. (B) Melting temperatures (T_m s) for 3WJs at 40 μ M in standard melt buffer (1 M NaCl, 10 mM sodium cacodylate, 0.5 mM EDTA, pH 7.0). The error in T_m is estimated to be ± 1.0 $^{\circ}$ C.

Figure 2 compares the time-resolved serum stabilities of the phi29 and M2 3WJs. The M2 3WJ previously was shown to be most thermodynamically stable among all investigated 3WJs, and it also most consistently outperformed the phi29 3WJ in short serum stability trials. After 10 minutes in 1% (v/v) human blood serum, the M2 3WJ was largely intact, whereas the majority of the phi29 3WJ was degraded (Figure 2). For time points after 10 minutes, the phi29 3WJ was no longer detectable, whereas the M2 3WJ was degraded but detectable at 1 hour, the longest time tested (Figure 2). Thus, the M2 3WJ both is more stable at short time points and is more stable over time than the phi29 3WJ.

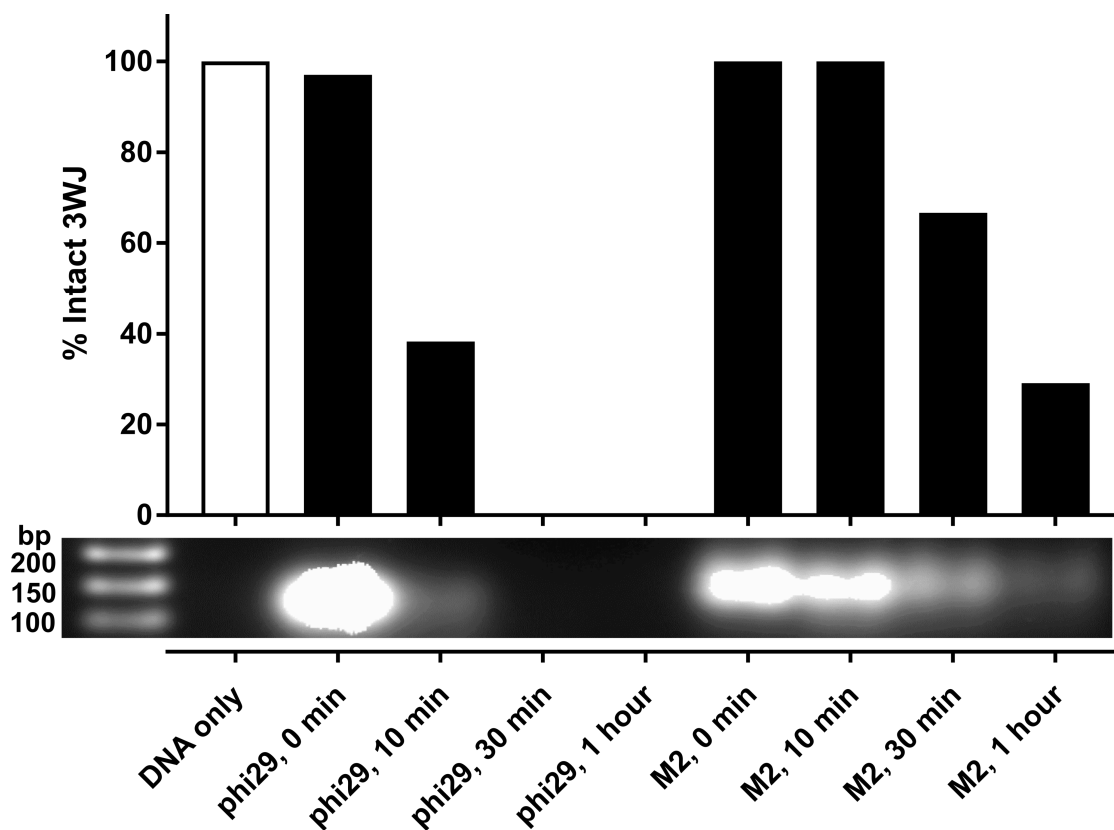


Figure 2 Time-resolved serum stabilities of the phi29 3WJ and M2 3WJs. Percent intact 3WJ normalized to an internal nucleic acid recovery control (DNA only, hollow bar) is shown for each 3WJ following incubation in 1% (v/v) human blood serum for the times indicated. The nucleic acid recovery control runs with lower mobility on a gel and therefore is not depicted in the gel image. Bands that measured over 100% relative intensity are shown as 100%.

Uptake of 3WJs in Neuroblastoma Cells

To assess how well 3WJs enter and accumulate in cells without an active targeting mechanism, we measured uptake in neuroblastoma cells. We chose to investigate the prototype phi29 3WJ and the SF5, SF5ΔG69, and M2 3WJs because these 3WJs are both the most thermodynamically stable and consistently the most stable in human blood serum among the investigated 3WJs (Figure 1). 80-90% confluent neuroblastoma cells were incubated with radiolabeled 3WJs in serum-free media, and at the times indicated, extracellular and intracellular radioactivity were measured (Figure 3). It is

known that in serum-free media, cell division is impaired, differentiation is promoted³⁵⁻³⁶, stress responses are activated, and there is a marked decrease in cell viability after only 24-48 hours³⁷⁻³⁸. We monitored uptake over 24 hours, and cells remained intact over this period. After 24 hours, the phi29 3WJ accumulated to 16%, the M2 3WJ accumulated to 14%, the SF5 3WJ accumulated to 20%, and the SF5ΔG69 3WJ accumulated to 14% in the intracellular compartment (Figure 3). By contrast, a radiolabeled single-stranded RNA showed statistically significantly higher accumulation in cells (Figure 4).

Discussion

Stabilities of 3WJs in Human Blood Serum

RNA is a promising platform in the development of NP for therapeutic drug delivery¹⁰; however, nucleases in blood serum represent an initial and significant barrier to systemically administered RNA-based NP, which may not have sufficient time to reach an intracellular target before being degraded². Certain chemical modifications to the RNA backbone (*e.g.*, phosphorothioate linkages) or ribose (*e.g.*, 2'fluoro) can extend the half-life of RNA by increasing its thermodynamic stability and by rendering it less susceptible to enzymatic degradation and intrinsic chemical degradation³⁹⁻⁴¹. However, modifications can show toxicity *in vivo*⁶, and RNA sequences with inherently higher energetic and physiologic stabilities may reduce dependence on chemical stabilization.

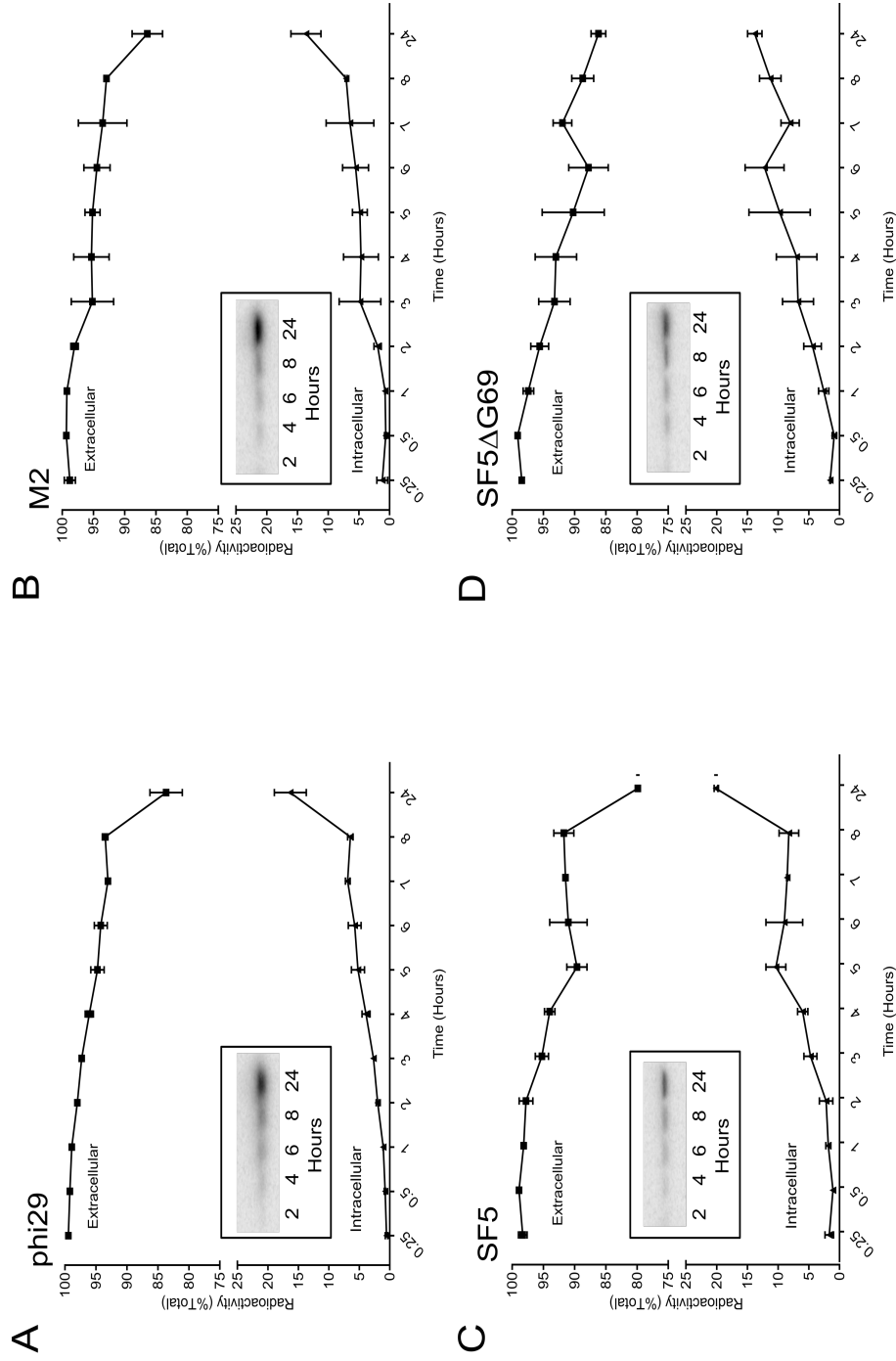


Figure 3 Uptake of radiolabeled (A) phi29, (B) M2, (C) SF5, and (D) SF5ΔG69 3WJs in neuroblastoma cells. Extracellular and intracellular radioactivity are plotted over the period 24 hours. Results represent means ± standard deviations from two independent experiments. Inset: Polyacrylamide gel electrophoresis of RNA recovered from the total cellular extract shows accumulation in the intracellular compartment over the period 2 to 24 hours.

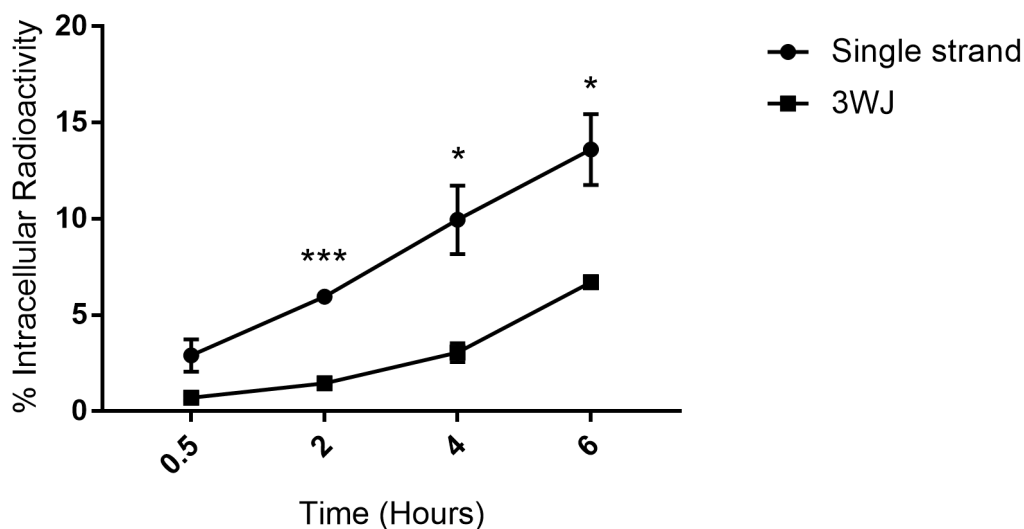


Figure 4 Uptake of radiolabeled single-stranded RNA and 3WJ in neuroblastoma cells. Intracellular radioactivity is plotted over the period 6 hours. Results represent means \pm standard deviations from two independent experiments. * $P \leq 0.001$, * $P \leq 0.05$. At 0.5 hours, $P = 0.07$.**

It has been reported previously that an unmodified phi29 3WJ is stable in 10% (v/v) fetal bovine serum (FBS) for up to two hours¹⁴. Other studies have reported that the unmodified phi29 3WJ is completely degraded after incubation in 10% (v/v) FBS for 15 minutes²³ and 10 minutes¹². The variability in these results may be explained by variability among batches of serum, in particular, with respect to the activity of serum nucleases. While our own examination of 3WJ stability in serum also indicated some trial-to-trial variability (Figure 1), we were able to show that the SF5, SF5ΔG69, and M2 3WJs consistently are more stable in human blood serum than the phi29 3WJ.

Different RNA sequences have different serum stabilities⁴². Recent studies on siRNA digestion in serum have identified endoribonuclease blunt cut sites UA/UA and CA/UG⁴² and a staggered cut site GUX/XAU⁴³. Table 1 summarizes the number of times each cut site occurs in each 3WJ investigated in this study. Contrary to

expectation, the most serum stable M2 3WJ also contains the highest number of each cut site and the highest total number of cut sites among all investigated 3WJs. Although endoribonucleases can bind short duplex RNAs approximately the length of one 3WJ helix⁴⁴, cut sites in helices emerging from a 3WJ may be less accessible to enzymes relative to cut sites in an siRNA due to inherent secondary and tertiary structure⁴⁵. These results may suggest the presence of other cut sites in serum-sensitive 3WJs, or it may suggest that another factor, such as 3WJ shape, plays a role in serum stability.

Table 1 Number of blunt endoribonuclease cut sites UA/UA, CA/UG⁴² and staggered endoribonuclease cut sites GUX/XAU⁴³ in 3WJ sequences, where X represents any nucleotide A, U, C, or G.

	UA/UA	CA/UG	GUX/XAU
Phi29	1	4	0
Phi29 _{ΔU29/ΔU72-73}	1	4	0
Phi29 _{ΔU29/ΔU72-73-74}	1	4	0
GA1	3	2	0
SF5	1	3	0
SF5 _{ΔG31}	1	3	0
SF5 _{ΔG69}	1	3	0
SF5 _{ΔG31/ΔG69}	1	3	0
M2	3	4	1

Serum Stabilities in Relation to Metal Ion Binding and Structure

One hypothesis is that stability gains by metal ion binding may help explain why certain 3WJs are more stable in serum. Our previous results indicated that the phi29, SF5, and M2 3WJs are stabilized in the presence of Mg²⁺³⁴. The concentration of Mg²⁺

in the blood serum of healthy human adults is estimated at 0.55 – 0.75 mM⁴⁶, and prior studies have shown that the stabilizing effect of this ion on the 3WJ is most pronounced at physiological temperature³³. Our previously reported thermodynamic data showed that the addition of 10 mM Mg²⁺ stabilizes the phi29 3WJ by approximately 1.5 kcal mol⁻¹ at 37°C, whereas 10 mM Mg²⁺ stabilizes the SF5 3WJ by approximately 12.6 kcal mol⁻¹ and the M2 3WJ by approximately 18.3 kcal mol⁻¹ at 37°C. Based on these data, it is possible that the Mg²⁺ present in human blood serum has a greater stabilizing effect on the SF5 and M2 3WJs relative to the phi29 3WJ, and this may partially explain the superior stabilities of the SF5 and M2 3WJs in this context.

Another hypothesis is that 3WJ structure confers nuclease stability on certain sequences. This idea perhaps is best exemplified by the structure of a subgenomic flaviviral RNA, which includes an RNA 3WJ and a pseudoknot that confound nuclease activity⁴⁷. Structure at the 3WJ can be difficult to predict, and it becomes increasingly difficult for larger junctions with unpaired nucleotides^{34, 48}. However, our data indicate a positive correlation between the predicted number of unpaired nucleotides at the 3WJ and the stability of the 3WJ in serum (Spearman's rank order correlation coefficient, $r_s = 0.87$). More data will be necessary to further explore the role of conformation in 3WJ energetic and physiologic stabilities. It is possible that both metal ion binding and conformation play a role in 3WJ serum stability.

Cellular Uptake of 3WJs

In most cases, NP that are able to overcome extracellular barriers still must be taken up by cells in order to achieve their desired effects. It has been suggested that the cell membrane is a barrier to the passive diffusion of RNA molecules⁴⁹⁻⁵⁰. However, certain

cells take up double-stranded RNA (dsRNA) via pattern recognition receptor-mediated endocytosis. In particular, scavenger receptors mediate the uptake of dsRNA⁵¹⁻⁵³. For example, when RNA interference is used to target scavenger receptor class C, type I (*i.e.*, *SR-CI*) in *Drosophila* S2 cells, the uptake of dsRNA is significantly decreased; conversely, when Chinese hamster ovary (CHO) cells are stably transfected with *SR-CI*, uptake of dsRNA is enhanced⁵¹. Furthermore, active, specific cell targeting can be achieved with functionalization, such as with aptamers that trigger receptor-mediated endocytosis¹⁰.

We observed 3WJ stability and accumulation in neuroblastoma cells to approximately 20% over 24 hours (Figure 3). An appropriate time scale for gene silencing by siRNA reflects cell doubling time and RNA half-life⁵⁴. Specifically, gene silencing in cells with a doubling time that is shorter than the half-life of an siRNA will be limited by dilution due to cell division, whereas gene silencing in cells with a doubling time that is longer than the half-life of an siRNA will be limited by the intracellular persistence of the siRNA⁵⁴. The doubling time of NG108-15 neuroblastoma cells is 22 hours⁵⁵. In these cells, a 3WJ NP carrying an siRNA should stay intact for 22 hours, and stability gains beyond this would have only an insignificant effect on the duration of gene silencing⁵⁴.

The phi29 3WJ, in particular, showed 16% intracellular accumulation over 24 hours (Figure 3). Previous studies have reported the binding and internalization of a phi29 3WJ to MDA-MB-231 human breast cancer cells at 16.3% after two hours²². Another study reported association of a phi29 3WJ with U87EGFRvIII glioblastoma cells at 40.3% after two hours²⁸. In both cases, functionalization of the phi29 3WJ with

an aptamer increased cell association to approximately 70%^{22, 28}. Yet another study in LNCaP-FGC and PC-3 human prostate cancer cells showed that after two hours, a non-functionalized phi29 3WJ binds at levels of 6.6% and 4.4%, respectively, and functionalization with an aptamer increased cell binding up to 91.2%²³. It is known that different cell lines have different propensities for taking up extracellular material including RNA⁵⁶⁻⁵⁷, but cell types that show minimal uptake of naked RNA may show greater-than-marginal gains in uptake with RNA functionalization.

Cellular Uptake Over Time

Although after 24 hours the total amounts of intracellular 3WJ were similar for all four constructs, data over the first eight hours may suggest differences in the uptake rates for different 3WJs. The phi29 3WJ appeared to be taken up steadily, at a rate of approximately 1% per hour over the first seven hours. The error in the measured intracellular radioactivity for cells incubated with the M2 3WJ was larger than the error for cells incubated with the phi29 3WJ during this period, and the trends in cellular uptake for these junctions may be similar.

By contrast, the SF5 and SF5ΔG69 3WJs may accumulate faster than the phi29 and M2 3WJs. The SF5 3WJ reached an intracellular accumulation of $10.4 \pm 1.6\%$, a local peak, at hour five. Similarly, the SF5ΔG69 3WJ reached an intracellular accumulation of $12.2 \pm 3.2\%$, a local peak, at hour six. By comparison, neither the phi29 nor the M2 3WJ accumulated to above 7% prior to the 24-hour mark. An analysis of variance (ANOVA) on these values showed that the total amount of intracellular SF5 3WJ was statistically significantly different from the amounts of phi29 and M2 3WJs at hour five ($F(2,3) = 10.94$, $p = 0.041870$). A post hoc Tukey test showed that at this

time, intracellular levels of the phi29 and SF5 3WJs differed significantly ($p < .05$), and intracellular levels of the M2 and SF5 3WJs differed significantly ($p < .05$), while the phi29 and M2 3WJ levels were not significantly different from one another. ANOVA on values at hour six did not reveal statistical significance ($F(2,3) = 5.54$, $p = 0.098351$).

While the physical size, chemical structure, and gel mobility of each 3WJ is approximately the same ³⁴, it is known that different 3WJs adopt different conformations *in vitro*, and it is possible that conformation affects cellular uptake. Predictions using Junction Explorer ⁵⁸, an algorithm that bins 3WJ sequences into one of three topological families A, B, or C ⁵⁹ based on predicted secondary structure, suggest that both the SF5 and SF5 Δ G69 3WJs adopt a conformation consistent with family A that is different from both phi29 and M2 (Figure 5). (Predictions for all 3WJs can be found in Appendix II Table 3.) Additional studies will be needed to further address a possible link between conformation and cell uptake, but knowledge that the ability of 3WJs to be taken up by cells may be modulated by 3WJ shape could have implications for RNA nanotechnology, especially in the development of rationally designed drug delivery vectors.

3WJ	Family	Stacking Helices
Phi29	C	A/D
M2	B	A/CE
SF5	A	CE/D
SF5 Δ G69	A	CE/D

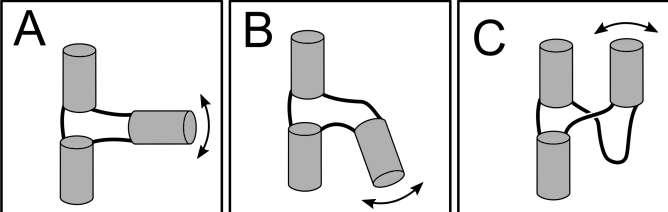


Figure 5 consists of two parts. Part (A) is a table with three columns: '3WJ', 'Family', and 'Stacking Helices'. It lists four 3WJ sequences: Phi29 (Family C, Stacking Helices A/D), M2 (Family B, Stacking Helices A/CE), SF5 (Family A, Stacking Helices CE/D), and SF5 Δ G69 (Family A, Stacking Helices CE/D). Part (B) shows three cartoon diagrams labeled A, B, and C, each depicting a different three-way junction topology. Diagram A shows a central helix with two other helices branching off at different angles. Diagram B shows a similar structure but with a different branching pattern. Diagram C shows a more complex branching structure with helices stacked on top of each other.

Figure 5 (A) Predicted family and helical coaxial stacking interactions for the phi29, M2, SF5, and SF5 Δ G69 3WJs using Junction Explorer. (B) Cartoon representations for the three families A, B, and C depicting different three-way junction topologies.

Other Factors Affecting Cell Uptake

Other factors, such as cell confluency and NP size, can affect cell uptake. Indeed, the uptake of NP in confluent cells can be 2.5-fold lower than in actively growing cells⁵⁶, and in our own studies we observed a significant reduction in 3WJ uptake with cells at 100% confluence (data not shown). Additionally, the size of NP affects cellular uptake and warrants special consideration for applications *in vivo*. Studies monitoring the uptake of microspheres of defined sizes in six different cell lines showed that submicron particles are taken up by most cell types tested, while uptake of 1010 nm particles is significantly lower and dependent upon cell type⁵⁶. Another recent study using titanium dioxide (TiO₂) and silver (Ag) NP reported size-dependent uptake in neuroblastoma cells, with smaller NP able to penetrate and accumulate in cells more efficiently⁶⁰. Our own data comparing the uptake of single-stranded RNA and the 3WJ supports this idea (Figure 4). *In vivo*, size is important not only for cell uptake but also for avoiding clearance by the mononuclear phagocyte system (MPS), formerly reticuloendothelial system (RES), which is promoted with very small and very large NP². In particular, NP smaller than 8 nm are readily filtered by the kidneys⁶¹. The 3WJs investigated here measure 5-8 nm in diameter (Appendix II Table 1), a size that may support uptake by the majority of cell types but may be subject to rapid clearance *in vivo*⁶¹⁻⁶².

Future Prospects for Improving Cell Uptake and Specificity

As previously discussed, uptake of a phi29 3WJ could be increased from 6.6% to over 91% following functionalization with an aptamer²³. Relative to natural receptor ligands such as hyaluronic acid (HA)⁶³ and folate⁶⁴, RNA aptamers, in particular, are an appealing option for achieving active, specific cell targeting because an RNA aptamer

sequence can be appended directly to the 3WJ scaffold core without the need for complex chemistries². Many factors may be considered in choosing a targeting molecule for homing 3WJs to specific cells, but the tunability of the RNA platform may prove very useful for functionalizing 3WJs to promote cell uptake.

Conclusion

Certain phi29-alternative 3WJs are viable building blocks in the development of NP for therapeutic drug delivery. Relative to the prototype phi29 3WJ, our data show that the SF5, SF5ΔG69, and M2 3WJs are more thermodynamically stable and more stable in human blood serum, suggesting that these junctions will have superior stability *in vivo*. Additionally, preliminary data indicate that these 3WJs enter and accumulate to similar levels over 24 hours in neuroblastoma cells. The results of our studies can be used as a springboard for continued research on phi29-alternative 3WJs in nanotechnology, especially in the development of NP that persist in biological milieu. Our work provides further support for increasing the sequence diversity in pRNA-based nanotechnology and sets a solid foundation for translational research with certain phi29-alternative 3WJs.

Materials and Methods

Serum Stability Assays

The pRNA 3WJ can be assembled from three strands 3WJa, 3WJb, and 3WJc mixed in equimolar concentrations¹². Tripartite 3WJs designed as described previously³⁴ were assembled at 10 μM in RNase-free water, dried, and resuspended in either standard melt buffer (1M NaCl, 10 mM sodium cacodylate, 0.5 mM EDTA, pH 7.0) or 100-fold diluted human blood serum (Oklahoma Blood Institute) and incubated at

physiological temperature (*i.e.*, 37°C) for 10 minutes unless otherwise indicated. A negative degradation control, phi29 3WJ in standard melt buffer, was used as a reference. A positive degradation control with 5 units added RNase T1 also was used as a reference. After incubation in either standard melt buffer or serum, RNA was recovered via phenol extraction and ethanol precipitation. Reactions were mixed with one volume phenol:chloroform:isoamyl alcohol (25:24:1), gently shaken by hand, and centrifuged for 5 minutes at 16,000 x g and room temperature. The aqueous phase was transferred to a clean centrifuge tube, and this extraction procedure was repeated twice. For ethanol precipitation of RNA, 0.10 volume of 3 M sodium acetate, pH 5.0 followed by 2.5 volumes of ice cold ethanol was added to each reaction and incubated at -80°C for 1 hour and -20°C overnight. Reactions were centrifuged for 30 minutes at 16,000 x g and 4°C, and supernatants were removed and discarded. RNA pellets were washed with 150 µL ice cold 70% (v/v) ethanol and centrifuged for 2 minutes at 16,000 x g and 4°C. After the ethanol was removed, the RNA was dried for 5-10 minutes, resuspended in standard melt buffer, and run in TAE buffer at 50 V and 4°C in pre-cooled, 2% (w/v) agarose stained with ethidium bromide. For time-resolved serum stabilities of 3WJs, an internal control for nucleic acid recovery, *i.e.*, 0.5 µL plasmid DNA at 1 µg/µL, was added to each reaction prior to phenol extraction and ethanol precipitation. Gel imaging was performed on a ChemiDoc XRS+ Imaging System (BIO-RAD). Intensities for each 3WJ band were calculated relative to a negative degradation control using ImageQuant software (GE Healthcare Life Sciences).

Cellular Uptake Assays

The methods for RNA uptake and stability in cells have been described previously⁶⁵ and were used with slight modifications. Briefly, NG108-15 neuroblastoma x glioma hybrid cells were grown in high glucose Dulbecco's modified Eagle's medium (DMEM) supplemented with 10% fetal bovine serum, L-glutamine, pyridoxine hydrochloride, sodium bicarbonate (3.7 g/L), sodium hypoxanthine (100 μ M), aminopterin (0.4 μ M), and thymidine (16 μ M) at 37°C in a 5% CO₂/95% humidified air atmosphere. Cells at 80-90% confluence were washed free of serum and fed with growth medium in the absence of serum during incubation with RNA at 37°C for the times indicated. Strand 3WJa (1 μ g) for each of the 3WJs designed as described previously³⁴ was 5'-labeled with 50 μ Ci of [γ -³²P]ATP (3000 Ci/mmol; PerkinElmer) in a total volume of 20 μ L containing T4 polynucleotide kinase (New England BioLabs). Unincorporated mononucleotides were removed using Microcon centrifugal filter units with YM-3 membranes (Sigma-Aldrich). Labeled 3WJa and unlabeled 3WJa, 3WJb, and 3WJc were assembled at room temperature and added to cells in serum-free media in 24-well plates for a final concentration of 250 nM 3WJ and 1x10⁵ dpm per well for the times indicated. Strand 3WJa (1 μ g) for each of the 3WJs designed as described previously³⁴ was 5'-labeled with 50 μ Ci of [γ -³²P]ATP (3000 Ci/mmol; PerkinElmer) in a total volume of 20 μ L containing T4 polynucleotide kinase (New England BioLabs). Unincorporated mononucleotides were removed using Microcon centrifugal filter units with YM-3 membranes (Sigma-Aldrich). Labeled 3WJa and unlabeled 3WJa, 3WJb, and 3WJc were assembled at room temperature and added to cells in serum-free media in 24-well plates for a final concentration of 250 nM 3WJ and

1×10^5 dpm per well for the times indicated. As a control, labeled 3WJa alone also was added to cells. Cells were incubated at 37°C with the added RNA and at the end of the incubation, the supernatant was removed, and cells were washed with PBS and solubilized with 0.1% sodium dodecyl sulfate (SDS). Aliquots of the supernatant and total cellular extract were used for radioactivity determination by counting in a LS 6500 Multi-Purpose Scintillation Counter (Beckman Coulter). Percent radioactivity in the supernatant and in cells was calculated from total radioactivity measured per well. Some fractions of the total cellular extract were subjected to electrophoresis at 150 V and 4°C for 24 hours in pre-cooled, 20% polyacrylamide.

Statistical Analysis

Experiments for 3WJ uptake in NG108-15 cells were performed in duplicate. Results are expressed as means \pm standard deviations. Statistical differences were evaluated using analysis of variance (ANOVA) and considered significant at $P < 0.05$.

References

1. Singh, R.; Lillard, J. W., Nanoparticle-based targeted drug delivery. *Experimental and Molecular Pathology* 2009, 86 (3), 215-223.
2. Parlea, L.; Puri, A.; Kasprzak, W.; Bindewald, E.; Zakrevsky, P.; Satterwhite, E.; Joseph, K.; Afonin, K. A.; Shapiro, B. A., Cellular delivery of RNA nanoparticles. *ACS Combinatorial Science* 2016, 18 (9), 527-547.
3. Li, Y.; Wang, J.; Wientjes, M. G.; Au, J. L., Delivery of nanomedicines to extracellular and intracellular compartments of a solid tumor. *Advanced Drug Delivery Reviews* 2012, 64 (1), 29-39.
4. Au, J. L. S.; Yeung, B. Z.; Wientjes, M. G.; Lu, Z.; Wientjes, M. G., Delivery of cancer therapeutics to extracellular and intracellular targets: Determinants, barriers, challenges and opportunities. *Advanced Drug Delivery Reviews* 2016, 97, 280-301.
5. Barenholz, Y., Doxil(R)--the first FDA-approved nano-drug: lessons learned. *Journal of Controlled Release* 2012, 160 (2), 117-34.
6. Corey, D. R., Chemical modification: The key to clinical application of RNA interference? *The Journal of Clinical Investigation* 2007, 117 (12), 3615-22.
7. Sita, T. L.; Kouri, F. M.; Hurley, L. A.; Merkel, T. J.; Chalastanis, A.; May, J. L.; Ghelfi, S. T.; Cole, L. E.; Cayton, T. C.; Barnaby, S. N.; Sprangers, A. J.; Savalia, N.; James, C. D.; Lee, A.; Mirkin, C. A.; Stegh, A. H., Dual bioluminescence and near-infrared fluorescence monitoring to evaluate spherical nucleic acid nanoconjugate activity in vivo. *Proceedings of the National Academy of Sciences of the United States of America* 2017, 114 (16), 4129-4134.
8. Garber, K., Worth the RISC? *Nature Biotechnology* 2017, 35 (3), 198-202.
9. Kanasty, R.; Dorkin, J. R.; Vegas, A.; Anderson, D., Delivery materials for siRNA therapeutics. *Nature Materials* 2013, 12 (11), 967-977.
10. Jasinski, D.; Haque, F.; Binzel, D. W.; Guo, P., Advancement of the emerging field of RNA nanotechnology. *ACS Nano* 2017, 11 (2), 1142-1164.

11. Kumar, V.; Palazzolo, S.; Bayda, S.; Corona, G.; Toffoli, G.; Rizzolio, F., DNA nanotechnology for cancer therapy. *Theranostics* 2016, 6 (5), 710-725.
12. Shu, D.; Shu, Y.; Haque, F.; Abdelmawla, S.; Guo, P., Thermodynamically stable RNA three-way junction for constructing multifunctional nanoparticles for delivery of therapeutics. *Nature Nanotechnology* 2011, 6, 658-667.
13. Shu, Y.; Haque, F.; Shu, D.; Li, W.; Zhu, Z.; Kotb, M.; Lyubchenko, Y.; Guo, P., Fabrication of 14 different RNA nanoparticles for specific tumor targeting without accumulation in normal organs. *RNA* 2013, 19 (6), 767-777.
14. Shu, Y.; Shu, D.; Haque, F.; Guo, P., Fabrication of pRNA nanoparticles to deliver therapeutic RNAs and bioactive compounds into tumor cells. *Nature Protocols* 2013, 8 (9), 1635-1659.
15. Shu, D.; Khisamutdinov, E. F.; Zhang, L.; Guo, P., Programmable folding of fusion RNA in vivo and in vitro driven by pRNA 3WJ motif of phi29 DNA packaging motor. *Nucleic Acids Research* 2014, 42 (2), e10.
16. Feng, L.; Li, S. K.; Liu, H.; Liu, C. Y.; LaSance, K.; Haque, F.; Shu, D.; Guo, P., Ocular delivery of pRNA nanoparticles: distribution and clearance after subconjunctival injection. *Pharmaceutical Research* 2014, 31 (4), 1046-58.
17. Khisamutdinov, E. F.; Jasinski, D. L.; Guo, P., RNA as a boiling-resistant anionic polymer material to build robust structures with defined shape and stoichiometry. *ACS Nano* 2014, 8, 4771-4781.
18. Binzel, D. W.; Khisamutdinov, E. F.; Guo, P., Entropy-driven one-step formation of phi29 pRNA 3WJ from three RNA fragments. *Biochemistry* 2014, 53 (14), 2221-2231.
19. Jasinski, D. L.; Khisamutdinov, E. F.; Lyubchenko, Y. L.; Guo, P., Physicochemically tunable polyfunctionalized RNA square architecture with fluorogenic and ribozymatic properties. *ACS Nano* 2014, 8 (8), 7620-7629.
20. Khisamutdinov, E. F.; Li, H.; Jasinski, D. L.; Chen, J.; Fu, J.; Guo, P., Enhancing immunomodulation on innate immunity by shape transition among RNA triangle, square and pentagon nanovehicles. *Nucleic Acids Research* 2014, 42 (15), 9996-10004.

21. Zhang, H.; Pi, F.; Shu, D.; Vieweger, M.; Guo, P., Using RNA nanoparticles with thermostable motifs and fluorogenic modules for real-time detection of RNA folding and turnover in prokaryotic and eukaryotic cells. In *RNA Nanotechnology and Therapeutics: Methods and Protocols*, Guo, P.; Haque, F., Eds. Springer New York: New York, NY, 2015; pp 95-111.
22. Shu, D.; Li, H.; Shu, Y.; Xiong, G.; Carson, W. E.; Haque, F.; Xu, R.; Guo, P., Systemic delivery of anti-miRNA for suppression of triple negative breast cancer utilizing RNA nanotechnology. *ACS Nano* 2015, 9 (10), 9731-9740.
23. Binzel, D. W.; Shu, Y.; Li, H.; Sun, M.; Zhang, Q.; Shu, D.; Guo, B.; Guo, P., Specific delivery of miRNA for high efficient inhibition of prostate cancer by RNA nanotechnology. *Molecular Therapy* 2016, 24 (7), 1267-77.
24. Li, H.; Zhang, K.; Pi, F.; Guo, S.; Shlyakhtenko, L.; Chiu, W.; Shu, D.; Guo, P., Controllable self-assembly of RNA tetrahedrons with precise shape and size for cancer targeting. *Advanced Materials* 2016, 28 (34), 7501-7507.
25. Khisamutdinov, E. F.; Jasinski, D. L.; Li, H.; Zhang, K.; Chiu, W.; Guo, P., Fabrication of RNA 3D nanoprisms for loading and protection of small RNAs and model drugs. *Advanced Materials* 2016, 28 (45), 10079-10087.
26. Pi, F.; Zhang, H.; Li, H.; Thiviyanathan, V.; Gorenstein, D. G.; Sood, A. K.; Guo, P., RNA nanoparticles harboring annexin A2 aptamer can target ovarian cancer for tumor-specific doxorubicin delivery. *Nanomedicine: Nanotechnology, Biology and Medicine* 2017, 13 (3), 1183-1193.
27. Lee, T. J.; Yoo, J. Y.; Shu, D.; Li, H.; Zhang, J.; Yu, J.-G.; Jaime-Ramirez, A. C.; Acunzo, M.; Romano, G.; Cui, R.; Sun, H.-L.; Luo, Z.; Old, M.; Kaur, B.; Guo, P.; Croce, C. M., RNA nanoparticle-based targeted therapy for glioblastoma through inhibition of oncogenic miR-21. *Molecular Therapy* 2017, 25 (7), 1544-1555.
28. Lee, T. J.; Haque, F.; Shu, D.; Yoo, J. Y.; Li, H.; Yokel, R. A.; Horbinski, C.; Kim, T. H.; Kim, S. H.; Kwon, C. H.; Nakano, I.; Kaur, B.; Guo, P.; Croce, C. M., RNA nanoparticle as a vector for targeted siRNA delivery into glioblastoma mouse model. *Oncotarget* 2015, 6 (17), 14766-76.
29. Cui, D.; Zhang, C.; Liu, B.; Shu, Y.; Du, T.; Shu, D.; Wang, K.; Dai, F.; Liu, Y.; Li, C.; Pan, F.; Yang, Y.; Ni, J.; Li, H.; Brand-Saberi, B.; Guo, P., Regression of gastric cancer by systemic injection of RNA nanoparticles carrying both ligand and siRNA. *Scientific Reports* 2015, 5, 10726.

30. Zhang, Y.; Leonard, M.; Shu, Y.; Yang, Y.; Shu, D.; Guo, P.; Zhang, X., Overcoming tamoxifen resistance of human breast cancer by targeted gene silencing using multifunctional pRNA nanoparticles. *ACS Nano* 2017, 11 (1), 335-346.
31. Gu, X.; Schroeder, S., Different sequences show similar quaternary interaction stabilities in prohead viral RNA self-assembly. *Journal of Biological Chemistry* 2011, 286, 14419-14426.
32. Hao, Y.; Kieft, J. S., Diverse self-association properties within a family of phage packaging RNAs. *RNA* 2014, 20, 1-16.
33. Hao, Y.; Kieft, J. S., Three-way junction conformation dictates self-association of phage packaging RNAs. *RNA Biology* 2016, 13 (7), 635-45.
34. Hill, A. C.; Schroeder, S. J., Thermodynamic stabilities of three-way junction nanomotifs in prohead RNA. *RNA* 2017.
35. Krystosek, A., Neurite formation by neuroblastoma-glioma hybrid cells (NG108-15) in defined medium: stochastic initiation with persistence of differentiated functions. *Journal of Cellular Physiology* 1985, 125 (2), 319-29.
36. Seidman, K. J. N.; Barsuk, J. H.; Johnson, R. F.; Weyhenmeyer, J. A., Differentiation of NG108-15 neuroblastoma cells by serum starvation or dimethyl sulfoxide results in marked differences in angiotensin II receptor subtype expression. *Journal of Neurochemistry* 1996, 66 (3), 1011-1018.
37. Li, J.; Lee, Y.; Johansson, H. J.; Mäger, I.; Vader, P.; Nordin, J. Z.; Wiklander, O. P. B.; Lehtiö, J.; Wood, M. J. A.; Andaloussi, S. E. L., Serum-free culture alters the quantity and protein composition of neuroblastoma-derived extracellular vesicles. *Journal of Extracellular Vesicles* 2015, 4, 10.3402/jev.v4.26883.
38. Howard, M. K.; Burke, L. C.; Mailhos, C.; Pizzey, A.; Gilbert, C. S.; Durward Lawson, W.; Collins, M. K. L.; Thomas, N. S. B.; Latchman, D. S., Cell cycle arrest of proliferating neuronal cells by serum deprivation can result in either apoptosis or differentiation. *Journal of Neurochemistry* 1993, 60 (5), 1783-1791.
39. Egli, M.; Pallan, P. S., Crystallographic studies of chemically modified nucleic acids: A backward glance. *Chemistry & Biodiversity* 2010, 7 (1), 60-89.

40. Deleavey, Glen F.; Damha, Masad J., Designing chemically modified oligonucleotides for targeted gene silencing. *Chemistry & Biology* 2012, 19 (8), 937-954.
41. Freier, S. M.; Altmann, K. H., The ups and downs of nucleic acid duplex stability: structure-stability studies on chemically-modified DNA:RNA duplexes. *Nucleic Acids Research* 1997, 25 (22), 4429-4443.
42. Hong, J.; Huang, Y.; Li, J.; Yi, F.; Zheng, J.; Huang, H.; Wei, N.; Shan, Y.; An, M.; Zhang, H.; Ji, J.; Zhang, P.; Xi, Z.; Du, Q.; Liang, Z., Comprehensive analysis of sequence-specific stability of siRNA. *The FASEB Journal* 2010, 24 (12), 4844-4855.
43. Barnaby, S. N.; Lee, A.; Mirkin, C. A., Probing the inherent stability of siRNA immobilized on nanoparticle constructs. *Proceedings of the National Academy of Sciences* 2014, 111 (27), 9739-9744.
44. Nicholson, A. W., Ribonuclease III mechanisms of double-stranded RNA cleavage. *Wiley Interdisciplinary Reviews RNA* 2014, 5 (1), 31-48.
45. Warashina, M.; Kuwabara, T.; Kato, Y.; Sano, M.; Taira, K., RNA-protein hybrid ribozymes that efficiently cleave any mRNA independently of the structure of the target RNA. *Proceedings of the National Academy of Sciences of the United States of America* 2001, 98 (10), 5572-7.
46. Jahnen-Dechent, W.; Ketteler, M., Magnesium basics. *Clinical Kidney Journal* 2012, 5 (Suppl 1), i3-i14.
47. Chapman, E. G.; Costantino, D. A.; Rabe, J. L.; Moon, S. L.; Wilusz, J.; Nix, J. C.; Kieft, J. S., The structural basis of pathogenic subgenomic flavivirus RNA (sfRNA) production. *Science* 2014, 344 (6181), 307.
48. Tyagi, R.; Mathews, D. H., Predicting helical coaxial stacking in RNA multibranch loops. *RNA* 2007, 13 (7), 939-951.
49. Dinger, M. E.; Mercer, T. R.; Mattick, J. S., RNAs as extracellular signaling molecules. *Journal of Molecular Endocrinology* 2008, 40 (4), 151-159.
50. Dowdy, S. F., Overcoming cellular barriers for RNA therapeutics. *Nature Biotechnology* 2017, 35 (3), 222-229.

51. Ulvila, J.; Parikka, M.; Kleino, A.; Sormunen, R.; Ezekowitz, R. A.; Kocks, C.; Ramet, M., Double-stranded RNA is internalized by scavenger receptor-mediated endocytosis in *Drosophila* S2 cells. *The Journal of Biological Chemistry* 2006, 281 (20), 14370-5.
52. Saleh, M.-C.; van Rij, R. P.; Hekele, A.; Gillis, A.; Foley, E.; O'Farrell, P. H.; Andino, R., The endocytic pathway mediates cell entry of dsRNA to induce RNAi silencing. *Nature Cell Biology* 2006, 8 (8), 793-802.
53. Nellimarla, S.; Baid, K.; Loo, Y.-M.; Gale, M.; Bowdish, D. M. E.; Mossman, K. L., Class A scavenger receptor-mediated double-stranded RNA internalization is independent of innate antiviral signaling and does not require phosphatidylinositol 3-kinase activity. *The Journal of Immunology* 2015, 195 (8), 3858.
54. Bartlett, D. W.; Davis, M. E., Insights into the kinetics of siRNA-mediated gene silencing from live-cell and live-animal bioluminescent imaging. *Nucleic Acids Research* 2006, 34 (1), 322-333.
55. Wu, G.; Lu, Z. H.; Xie, X.; Li, L.; Ledeen, R. W., Mutant NG108-15 cells (NG-CR72) deficient in GM1 synthase respond aberrantly to axonogenic stimuli and are vulnerable to calcium-induced apoptosis: they are rescued with LIGA-20. *Journal of Neurochemistry* 2001, 76 (3), 690-702.
56. Zauner, W.; Farrow, N. A.; Haines, A. M., In vitro uptake of polystyrene microspheres: Effect of particle size, cell line and cell density. *Journal of Controlled Release* 2001, 71 (1), 39-51.
57. Diken, M.; Kreiter, S.; Selmi, A.; Britten, C. M.; Huber, C.; Tureci, O.; Sahin, U., Selective uptake of naked vaccine RNA by dendritic cells is driven by macropinocytosis and abrogated upon DC maturation. *Gene Therapy* 2011, 18 (7), 702-708.
58. Laing, C.; Wen, D.; Wang, J. T. L.; Schlick, T., Predicting coaxial helical stacking in RNA junctions. *Nucleic Acids Research* 2012, 40 (2), 487-498.
59. Lescoute, A.; Westhof, E., Topology of three-way junctions in folded RNAs. *RNA* 2006, 12, 83-93.
60. Hsiao, I. L.; Bierkandt, F. S.; Reichardt, P.; Luch, A.; Huang, Y. J.; Jakubowski, N.; Tentschert, J.; Haase, A., Quantification and visualization of cellular uptake of TiO₂

and Ag nanoparticles: comparison of different ICP-MS techniques. *Journal of Nanobiotechnology* 2016, 14 (1), 50.

61. Longmire, M.; Choyke, P. L.; Kobayashi, H., Clearance properties of nano-sized particles and molecules as imaging agents: considerations and caveats. *Nanomedicine (London, England)* 2008, 3 (5), 703-17.

62. Choi, H. S.; Liu, W.; Misra, P.; Tanaka, E.; Zimmer, J. P.; Iyengar, B.; Bawendi, M. G.; Frangioni, J. V., Renal clearance of quantum dots. *Nature Biotechnology* 2007, 25 (10), 1165-70.

63. Badwaik, V.; Liu, L.; Gunasekera, D.; Kulkarni, A.; Thompson, D. H., Mechanistic insight into receptor-mediated delivery of cationic- β -cyclodextrin:hyaluronic acid-adamantamethyl host:guest pDNA nanoparticles to CD44+ cells. *Molecular Pharmaceutics* 2016, 13 (3), 1176-1184.

64. Zwicke, G. L.; Mansoori, G. A.; Jeffery, C. J., Utilizing the folate receptor for active targeting of cancer nanotherapeutics. *Nano Reviews* 2012, 3, 10.3402/nano.v3i0.18496.

65. Standifer, K. M.; Jenab, S.; Su, W.; Chien, C.-C.; Pan, Y.-X.; Inturrisi, C. E.; Pasternak, G. W., Antisense oligodeoxynucleotides to the cloned δ receptor DOR-1: Uptake, stability, and regulation of gene expression. *Journal of Neurochemistry* 1995, 65 (5), 1981-1987.

Chapter 5: Preliminary Investigations of pRNA 3WJ Conformation Using Transmission Electron Microscopy

Abstract

A three-way junction (3WJ) is a critical determinant of structure, stability, and function in viral prohead or packaging RNA (pRNA). The central 3WJ correctly positions peripheral helices A, CE, and D to promote the self-assembly of pRNA in a bacteriophage molecular motor and *in vitro*. Phylogenetically related 3WJs have different energetics and different propensities for self-assembly that may be partially explained by the relative orientation of helices around the junction. Using transmission electron microscopy (TEM) on a helix-extended construct, we directly measured interhelical angles for the prototype phi29 pRNA 3WJ. Our data indicate that the helices emerging from the phi29 3WJ are distributed equally around the junction, with angles of $118 \pm 23^\circ$, $115 \pm 25^\circ$, and $122 \pm 25^\circ$ between helix pairs A and CE, A and D, and CE and D, respectively. These results are consistent with the results of previous studies, which indicate that the phi29 3WJ is a flexible, conformationally dynamic element in pRNA. Our work provides insight into the three-dimensional organization of pRNA, and our technique can be extended to other, phylogenetically related pRNA 3WJ sequences in order to further develop structure-energetics-function relationships and knowledge that will be useful in basic RNA research and RNA nanotechnology.

Introduction

RNA structure comprises a hierarchical assembly of helices formed by Watson-Crick base pairs and motifs maintained by non-Watson-Crick base pairs¹⁻². Multibranch loop motifs such as three-way junctions (3WJs) are ubiquitous in natural RNA

structures and enable the long-range contacts that are essential for many RNA functions, such as gene regulation in riboswitches, auto-catalytic cleavage in hammerhead ribozymes, and protein synthesis in ribosomes^{1, 3}. In folded prohead or packaging RNA (pRNA), a 3WJ is a conserved motif that is critical to the function of a DNA packaging motor found in the phi29-like family of bacteriophages⁴. The central 3WJ positions peripheral helices A, CE, and D such that interlocking loop motifs are able to base pair and form a ring assembly of functional pRNA, which is essential for motor activity⁴⁻⁵. Changes at the 3WJ core that interrupt the native RNA architecture can abolish the self-assembly of pRNA on the viral prohead and impair the packaging activity of the molecular motor⁵. *In vitro*, phylogenetically related pRNAs have different self-assembly behaviors that are modulated by the 3WJ⁶⁻⁷. For example, recent studies have shown that the M2 3WJ preferentially adopts a conformation in solution that favors the formation of thermostable multimers compared to the prototype sequence phi29, which forms only dimers⁸. The self-assembly behavior of certain sequences can be leveraged in RNA engineering to create new structures of diverse sizes, shapes, and functionalities⁹⁻¹¹. Therefore, information about pRNA 3WJ conformation may have important biological and nanotechnological implications⁸.

Recently, we measured the thermodynamic stabilities of various pRNA 3WJs using a system designed for UV optical melting¹². The results of our studies showed that pRNA 3WJs have different energetics. The range of free energies for 3WJs spans over 20 kcal mol⁻¹, and these large differences are not readily explained by sequence or by the number of unpaired nucleotides at the 3WJ core. In the majority of RNA three-way junctions, two of the helices leading into the junction are contiguous and form a

stack, with the third helix positioned adjacent and at an angle to the stack¹. It is known that helical coaxial stacking interactions can be thermodynamically favorable¹³, and one hypothesis is that helical coaxial stacking may help explain differences among the stabilities of different pRNA 3WJs¹². Using a method described previously for the *Tetrahymena* group I ribozyme¹⁴⁻¹⁵, we extended the peripheral helices A, CE, and D of the phi29 pRNA 3WJ to different, resolvable lengths for TEM analysis and directly measured interhelical angles (Figure 1).

Here, we present data showing that the helices emerging from the phi29 3WJ are distributed equally around the junction, with interhelical angles of $118 \pm 23^\circ$, $115 \pm 25^\circ$, and $122 \pm 25^\circ$ between helices A and CE, A and D, and CE and D, respectively ($n = 50$). Our results provide a framework for the investigation of other, related 3WJ sequences in order to fully examine the hypothesis that conformation differs across pRNA 3WJs. This work can be used to further our knowledge of the biophysical properties of pRNA, which can be leveraged in both basic and applied RNA research.

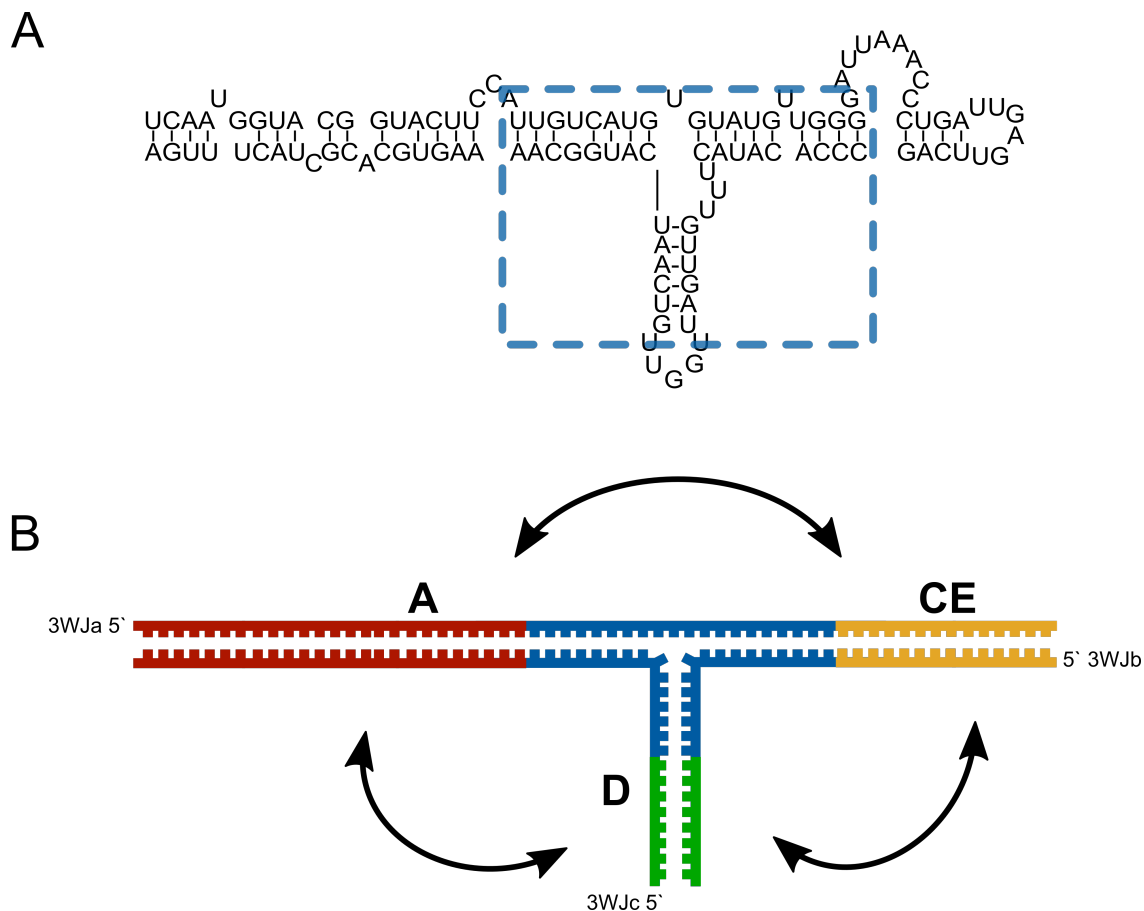


Figure 1 (A) Wild-type phi29 pRNA primary and secondary structure ¹⁶, where boxed nucleotides represent a core phi29 3WJ. (b) Cartoon representation of a tripartite phi29HE_{DNA} 3WJ comprising strands 3WJa, 3WJb, and 3WJc as described previously ¹², where the core 3WJ is in blue. Helices A, CE, and D are shown with extensions to lengths of 100 bp (red), 80 bp (yellow), and 50 bp (green), respectively. Curved arrows indicate interhelical angles.

Results

3WJ Helix-Extended Construct Design and Initial Characterization

Previously, we measured the energetics of various pRNA 3WJs using UV optical melting ¹². For those studies, we designed a tripartite system comprising RNA strands 3WJa, 3WJb, and 3WJc, which anneal to form a 3WJ approximately 5-8 nm in diameter (Appendix II Table 1). In order to visualize and resolve different 3WJ helices using

TEM, we employed a helix-extension method previously described for studies on the *Tetrahymena* group I ribozyme ¹⁴. This method involves artificially lengthening the helices that lead into a natural 3WJ core (Figure 1). For preliminary investigations, we designed a phi29 helix-extended DNA 3WJ construct (phi29HE_{DNA}). We chose the prototype phi29 sequence as a core motif because relative to other sequences, phi29 is well characterized and more biophysical data exist for comparative purposes ^{8, 17-20}.

Helix extension sequences from a prior study ¹⁴ were appended to a previously designed phi29 3WJ (Figure 1). Sequences and secondary structure free energy predictions ²¹ for the phi29HE_{DNA} 3WJ component strands 3WJa, 3WJb, and 3WJc strands are provided in Appendix II Tables 2 and 3, respectively. Secondary structure predictions indicate that formation of the 3WJ is thermodynamically favorable over any interaction within or between strands (Appendix II Table 3). Using dynamic light scattering (DLS), we confirmed the size of the phi29HE_{DNA} 3WJ. Table 1 compares the hydrodynamic diameters of the phi29 and phi29HE_{DNA} 3WJs. Initially, we extended helix A to 100 bp, helix CE to 80 bp, and helix D to 50 bp in order to approximate the relative length proportions found in natural pRNA ¹⁶ (Figure 1). Our rationale was that this design might minimize the potential effect of helix extensions on 3WJ conformation. Previous studies showed no effect of helix extensions on tRNA conformation ¹⁴, and interhelical angles measured using TEM were 90°, consistent with data obtained by X-ray crystallography ²²⁻²⁴. However, to rule out the possibility that the 3WJ conformation observed by TEM is an artifact of the helix extension method, further studies with helix extensions rotated around the phi29 3WJ may be necessary.

Table 1 Diameters of phi29 3WJ and phi29HE_{DNA} as determined by DLS. Results represent means \pm standard deviations.

3WJ	Mean Diameter (nm)
Phi29	7.12 \pm 2.29
Phi29HE _{DNA}	41.90 \pm 25.55

3WJ Conformation Predictions Using Junction Explorer

The topologies of three-way junctions can be classified into one of three families A, B, or C as assigned by Lescoute's and Westhof's analysis of a large number of RNA crystal structures¹. These families consider the relative lengths of single-stranded segments (or unpaired nucleotides) that link adjacent helical elements¹⁻². Using this classification, an algorithm Junction Explorer²⁵ predicts the family and helical coaxial stacking interactions for an input secondary structure. Chapter 4 briefly introduced the helical coaxial stacking interactions for the phi29, SF5, SF5 Δ G69, and M2 3WJs in relation to cell uptake (Chapter 4 Figure 5). The families and helical stacking for all previously described 3WJs and for the phi29HE_{DNA} 3WJ were predicted using Junction Explorer and are reported in Appendix II Table 4. Table 2 compares the family and helical coaxial stacking predictions for the phi29 and phi29HE_{DNA} 3WJs. In some cases, family and helical stacking predictions are sensitive to the order in which the sequences 3WJa, 3WJb, and 3WJc are input into the algorithm. However, both the phi29 and the phi29HE_{DNA} 3WJ consistently are predicted to belong to family C and share helical coaxial stacking of helices A and D.

Table 2 Family and helical coaxial stacking predictions for the phi29 3WJ and phi29HE_{DNA} using Junction Explorer²⁵.

3WJ	Family	Stacking Helices
Phi29	C	A/D
Phi29HE _{DNA}	C	A/D

Electrophoretic Mobility Shift Assay

Assembly of the phi29HE_{DNA} 3WJ from three strands 3WJa, 3WJb, and 3WJc was confirmed using an electrophoretic gel mobility shift assay. Figure 2 depicts the mobility of strands alone, pairwise, and assembled in the 3WJ. Mobility decreases as more components of the three-strand system are added, and a band with low mobility appears only when all three strands are present, indicating formation of the 3WJ from strands 3WJa, 3WJb, and 3WJc.

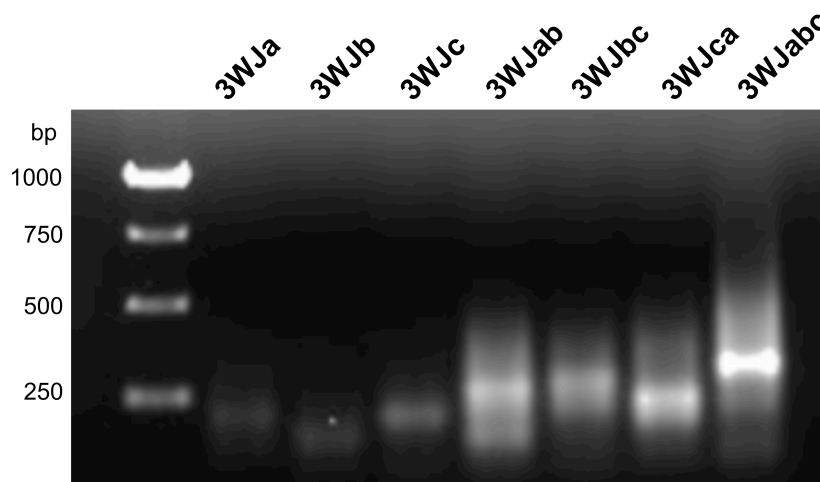


Figure 2 Gel mobility of phi29HE_{DNA} component strands 3WJa, 3WJb, and 3WJc. Single strands, pairwise strands, and strands assembled in the 3WJ are depicted. Strands were mixed at 1.5 μ M in 35 mM Tris-HCl, pH 7.50 and run in TAE buffer in pre-cooled 1% agarose (w/v) at 80V and 4°C.

3WJ Helix Lengths and Interhelical Angles

Figure 3A shows reverse contrast images of the ϕ 29HE_{DNA} 3WJ at 80,000X magnification. The lengths of helices A, CE, and D, and the angles between helix pairs A/CE, A/D, and CE/D in ϕ 29HE_{DNA} are reported in Figures 3B and 3C, respectively. Assuming a rise of 0.34 nm per base pair, the expected lengths for 100 bp, 80 bp, and 50 bp B-form DNA helices are 34 nm, 27.2 nm, and 17 nm, respectively. Consistent with these expectations, the measured lengths of peripheral helices A, CE, and D were 32 ± 3 nm, 23 ± 2 nm, and 18 ± 2 nm, respectively. Direct measurement revealed interhelical angles of $118 \pm 23^\circ$, $115 \pm 25^\circ$, and $122 \pm 25^\circ$ between helices A and CE, A and D, and CE and D, respectively ($n = 50$), indicating that helices are distributed equally around the ϕ 29HE_{DNA} 3WJ (Figure 3).

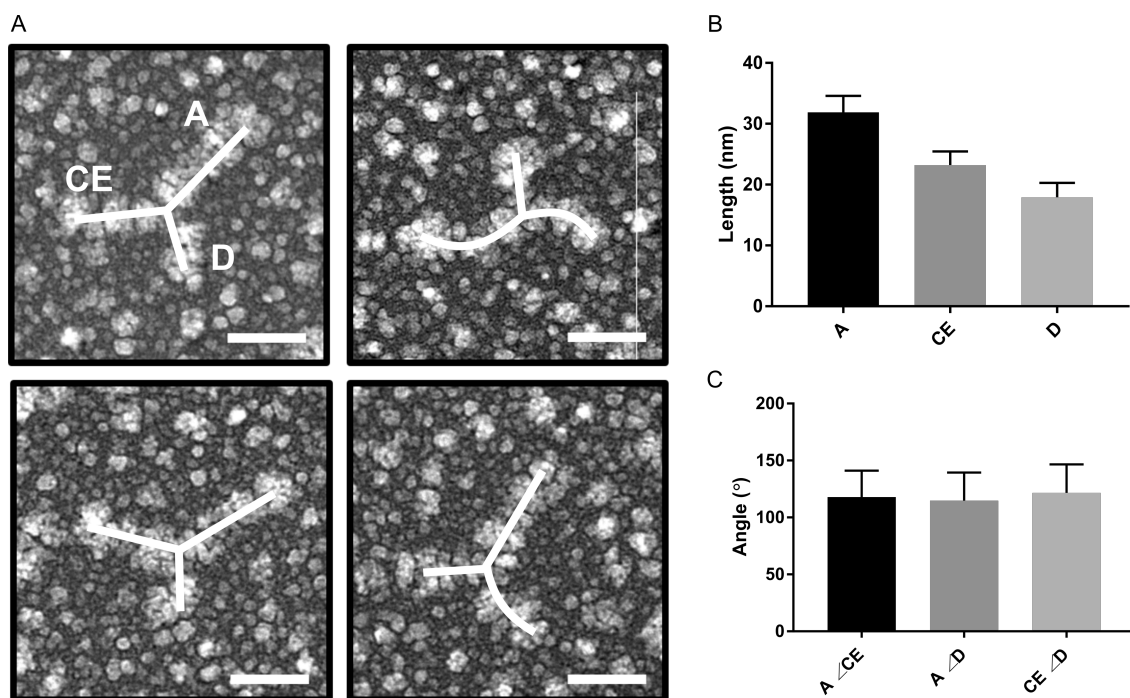


Figure 3 (A) TEM images showing the ϕ 29HE_{DNA} 3WJ. Images are shown in reverse contrast. In one image, helices A, CE, and D are labeled. Scale bars: 20 nm. (B) Lengths of helices A, CE, and D and (C) interhelical angles measured in the ϕ 29HE_{DNA} 3WJ. Results represent means \pm standard deviations ($n = 50$).

Discussion

Helical Coaxial Stacking Predictions

The algorithm Junction Explorer predicts topology and coaxial stacking in RNA multibranch loops. The ‘random forests’ data mining approach leverages a set of decision trees that consider variables such as length and sequence in order to arrive at a coaxial stacking prediction that is 81% or 77% accurate for three- or four-way junctions, respectively²⁵. Junction Explorer accurately predicts helical coaxial stacking between the acceptor stem and T ψ C loop and between the anticodon stem and the D loop based on the lowest free energy secondary structure predicted for the yeast tRNA 4-way junction²²⁻²⁴. Predictions using Junction Explorer²⁵ indicate that the phi29 3WJ belongs to family C and that helices A and D form a coaxial stack (Table 2). These results differ from previous predictions using the Lescoute and Westhof classification system that indicate that the phi29 3WJ belongs to family A, which has no preferred orientation for peripheral helices around the junction^{1, 8}. Both predictions of phi29 3WJ conformation are supported by prior experimental data^{8, 17-20}, and these data are discussed in more detail below (see ‘Helical Arrangement in the Phi29HE_{DNA} 3WJ’). Structures of 3WJs are difficult to predict^{12, 26}, and certain 3WJ helical coaxial stacking predictions differed based on the order in which component strands were input into the Junction Explorer algorithm, *i.e.*, 3WJa-3WJb-3WJc versus 3WJb-3WJc-3WJa versus 3WJc-3WJa-3WJb (Appendix II Table 4). While it is unclear for 3WJs where conflict exists among conformation predictions and for which no external supporting data exist, for certain 3WJs, predictions and prior experimental results are in agreement. For example, for the M2 3WJ, the results for input 3WJc-3WJa-3WJb are consistent with a

prior prediction that it belongs to family B, as well as with prior Förster resonance energy transfer (FRET) data that indicate that its conformation is different from that of the phi29 3WJ⁸. Importantly, predictions made for the phi29 3WJ and the phi29HE_{DNA} 3WJ indicate that both 3WJs belong to family C and that helices A and D stack, suggesting that converting the construct into DNA and extending the peripheral helices does not change the conformation of the 3WJ. Additional data collected on an RNA construct with helix extensions rotated around the 3WJ will help rule out these possibilities.

Helical Arrangement in the Phi29HE_{DNA} 3WJ

Using TEM, we observed that helices A, CE, and D are distributed equally around the phi29HE_{DNA} 3WJ (Figure 3). The conformation of the phi29 3WJ has been explored previously using X-ray crystallography¹⁷⁻¹⁸, pulsed electron paramagnetic resonance (EPR)¹⁹, atomic force microscopy (AFM)²⁷, and FRET^{8, 20}. The results of these studies are discussed in greater detail below and, taken together, support the idea that the phi29 3WJ is a conformationally dynamic, flexible motif in pRNA⁸.

Two structures have been determined for the phi29 3WJ using X-ray crystallography. The structure of a core phi29 3WJ lacking the ability to self-assemble was determined to 3.05 Å, and the structure of a truncated, self-assembling phi29 pRNA that crystallized in a tetramer was determined to 3.5 Å¹⁷⁻¹⁸. Both structures show that helices A and D form a stack; however, the interhelical angles in these structures differ. In the phi29 3WJ monomer, helices A and D are contiguous and helix CE forms an acute angle with helix A, while in the phi29 pRNA tetramer, helix CE is shifted to form a more acute angle with helix D^{8, 12, 17-18}. The stacking of helices A and D and the

position of helix CE at an acute angle relative to the stack is consistent with predictions made for the phi29 3WJ by Junction Explorer as described above. Because metal ion binding affects 3WJ structures²⁸, an important difference between the two structures is the presence of two metal binding sites in the core phi29 3WJ structure, where nucleotide pairs G23/A90 and C24/A89 bind one divalent ion each¹⁸. Also notably, the cytidine at position 24 (C24) in this construct was mutated from the uridine found in the wild-type phi29 sequence and in the pRNA tetramer^{12, 16}. Despite these limitations, the differences between these two structures may suggest that interhelical angles change during pRNA multimerization and ultimately hint at flexibility in the phi29 3WJ⁸.

In contrast to data obtained by X-ray crystallography, the results of EPR studies on a phi29 3WJ in a pRNA dimer show that helices A and D do not stack¹⁹. In these studies, a total of 17 internitroxide distances spanning the 3WJ were measured and pooled with steric chemical constraints to identify 3662 viable models for global 3WJ structure. In each model, helices A and D adopt an acute bend¹⁹. One notable limitation of the construct used in these studies is a strand break and missing residues between wild-type positions C71 and G75¹⁹. Previous crystal structure data indicate that the tri-U bulge (*i.e.*, U72-74) makes tertiary contacts that may be important for 3WJ structure¹⁸, and it is known that deletions in this region can abolish the packaging activity of the phi29 molecular motor^{5, 12}. Despite this, previous FRET studies on a phi29 pRNA dimer support the EPR model²⁰, while more recent FRET studies on a core phi29 3WJ suggest that the distance between helices A and D is larger, on average, than the distances between helices A and C/E and C/E and D⁸.

Additionally, AFM characterization of a helix-extended phi29 RNA 3WJ are consistent with observations that the phi29 3WJ is a flexible, conformationally dynamic element in pRNA ⁸. Indeed, AFM images of these 3WJs show remarkable similarity to the results obtained for the DNA construct used in our studies ²⁷. Unpaired nucleotides at the ends of DNA and RNA helices are known to stack differently ²⁹. For example, in DNA, 5'-dangling ends are most stabilizing, while in RNA, the stability increments for 5'-dangling ends are small, and certain 3'-dangling ends can stabilize a helix more than some base pairs ²⁹. Although inherent differences between DNA and RNA may contribute to differences between our observed results on the phi29HE_{DNA} 3WJ and the organization of the natural phi29 pRNA 3WJ, our data corroborate the AFM data that show helices A, CE, and D are distributed equally around the phi29 3WJ, with no preference for a particular helical arrangement.

Limitations and Future Directions for Determining 3WJ Conformation

Previous studies have suggested that the phi29 3WJ may sample a number of states in a conformational equilibrium ⁸. Although we did not see evidence for discrete conformational states, the nature of our study limited measurement to only those 3WJs that lay relatively flat in a plane, and it is possible that other conformations that tend to project back into the plane are underrepresented. Additionally, the process of air-drying and adsorption to a surface can distort macromolecular structures. It is possible that by comparison to existing data ⁸, future TEM studies on an M2 3WJ will help assess how representative 3WJs observed by TEM are of 3WJs in a solution state. Alternatively, cryo-electron microscopy may be more promising for future studies on 3WJ

conformation, as this technique limits molecular rearrangements during preparation and allows for single particle reconstruction in three dimensions³⁰.

Conclusion

The interhelical angles in a phi29 3WJ can be measured directly using transmission electron microscopy (TEM). The results presented here are in agreement with previous data showing that the phi29 3WJ is a flexible, conformationally dynamic element in pRNA. The helical coaxial stacking predictions for phylogenetically related 3WJs differ, and the preferred spatial orientation of helices around certain 3WJs is a suggested driving force behind their thermodynamic stabilities and multimerization properties *in vitro*^{6-8, 12, 19, 31}. Additionally, because 3WJs are important determinants of global RNA structure, the accurate prediction of junction structures is important for 3D structure prediction. Differences in the relative orientations of helices around different 3WJs may help explain why certain junctions are more thermodynamically stable than others¹² and may provide new opportunities for fine-tuning the self-assembly of certain sequences in RNA engineering. As shown here, TEM can be used to probe the conformational landscapes of 3WJs in order to develop knowledge about RNA structure-energetics-function relationships that may prove useful in both basic research and nanotechnology.

Materials and Methods

Helix-Extended 3WJ Construct Design

The peripheral helices A, CE, and D of a core tripartite phi29 pRNA 3WJ designed as described previously¹² were modified with extensions to 100, 80, and 50 bp, respectively, using sequences previously reported for similar experiments on the

Tetrahymena group I ribozyme ¹⁴ (Appendix II Table 2). Extensions were chosen to approximate the relative helical length proportions found in natural pRNA, *i.e.*, in natural pRNA, helix A is roughly four times longer than helix D, and helix CE is roughly two times longer than helix D, while in the helix-extended construct, helix A is two times longer than helix D, and helix CE is 1.6 times longer than helix D (Figure 1). A phi29 helix-extended DNA 3WJ (phi29HE_{DNA}) construct was used for preliminary investigations.

Secondary Structure and Family/Helical Coaxial Stacking Predictions

The secondary structure of the phi29HE_{DNA} 3WJ was predicted using the secondary structure prediction program RNA Structure ²¹ as described previously ¹². Briefly, strands 3WJa, 3WJb, and 3WJc were folded as a single strand by joining the strands 3WJa and 3WJb and 3WJb and 3WJc with 5' – aaaa – 3' hairpins. Predictions were not affected by the positions of the hairpins, *i.e.*, whether the hairpins were placed between strands 3WJa and 3WJb and strands 3WJb and 3WJc, between strands 3WJb and 3WJc and strands 3WJc and 3WJa, or between strands 3WJc and 3WJa and strands 3WJa and 3WJb. For each of these inputs, the target structure was the only predicted structure. Predicted free energies for folded 3WJ strands alone or in pairwise combinations were less favorable than the target structure. A table of predicted free energies for each strand alone, in pairwise combinations, and the 3WJ is provided in Appendix II Table 3. The algorithm Junction Explorer was used to predict 3WJ family and helical coaxial stacking interactions using dot bracket files written in RNA Structure ^{21, 25}. A table of predicted families and helical coaxial stacking interactions is provided in Appendix II

Table 4. Strands 3WJa, 3WJb, and 3WJc were purchased as Ultramer[®] DNA Oligos from IDT and prepared according to the manufacturer's instructions.

Dynamic Light Scattering (DLS)

Strands 3WJa, 3WJb, and 3WJc for previously designed RNA 3WJs were mixed at 50 μ M, and strands 3WJa, 3WJb, and 3WJc for the phi29HE_{DNA} 3WJ were mixed at 1.5 μ M and room temperature in RNase-free water to assemble a 3WJ. Reactions were dried, resuspended in standard melt buffer (1 M NaCl, 10 mM sodium cacodylate, 0.5 mM EDTA, pH 7.0), and refrigerated overnight at -20°C. The next day, following equilibration to room temperature, dynamic light scattering (DLS) was performed on 50 μ L assembled 3WJ using a pUNK (Unchained Labs) DLS instrument at 20°C.

Electrophoretic Mobility Shift Assays

The 3WJ can be assembled from three strands 3WJa, 3WJb, and 3WJc mixed in equimolar concentrations. Formation of the phi29HE_{DNA} 3WJ was monitored as described previously¹² using an electrophoretic gel mobility shift assay. Briefly, DNA at a concentration of 1.5 μ M (approximately 600 ng) in 35 mM Tris-HCl, pH 7.50 was heated to 50°C for 10 minutes and 42°C for 5 minutes before cooling to room temperature¹⁴. The assembled 3WJ was mixed with sucrose loading dye and run in TAE buffer at 80 V and 4°C in pre-cooled, 1% (w/v) agarose stained with ethidium bromide. Mobility of each single strand, pairwise combination, and the 3WJ were monitored.

Transmission Electron Microscopy

Methods for preparing nucleic acid samples for electron microscopy have been described previously¹⁴⁻¹⁵ and were used with some modifications. The phi29HE_{DNA}

3WJ was assembled from three strands 3WJa, 3WJb, and 3WJc mixed at a final concentration of 50 nM in 35 mM Tris-HCl, pH 7.50 and heated to 50°C for 10 minutes and 42°C for 5 minutes before cooling to room temperature. Previously, spermidine at a final concentration of 250 μ M was added to the *Tetrahymena* group I ribozyme for TEM studies. Spermidine can promote DNA condensation³², and in our own studies, we did not observe extended phi29HE_{DNA} 3WJs when spermidine was added to assembly reactions. We therefore omitted spermidine in our final assembly protocol. To prepare grids, a previously described glycerol spraying/low angle rotary shadowing technique³³ was used with some modifications. Briefly, 200/300 copper mesh grids were cleaned with a 95% (v/v) ethanol and 5% (v/v) HCl solution, rinsed with ethanol, and dried at room temperature. 3WJ samples were mixed with glycerol at a final concentration of 50% (v/v). Approximately 25 μ L 3WJ:glycerol sample was loaded into a Pasche single-action airbrush adjusted to produce fine droplets and sprayed at 15 psi onto freshly cleaved mica positioned 20-30 cm from the tip of the airbrush. The mica with sprayed 3WJ:glycerol was immediately rotary shadowed at 8-10° with platinum-carbon (35 s) and carbon (12 s) at approximately 2.5 kV and 70 mA using a JFD 9000 (JEOL). The heavy metal replica was floated off onto water and picked up onto clean, air-dried grids. After drying at room temperature, replicas were imaged on a JEOL 2000FX electron microscope at 80,000X magnification. Images were scanned with an Epson Perfection V750 Pro. Particles that were well isolated (*i.e.*, non-overlapping) and that showed three distinct helices emerging from a central core were selected for helix and angle measurements in ImageJ.

References

1. Lescoute, A.; Westhof, E., Topology of three-way junctions in folded RNAs. *RNA* 2006, 12, 83-93.
2. Westhof, E.; Masquida, B.; Jossinet, F., Predicting and modeling RNA architecture. *Cold Spring Harbor Perspectives in Biology* 2011, 3 (2).
3. de la Peña, M.; Dufour, D.; Gallego, J., Three-way RNA junctions with remote tertiary contacts: A recurrent and highly versatile fold. *RNA* 2009, 15 (11), 1949-1964.
4. Guo, P.; Erickson, S.; Anderson, D., A small viral RNA is required for in vitro packaging of bacteriophage phi 29 DNA. *Science* 1987, 236, 690-694.
5. Zhao, W.; Saha, M.; Ke, A.; Morais, M.; Jardine, P.; Grimes, S., A three-helix junction is the interface between two functional domains of prohead RNA in phi29 DNA packaging. *Journal of Virology* 2012, 86, 11625-11632.
6. Gu, X.; Schroeder, S., Different sequences show similar quaternary interaction stabilities in prohead viral RNA self-assembly. *Journal of Biological Chemistry* 2011, 286, 14419-14426.
7. Hao, Y.; Kieft, J. S., Diverse self-association properties within a family of phage packaging RNAs. *RNA* 2014, 20, 1-16.
8. Hao, Y.; Kieft, J. S., Three-way junction conformation dictates self-association of phage packaging RNAs. *RNA Biology* 2016, 13 (7), 635-45.
9. Hao, C.; Li, X.; Tian, C.; Jiang, W.; Wang, G.; Mao, C., Construction of RNA nanocages by re-engineering the packaging RNA of Phi29 bacteriophage. *Nature Communications* 2014, 5, 3890.
10. Jaeger, L.; Leontis, N. B., Tecto-RNA: One-dimensional self-assembly through tertiary interactions. *Angewandte Chemie International Edition* 2000, 39 (14), 2521-2524.
11. Chworos, A.; Severcan, I.; Koyfman, A. Y.; Weinkam, P.; Oroudjev, E.; Hansma, H. G.; Jaeger, L., Building programmable jigsaw puzzles with RNA. *Science* 2004, 306 (5704), 2068-2072.

12. Hill, A. C.; Schroeder, S. J., Thermodynamic stabilities of three-way junction nanomotifs in prohead RNA. *RNA* 2017.
13. Liu, B.; Diamond, J. M.; Mathews, D. H.; Turner, D. H., Fluorescence competition and optical melting measurements of RNA three-way multibranch loops provide a revised model for thermodynamic parameters. *Biochemistry* 2011, 50 (5), 640-653.
14. Nakamura, T. M.; Wang, Y. H.; Zaug, A. J.; Griffith, J. D.; Cech, T. R., Relative orientation of RNA helices in a group 1 ribozyme determined by helix extension electron microscopy. *The EMBO Journal* 1995, 14 (19), 4849-4859.
15. Wang, Y. H.; Murphy, F. L.; Cech, T. R.; Griffith, J. D., Visualization of a tertiary structural domain of the *Tetrahymena* group I intron by electron microscopy. *Journal of Molecular Biology* 1994, 236 (1), 64-71.
16. Bailey, S.; Wichitwechkarn, J.; Johnson, D.; Reilly, B.; Anderson, D.; Bodley, J., Phylogenetic analysis and secondary structure of the *Bacillus subtilis* bacteriophage RNA required for DNA packaging. *Journal of Biological Chemistry* 1990, 265, 22365-22370.
17. Ding, F.; Lu, C.; Zhao, W.; Rajashankar, K.; Anderson, D.; Jardine, P.; Grimes, S.; Ke, A., Structure and assembly of the essential RNA ring component of a viral DNA packaging motor. *Proceedings of the National Academy of Sciences* 2011, 108, 7357-7362.
18. Zhang, H.; Endrizzi, J.; Shu, Y.; Haque, F.; Sauter, C.; Shlyakhtenko, L.; Lyubchenko, Y.; Guo, P.; Chi, Y., Crystal structure of 3WJ core revealing divalent ion-promoted thermostability and assembly of the Phi29 hexameric motor pRNA. *RNA* 2013, 19, 1226-1237.
19. Zhang, X.; Tung, C.-S.; Sowa, G. Z.; Hatmal, M. M.; Haworth, I. S.; Qin, P. Z., Global structure of a three-way junction in a phi29 packaging RNA dimer determined using site-directed spin labeling. *Journal of the American Chemical Society* 2012, 134 (5), 2644-2652.
20. Shu, D.; Zhang, H.; Petrenko, R.; Meller, J.; Guo, P., Dual-channel single-molecule fluorescence resonance energy transfer to establish distance parameters for RNA nanoparticles. *ACS Nano* 2010, 4 (11), 6843-53.

21. Mathews, D. H.; Disney, M. D.; Childs, J. L.; Schroeder, S. J.; Zuker, M.; Turner, D. H., Incorporating chemical modification constraints into a dynamic programming algorithm for prediction of RNA secondary structure. *Proceedings of the National Academy of Sciences of the United States of America* 2004, 101 (19), 7287-92.
22. Kim, S. H.; Suddath, F. L.; Quigley, G. J.; McPherson, A.; Sussman, J. L.; Wang, A. H. J.; Seeman, N. C.; Rich, A., Three-dimensional tertiary structure of yeast phenylalanine transfer RNA. *Science* 1974, 185 (4149), 435.
23. Robertus, J. D.; Ladner, J. E.; Finch, J. T.; Rhodes, D.; Brown, R. S.; Clark, B. F.; Klug, A., Structure of yeast phenylalanine tRNA at 3 Å resolution. *Nature* 1974, 250 (467), 546-51.
24. Shi, H.; Moore, P. B., The crystal structure of yeast phenylalanine tRNA at 1.93 Å resolution: a classic structure revisited. *RNA* 2000, 6 (8), 1091-1105.
25. Laing, C.; Wen, D.; Wang, J. T. L.; Schlick, T., Predicting coaxial helical stacking in RNA junctions. *Nucleic Acids Research* 2012, 40 (2), 487-498.
26. Tyagi, R.; Mathews, D. H., Predicting helical coaxial stacking in RNA multibranch loops. *RNA* 2007, 13 (7), 939-951.
27. Cui, D.; Zhang, C.; Liu, B.; Shu, Y.; Du, T.; Shu, D.; Wang, K.; Dai, F.; Liu, Y.; Li, C.; Pan, F.; Yang, Y.; Ni, J.; Li, H.; Brand-Saberi, B.; Guo, P., Regression of gastric cancer by systemic injection of RNA nanoparticles carrying both ligand and siRNA. *Scientific Reports* 2015, 5, 10726.
28. Bartova, S.; Pechlaner, M.; Donghi, D.; Sigel, R. K. O., Studying metal ion binding properties of a three-way junction RNA by heteronuclear NMR. *Journal of Biological Inorganic Chemistry* 2016, 21 (3), 319-328.
29. Bloomfield, V. A.; Crothers, D. M.; Tinoco, I., Jr., *Nucleic Acids: Structures, Properties, and Functions*. University Science Books: Sausalito, California, 2000; pp 259-334.
30. Cabra, V.; Samsó, M., Do's and Don'ts of Cryo-electron Microscopy: A primer on sample preparation and high quality data collection for macromolecular 3D reconstruction. *Journal of Visualized Experiments* 2015, (95), 52311.

31. Hill, A. C.; Bartley, L. E.; Schroeder, S. J., Prohead RNA: A noncoding viral RNA of novel structure and function. *Wiley Interdisciplinary Reviews RNA* 2016, 7 (4), 428-37.
32. Raspaud, E.; Olvera de la Cruz, M.; Sikorav, J. L.; Livolant, F., Precipitation of DNA by polyamines: a polyelectrolyte behavior. *Biophysical Journal* 1998, 74 (1), 381-393.
33. Aebi, U.; Baschong, W., *Glycerol spraying/low-angle rotary metal shadowing*. 2006.

Chapter 6: Conclusion

Recent advances in RNA research, such as the engineering of CRISPR¹⁻³ and RNAi⁴, demonstrate how knowledge of natural systems can fuel innovations that shape the RNA World. A conserved three-way junction (3WJ) in prohead or packaging RNA (pRNA) offers a unique setting for studying RNA, as new insights into structure-energetics-function relationships can advance basic knowledge and also inform nanotechnology. In nature, the pRNA 3WJ is critical for the activity of the phi29 viral molecular machine⁵⁻⁶. Removed from this context, the 3WJ is used as a nano-scale tool, for example, as a nanoparticle in the delivery of therapeutic drugs⁷. In particular, connections made among thermodynamics, structure, and cell stability can focus efforts in 3WJ engineering by identifying and developing rules for sequences that may be most useful *in vivo*. The biophysical studies presented here contribute to parameters for improving RNA secondary structure prediction from sequence, provide knowledge for further investigating a structural mechanism underlying pRNA self-assembly and stability, and expand the number of useful sequences for RNA nanotechnology.

Phylogenetically related pRNA 3WJs share a conserved function and fold but are highly divergent in terms of sequence⁸. The thermodynamics data presented here show that related 3WJs also have different energetic stabilities⁹. Differences in 3WJ energetics were hypothesized to counterbalance differences in loop-loop interaction energetics, such that the overall energetics of pRNA dimerization would be preserved as shown previously by Gu & Schroeder⁸. The presented data indicate that for certain sequences, including GA1 and phi29, 3WJs offset loop-loop interaction stabilities. However, for other sequences, including SF5 and M2, both the 3WJ and loop-loop

interactions are stabilizing ⁹. The combination of favorable interactions may help explain why the SF5 and M2 sequences self-assemble with the highest propensities *in vitro* ^{8, 10}. Furthermore, the measured free energies span over 20 kcal mol⁻¹, and certain 3WJs are surprisingly more stable than predicted by currently available RNA secondary structure prediction programs ⁹. The wide range of thermodynamic stabilities observed may be explained partially by differences in sequence, for example, in the unpaired nucleotides at the 3WJ core. However, the energetics of phi29 3WJ deletion mutants do not correlate with the number of unpaired nucleotides remaining in the junction, and only a weak trend was observed between stability and the number of unpaired nucleotides at the 3WJ among related pRNA sequences, suggesting that stability differences are not explained by sequence alone ⁹. It is possible that the study of a larger dataset, with different numbers and characters of nucleotides positioned around the 3WJ, would help reveal trends that are not readily apparent for the 3WJs investigated here. Alternatively, unpaired nucleotides may represent only one piece of a larger 3WJ energetics puzzle.

Indeed, measured stabilities might be better understood in light of secondary and tertiary interactions, such as coaxial stacking of helices across the junction, which is common in 3WJ structures and which can be thermodynamically favorable ¹¹⁻¹². In particular, differences in coaxial stacking may explain differences in energetics among pRNA 3WJs. Proof-of-concept transmission electron microscopy (TEM) studies on a helix-extended phi29 3WJ showed that peripheral helices are distributed equally around the junction, with no preferred helical coaxial stacking interactions. These results are consistent with previously established models for the conformation of the phi29 3WJ ¹³⁻

¹⁸. However, the methods used here carry certain limitations. First, helix extensions may influence conformation at the 3WJ. For the studies reported here, extensions were chosen to approximate the relative helix length proportions found in natural pRNA in order to minimize this possibility. Future studies may shuffle extensions around the junction and monitor for changes in the measured 3WJ conformation. Second, only 3WJs that lay relatively flat in the plane were amenable to measurement, and these 3WJs may or may not represent a conformation adopted by the phi29 3WJ in a solution state. Additionally, 3WJs with conformations that tended to project helices back into the plane are not represented in these data. A different method, such as electron tomography or cryo-electron microscopy (cryo-EM), may prove more useful for examining 3WJ conformation in three-dimensional space. Finally, the spraying and heavy metal shadowing technique used here ¹⁹ is resolution limiting and also may influence the conformation of the 3WJ. Recent advances in cryo-EM and single particle reconstruction achieve near-atomic resolutions that rival X-ray crystallographic and NMR methods, and cryo-EM has the noted advantage of rapid freezing, which avoids drying artifacts and macromolecular rearrangements that can occur during sample preparation ²⁰⁻²¹. Future studies on 3WJ conformation, for example using cryo-EM, may contribute to a better understanding of the mechanisms underlying 3WJ energetics.

The energetic stability of the prototype phi29 pRNA 3WJ contributes to its use as a nanoparticle for therapeutic drug delivery ⁷. Rich sequence and structural diversity among phylogenetically related pRNA 3WJs may contribute to the development of new building blocks for nanotechnology, and the thermodynamics data reported here indicate that certain pRNA 3WJs are considerably more stable than the phi29 3WJ ⁹.

Studies in human blood serum and in cells tested the correlation between 3WJ energetic and physiologic stabilities. Although energetic and physiologic stabilities are not always correlated, some 3WJs are both more thermodynamically stable and more stable in serum than the phi29 3WJ. In fact, the M2 3WJ is 14.5 kcal mol⁻¹ more stable⁹ and up to 70% more stable in serum than the phi29 3WJ. Like energetic stability, serum stability is not fully explained by 3WJ sequence and may be modulated by 3WJ shape, which is known to confound nuclease degradation in some RNAs, such as subgenomic flaviviral RNA²². Recent studies have shown that the M2 3WJ adopts a conformation that is different from the phi29 3WJ in solution, and this conformation is implicated in the ability of the M2 sequence to form thermostable multimers *in vitro*¹⁸. Future studies, for example using cryo-EM as described above, that explore the sequence dependence of 3WJ structure may be useful for unraveling the mechanisms behind 3WJ energetic and physiologic stability.

Results from uptake studies in neuroblastoma cells indicate that naked 3WJs accumulate intracellularly to 20% over 24 hours. One limitation of this study is the use of a three-component RNA system, because it is difficult to eliminate the possibility that the measured uptake reflects only a single strand rather than the assembled 3WJ. Data for uptake of a single RNA strand are able to address this possibility only indirectly, and the use of a single-stranded 3WJ construct may be useful in future studies. Additionally, although incubation in serum-free media was important for reducing the effects of differential 3WJ serum sensitivity on cell uptake, the absence of serum in growth media can compromise cell quality²³⁻²⁶ and therefore the measured cell uptake may not reflect accurately cell uptake *in vivo*. Despite these limitations, the

presented results support the idea that phi29-alternative 3WJs may be useful in nanotechnology, such as in the stabilization of RNAs for drug delivery.

Knowledge about RNA structure-energetics-function relationships can develop existing tools to better navigate the RNA World and can support the engineering of new RNA tools for nanotechnology. In particular, a better grasp of the interplay between structure and energetics can inform better drug design principles. The thermodynamics, structure, and cell stability data presented here provide a foundation for further developing phi29-alternative 3WJs as nanoparticles for therapeutic drug delivery *in vivo*. In the future, the energetically and physiologically stable SF5 and M2 sequences could be leveraged as efficient pRNA-based nanoparticles that persist at body temperature and in the presence of serum nucleases, while continued investigations into the conformations of these sequences could reveal a structural mechanism behind their stabilities and propensities for self-assembly *in vitro*. An understanding of 3WJ stability and structure will aid in the development of new hypotheses surrounding structure-energetics-function relationships, help refine current parameters for prediction of RNA multibranch loops from sequence, and contribute new building blocks in the design of functional supramolecular structures.

References

1. Gasiunas, G.; Barrangou, R.; Horvath, P.; Siksnys, V., Cas9–crRNA ribonucleoprotein complex mediates specific DNA cleavage for adaptive immunity in bacteria. *Proceedings of the National Academy of Sciences* 2012, 109 (39), E2579–E2586.
2. Jinek, M.; Chylinski, K.; Fonfara, I.; Hauer, M.; Doudna, J. A.; Charpentier, E., A programmable dual-RNA-guided DNA endonuclease in adaptive bacterial immunity. *Science* 2012, 337 (6096), 816-21.
3. Cong, L.; Ran, F. A.; Cox, D.; Lin, S.; Barretto, R.; Habib, N.; Hsu, P. D.; Wu, X.; Jiang, W.; Marraffini, L. A.; Zhang, F., Multiplex genome engineering using CRISPR/Cas systems. *Science (New York, N.Y.)* 2013, 339 (6121), 819-823.
4. Garber, K., Worth the RISC? *Nature Biotechnology* 2017, 35 (3), 198-202.
5. Reid, R.; Zhang, F.; Benson, S.; Anderson, D., Probing the structure of bacteriophage phi29 prohead RNA with specific mutations. *Journal of Biological Chemistry* 1994, 269, 18656-18661.
6. Zhao, W.; Saha, M.; Ke, A.; Morais, M.; Jardine, P.; Grimes, S., A three-helix junction is the interface between two functional domains of prohead RNA in phi29 DNA packaging. *Journal of Virology* 2012, 86, 11625-11632.
7. Shu, D.; Shu, Y.; Haque, F.; Abdelmawla, S.; Guo, P., Thermodynamically stable RNA three-way junction for constructing multifunctional nanoparticles for delivery of therapeutics. *Nature Nanotechnology* 2011, 6, 658-667.
8. Gu, X.; Schroeder, S., Different sequences show similar quaternary interaction stabilities in prohead viral RNA self-assembly. *Journal of Biological Chemistry* 2011, 286, 14419-14426.
9. Hill, A. C.; Schroeder, S. J., Thermodynamic stabilities of three-way junction nanomotifs in prohead RNA. *RNA* 2017.
10. Hao, Y.; Kieft, J. S., Diverse self-association properties within a family of phage packaging RNAs. *RNA* 2014, 20, 1-16.

11. Lescoute, A.; Westhof, E., Topology of three-way junctions in folded RNAs. *RNA* 2006, 12, 83-93.
12. Liu, B.; Diamond, J. M.; Mathews, D. H.; Turner, D. H., Fluorescence competition and optical melting measurements of RNA three-way multibranch loops provide a revised model for thermodynamic parameters. *Biochemistry* 2011, 50 (5), 640-653.
13. Ding, F.; Lu, C.; Zhao, W.; Rajashankar, K.; Anderson, D.; Jardine, P.; Grimes, S.; Ke, A., Structure and assembly of the essential RNA ring component of a viral DNA packaging motor. *Proceedings of the National Academy of Sciences* 2011, 108, 7357-7362.
14. Zhang, H.; Endrizzi, J.; Shu, Y.; Haque, F.; Sauter, C.; Shlyakhtenko, L.; Lyubchenko, Y.; Guo, P.; Chi, Y., Crystal structure of 3WJ core revealing divalent ion-promoted thermostability and assembly of the Phi29 hexameric motor pRNA. *RNA* 2013, 19, 1226-1237.
15. Zhang, X.; Tung, C.-S.; Sowa, G. Z.; Hatmal, M. M.; Haworth, I. S.; Qin, P. Z., Global structure of a three-way junction in a phi29 packaging RNA dimer determined using site-directed spin labeling. *Journal of the American Chemical Society* 2012, 134 (5), 2644-2652.
16. Cui, D.; Zhang, C.; Liu, B.; Shu, Y.; Du, T.; Shu, D.; Wang, K.; Dai, F.; Liu, Y.; Li, C.; Pan, F.; Yang, Y.; Ni, J.; Li, H.; Brand-Saberi, B.; Guo, P., Regression of gastric cancer by systemic injection of RNA nanoparticles carrying both ligand and siRNA. *Scientific Reports* 2015, 5, 10726.
17. Shu, D.; Zhang, H.; Petrenko, R.; Meller, J.; Guo, P., Dual-channel single-molecule fluorescence resonance energy transfer to establish distance parameters for RNA nanoparticles. *ACS Nano* 2010, 4 (11), 6843-53.
18. Hao, Y.; Kieft, J. S., Three-way junction conformation dictates self-association of phage packaging RNAs. *RNA Biology* 2016, 13 (7), 635-45.
19. Aebi, U.; Baschong, W., Glycerol spraying/low-angle rotary metal shadowing. 2006.
20. Frank, J., Advances in the field of single-particle cryo-electron microscopy over the last decade. *Nature Protocols* 2017, 12 (2), 209-212.

21. Cabra, V.; Samsó, M., Do's and Don'ts of Cryo-electron Microscopy: A Primer on Sample Preparation and High Quality Data Collection for Macromolecular 3D Reconstruction. *Journal of Visualized Experiments* 2015, (95), 52311.
22. Chapman, E. G.; Costantino, D. A.; Rabe, J. L.; Moon, S. L.; Wilusz, J.; Nix, J. C.; Kieft, J. S., The structural basis of pathogenic subgenomic flavivirus RNA (sfRNA) production. *Science* 2014, 344 (6181), 307.
23. Krystosek, A., Neurite formation by neuroblastoma-glioma hybrid cells (NG108-15) in defined medium: stochastic initiation with persistence of differentiated functions. *Journal of Cellular Physiology* 1985, 125 (2), 319-29.
24. Seidman, K. J. N.; Barsuk, J. H.; Johnson, R. F.; Weyhenmeyer, J. A., Differentiation of NG108-15 neuroblastoma cells by serum starvation or dimethyl sulfoxide results in marked differences in angiotensin II receptor subtype expression. *Journal of Neurochemistry* 1996, 66 (3), 1011-1018.
25. Li, J.; Lee, Y.; Johansson, H. J.; Mäger, I.; Vader, P.; Nordin, J. Z.; Wiklander, O. P. B.; Lehtiö, J.; Wood, M. J. A.; Andaloussi, S. E. L., Serum-free culture alters the quantity and protein composition of neuroblastoma-derived extracellular vesicles. *Journal of Extracellular Vesicles* 2015, 4, 10.3402/jev.v4.26883.
26. Howard, M. K.; Burke, L. C.; Mailhos, C.; Pizzey, A.; Gilbert, C. S.; Durward Lawson, W.; Collins, M. K. L.; Thomas, N. S. B.; Latchman, D. S., Cell cycle arrest of proliferating neuronal cells by serum deprivation can result in either apoptosis or differentiation. *Journal of Neurochemistry* 1993, 60 (5), 1783-1791.

Appendix I

Supplementary Information for “Thermodynamic Stabilities of Three-Way Junction Nanomotifs in Prohead RNA”

The following appendix was published as supplementary information in similar form in *RNA* by the author of this dissertation. All text and figures are taken with the permissions of a Creative Commons license.

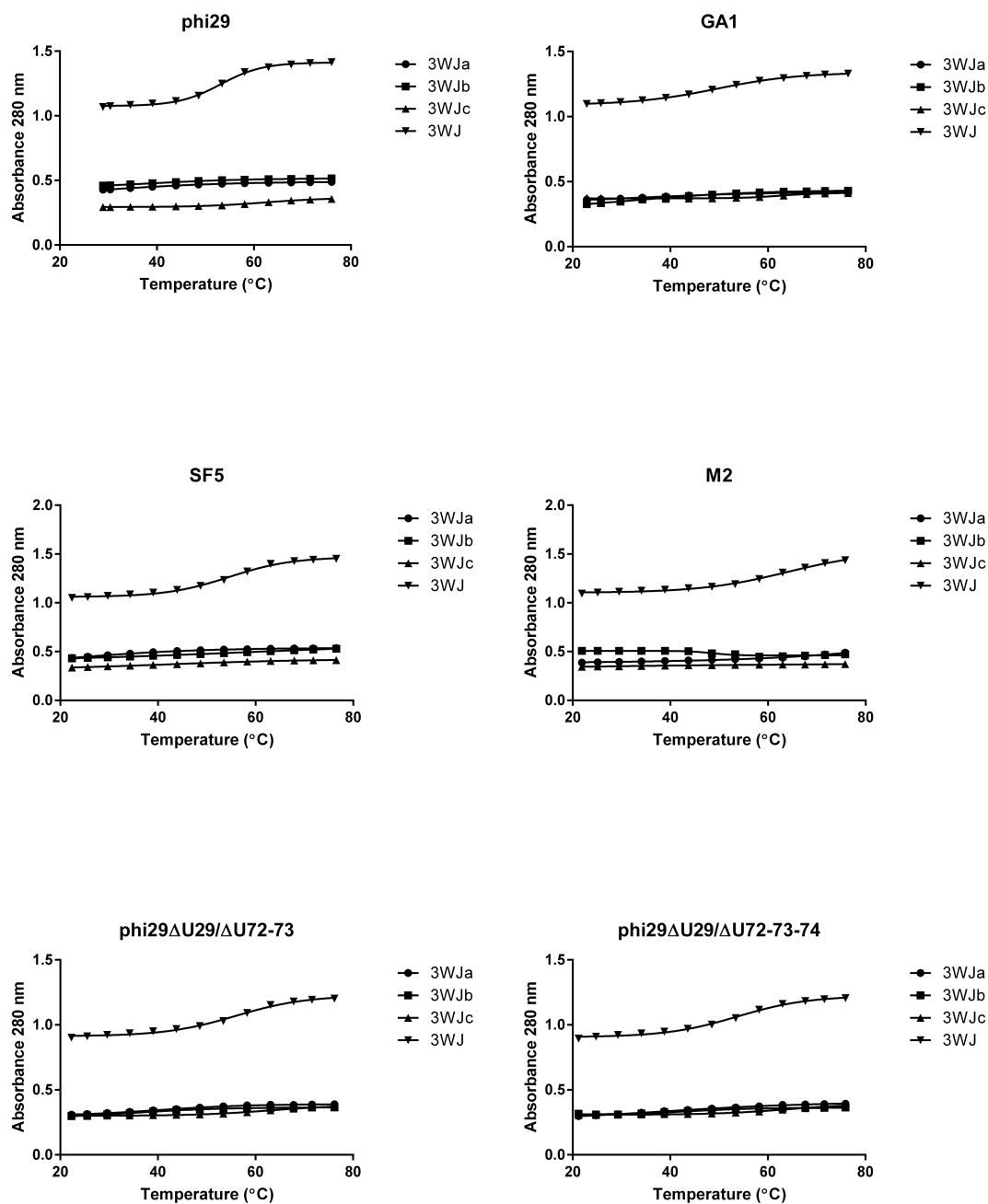


Figure 1 Optical melting data for single strands 3WJa, 3WJb, 3WJc, and the assembled 3WJ in standard melt buffer (1 M sodium chloride, 10 mM sodium cacodylate, 0.5 mM EDTA, pH 7.0)¹.

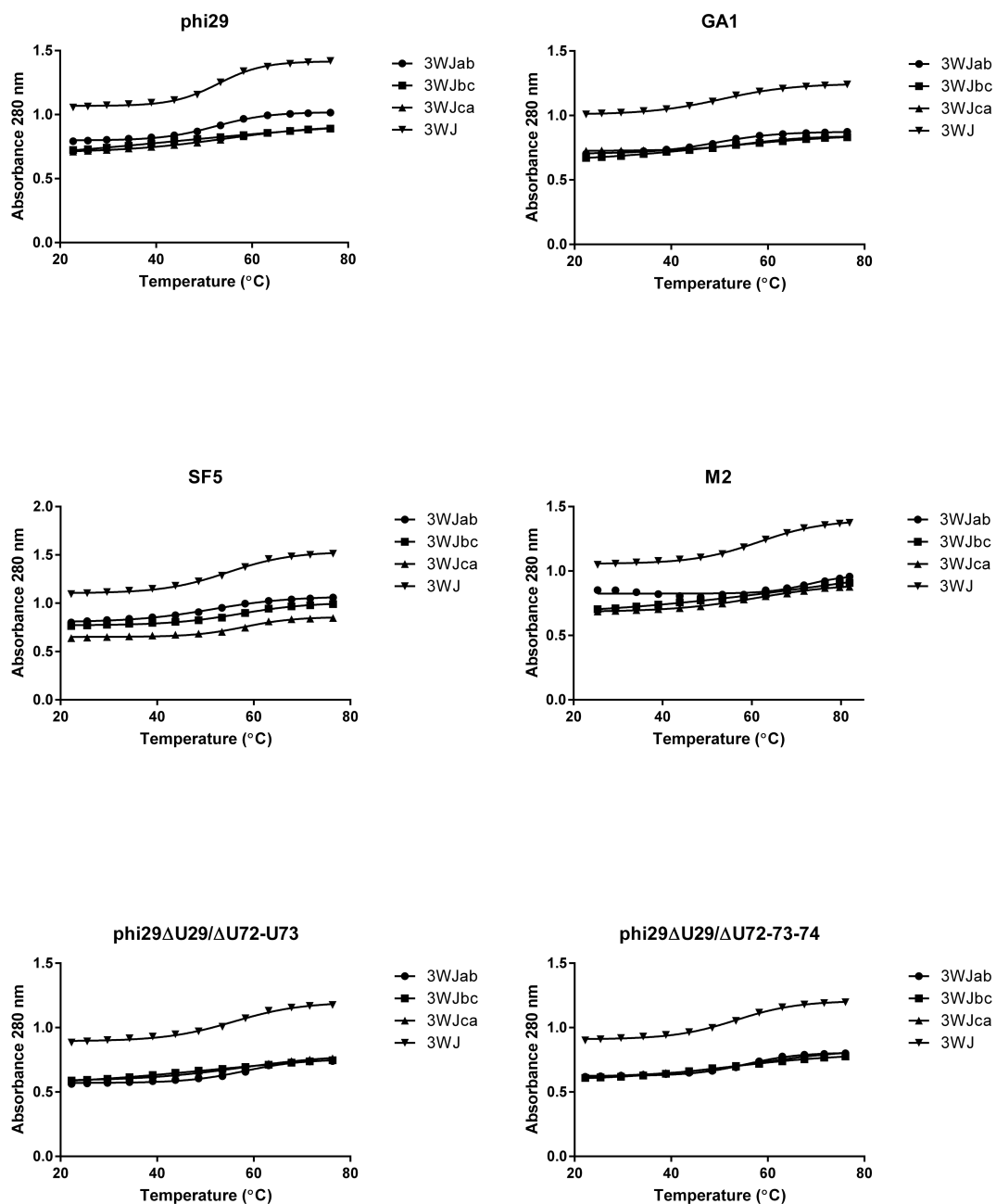


Figure 2 Optical melting data for pairwise stands 3WJab (*i.e.*, 3WJa + 3WJb), 3WJbc (*i.e.*, 3WJb + 3WJc), 3WJca (*i.e.*, 3WJc + 3WJa), and the assembled 3WJ in standard melt buffer (1 M sodium chloride, 10 mM sodium cacodylate, 0.5 mM EDTA, pH 7.0)¹.

Table 1 Comparison of predicted and experimental free energies.

Sequence	ΔG_{37} (kcal mol ⁻¹)											
	RNA Structure		RNAfold		mfold		RNAsoft		Experimental			
	Construct	3WJ	Construct	3WJ	Construct	3WJ	Construct	3WJ	Construct	3WJ		
Phi29	-29.2	1.9	-28.5	2.6	-30.1	1.0	-29.0	2.1	-26.5	4.6		
GAI	-28.1	1.7	-29.3	0.5	-29.5	0.3	n/a*	n/a*	-27.9	1.9		
SF5	-27.3	3.4	-27.4	3.3	-28.3	2.4	-26.8	3.9	-35.0	-4.3		
M2	-31.7	-1.7	-31.4	-1.4	-33.0	-3.0	-32.3	-2.3	-39.9	-9.9		
Phi29 _{ΔU29}	-29.1	2.0	-29.1	2.0	-29.5	1.6	-28.4	2.7	-25.8	5.3		
Phi29 _{ΔU29/ΔU72}	-29.1	2.0	-29.1	2.0	-29.5	1.6	-28.4	2.7	-25.8	5.3		
Phi29 _{ΔU29/ΔU72-73}	-29.1	2.0	-29.1	2.0	-29.3	1.8	-28.2	2.9	-34.4	-3.3		
Phi29 _{ΔU29/ΔU72-73-74}	-28.9	2.2	-29.8	1.3	-29.0	2.1	-27.9	3.2	-30.5	0.6		
Phi29 _{ΔU72}	-29.2	1.9	-28.5	2.6	-30.1	1.0	-29.0	2.1	-26.4	4.7		
Phi29 _{ΔU72-73}	-29.0	2.1	-28.5	2.6	-29.9	1.2	-28.8	2.3	-20.9	10.2		
Phi29 _{ΔU72-73-74}	-28.8	2.3	-28.9	2.2	-29.6	1.5	-28.5	2.6	-25.8	5.3		

Table 1 Calculated secondary structure stabilities for pRNA 3WJs. For predictions in RNA Structure, RNAfold, and mfold, pRNA strands 3WJa and 3WJb as well as 3WJb and 3WJc were joined with a 5' – aaaa – 3' hairpin and then the construct was folded as a single strand. To correct for the added hairpins, two 5' – aaaa – 3' hairpin penalties and three initiation terms were subtracted from the secondary structure stabilities output by RNA Structure, RNAfold, and mfold. For stabilities predicted by RNAsoft, one 5' – aaaa – 3' hairpin penalty and two initiation terms were subtracted. *RNAsoft did not output a secondary structure for the GAI pRNA 3WJ construct due to computational time limitations.

Table 2 Thermodynamic parameters for pRNA constructs with metal ions. *Optical melts of the GA1 3WJ in 100 mM Na⁺ and 10 mM Mg²⁺ did not meet the van't Hoff plot goodness of linear fit cutoff criterion of ≥ 0.90 .

Condition	ΔH (kcal mol ⁻¹)				ΔS (cal mol ⁻¹ K ⁻¹)				ΔG_{37} (kcal mol ⁻¹)			
	Phi29	GAI	SF5	M2	Phi29	GAI	SF5	M2	Phi29	GAI	SF5	M2
1 M Na ⁺	-231.6	-358.2	-308.1	-354.2	-663.5	-1055.6	-889.0	-1015.9	-25.8	-30.8	-32.3	-39.1
100 mM Na ⁺	-226.7	-278.8	-189.7	-167.4	-655.0	-840.6	-560.9	-478.3	-23.5	-18.1	-15.7	-19.0
100 mM Na ⁺ + 10 mM Mg ²⁺	-223.2	n/a*	-292.5	-310.5	-639.2	n/a*	-851.7	-880.7	-25.0	n/a*	-28.3	-37.4
100 mM Na ⁺ + 10 mM spermidine	-235.9	-311.1	-540.8	-604.7	-679.7	-900.8	-1594.9	-1746.5	-25.1	-31.7	-46.2	-63.1

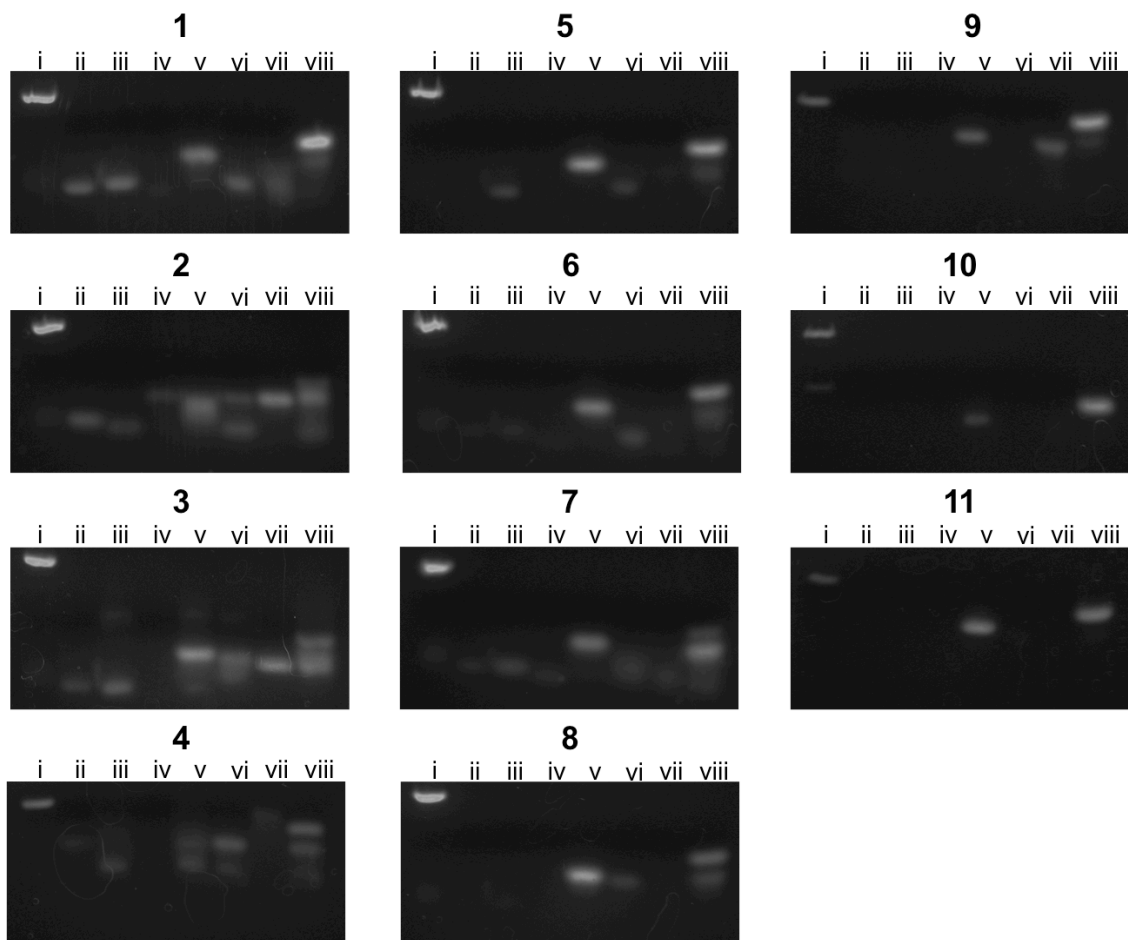


Figure 3 Gel mobility of RNA single strands, pairwise combinations, and 3WJs in TMS buffer. Gel mobility of 100 bp ladder (Lane i); individual strands 3WJa (Lane ii), 3WJb (Lane iii), and 3WJc (Lane iv); pairwise strands 3WJa + 3WJb (Lane v), 3WJb + 3WJc (Lane vi), and 3WJc + 3WJa (Lane vii); and strands 3WJa + 3WJb + 3WJc (Lane viii). 1: Phi29, 2: GA1, 3: SF5, 4: M2, 5: Phi29 Δ U29, 6: Phi29 Δ U29/ Δ U72, 7: Phi29 Δ U29/ Δ U72-73, 8: Phi29 Δ U29/ Δ U72-73-74, 9: Phi29 Δ U72, 10: Phi29 Δ U72-73, 11: Phi29 Δ U72-73-74. Assembly was performed in TMS buffer (50 mM Tris-HCl, pH 7.8, 100 mM NaCl, 10 mM MgCl₂) for the purpose of comparison to previous work published on the assembly and stabilities of various biological RNAs².

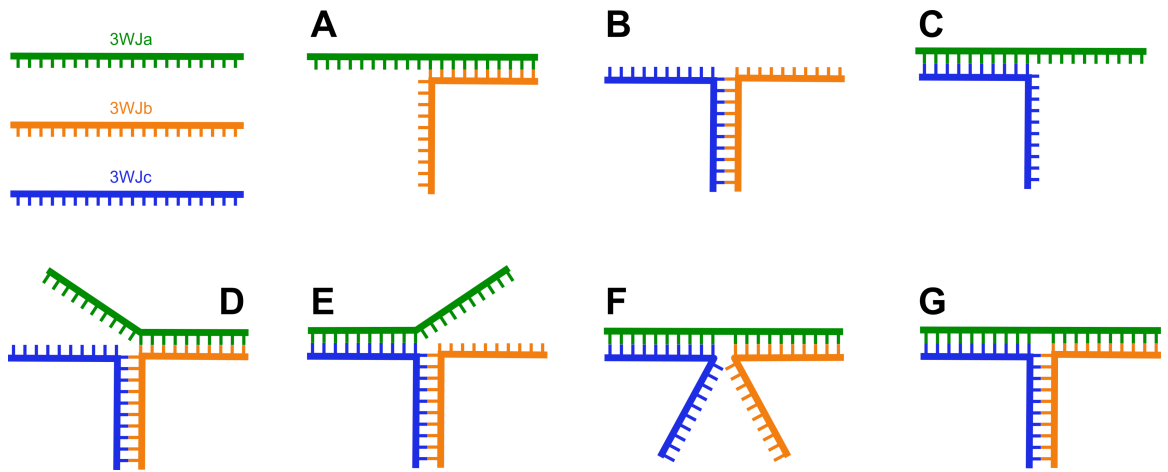


Figure 4 Possible species formed by strands 3WJa, 3WJb, and 3WJc pairwise (A, B, and C) and all together (D, E, F, and G).

Table 3 Calculated ΔG_{37} and ΔH values from the Nearest Neighbor Database² for possible species formed by phi29, SF5, and M2 strands 3WJa, 3WJb, and 3WJc (see Figure S4) compared to experimental values.

Species	Helices Formed	Phi29			SF5			M2		
		ΔG_{37} (kcal mol ⁻¹)	ΔH (kcal mol ⁻¹)	ΔG_{37} (kcal mol ⁻¹)	ΔH (kcal mol ⁻¹)	ΔG_{37} (kcal mol ⁻¹)	ΔH (kcal mol ⁻¹)	ΔG_{37} (kcal mol ⁻¹)	ΔH (kcal mol ⁻¹)	
A	Branch 1	-11.5	-82.7	-10.7	-76.3	-10.6	-76.4			
B	Branch 2	-10.7	-72.1	-10.7	-69.6	-13.8	-75.8			
C	Branch 3	-11.1	-80.3	-11.2	-77.4	-11.3	-76.9			
D	Branches 1 and 2	-20.8	-150.5	-20.2	-141.2	-23.7	-154.5			
E	Branches 2 and 3	-21.6	-150.4	-20.6	-145.4	-24.7	-152.6			
F	Branches 3 and 1	-22.0	-159.0	-21.0	-150.9	-21.0	-150.5			
G	Branches 1, 2, and 3	-27.5	-207.6	-26.8	-206.7	-30.4	-221.0			
Experimental Value	Branches 1, 2, and 3	-26.5	-230.8	-35.0	-336.1	-39.9	-350.7			

Table 3 Calculations for species A, B, and C include parameters for the formed helix, dangling ends, and one initiation penalty. Calculations for species D, E, and F include parameters for the formed helices, dangling ends, and two initiation penalties. The calculation for species G includes parameters for the formed helices, two initiation penalties, and a penalty for forming a 3-branch loop³⁻⁴. Formation of the 3WJ is favored when all three strands are present. As previously shown for RNA duplexes, even when the T_m for a single strand forming a self-complementary duplex is higher, the non-self-complementary duplex will form as long as the enthalpy for the non-self-complementary duplex is more favorable⁵.

Equation 1 Derivation of K_{eq} .

$$(1) K_{eq} = \frac{[ASC]}{[A][S][C]}$$

$$(2) C_T = \text{total strand concentration, } \alpha = \text{fraction in RNA triplex}$$

$$(3) K_{eq} = \frac{\frac{1}{2}C_T\alpha}{[\frac{1}{2}C_T(1-\alpha)]^2}$$

$$(4) K_{eq} = \frac{\frac{1}{2}C_T\alpha}{\frac{1}{4}C_T^2(1-\alpha)^2}$$

$$(5) K_{eq} = \frac{2\alpha}{C_T(1-\alpha)^2}$$

$$(6) \text{ At } T_m, \alpha = 0.5$$

$$(7) K_{eq} = \frac{2(0.5)}{C_T(0.5)^2}$$

$$(8) K_{eq} = \frac{2}{C_T}$$

References

1. Hill, A. C.; Schroeder, S. J., Thermodynamic stabilities of three-way junction nanomotifs in prohead RNA. *RNA* 2017.
2. Shu, D.; Shu, Y.; Haque, F.; Abdelmawla, S.; Guo, P., Thermodynamically stable RNA three-way junction for constructing multifunctional nanoparticles for delivery of therapeutics. *Nature Nanotechnology* 2011, 6, 658-667.
3. Turner, D. H.; Mathews, D. H., NNDB: The nearest neighbor parameter database for predicting stability of nucleic acid secondary structure. *Nucleic Acids Research* 2010, 38 (Database issue), D280-D282.
4. Laing, C.; Wen, D.; Wang, J. T. L.; Schlick, T., Predicting coaxial helical stacking in RNA junctions. *Nucleic Acids Research* 2011.
5. Schroeder, S. J.; Turner, D. H., Factors affecting the thermodynamic stability of small asymmetric internal loops in RNA. *Biochemistry* 2000, 39 (31), 9257-74.

Appendix II

Supplementary Information for “Preliminary Investigations of pRNA 3WJ Conformation Using Transmission Electron Microscopy”

Table 1 Diameters of 3WJs as determined by DLS.

3WJ	Mean Diameter (nm)	Polydisp. (%)	Intensity (%)	Mass (%)
Phi29	7.12 ± 2.29	32.19	100.00	100.00
GA1	5.74 ± 1.90	33.13	100.00	100.00
SF5	6.83 ± 2.31	33.82	100.00	100.00
M2	8.48 ± 3.18	37.54	100.00	100.00
Phi29 _{ΔU29}	5.56 ± 2.45	44.00	100.00	100.00
Phi29 _{ΔU29/ΔU72}	5.26 ± 2.28	43.31	100.00	100.00
Phi29 _{ΔU29/ΔU72-73}	5.09 ± 2.28	44.89	100.00	100.00
Phi29 _{ΔU29/ΔU72-73-74}	5.51 ± 1.98	35.88	100.00	100.00
Phi29 _{ΔU72} *	5.64 ± 4.21	74.62	100.00	100.00
Phi29 _{ΔU72-73} *	5.70 ± 5.53	97.04	100.00	100.00
Phi29 _{ΔU72-73-74}	5.21 ± 2.04	39.12	100.00	100.00
SF5 _{ΔG31}	7.00 ± 2.88	41.20	100.00	100.00
SF5 _{ΔG69}	6.37 ± 1.78	28.00	100.00	100.00
SF5 _{ΔG31/ΔG69}	6.01 ± 1.89	31.40	100.00	100.00
Phi29HE _{DNA}	41.90 ± 25.55	60.98	59.92	99.20

Table 1 Hydrodynamic sizes of 3WJs in standard melt buffer (1 M sodium chloride, 10 mM sodium cacodylate, 0.5 mM EDTA, pH 7.0) as determined by dynamic light scattering (DLS). Results represent means ± standard deviations. *Count rates for all 3WJs were between 100 – 500 kcps, with the exception of the phi29_{ΔU72} and phi29_{ΔU72-73} 3WJs, which were approximately 3 kcps. Results for these 3WJs therefore may not be statistically significant.

Table 2 Sequences for phi29HE_{DNA} 3WJ component strands 3WJa, 3WJb, and 3WJc.

Strand	Sequence
Phi29HE _{DNA} 3WJa	5' – TCCATATCAA CAGATCTGTA TTATGCCTCC TCACCTTAAC TAAAATATCA TCTTTCCGTA ATCCTATGAT GAATGTAGAA TGACAAGCCT CTAGAGCGTA <u>GCTTGTCATG TGTATGTTGC CCGGGGTACC</u> ACCGTACGGT CCTGTCCGAC TCGAATCTTG GCTGAACGGT ACTCGCGACA TCGCATACAA A – 3'
Phi29HE _{DNA} 3WJb	5' – TTTGTATGCG ATGTCGCGAG TACCGTTCAG CCAAGATTCG AGTCGGACAG GACCGTACGG TGGTACCCCG <u>GGCACATACT</u> <u>TTGTTGATAG GCGGGATCCC</u> CGGGAGGTCC ATCGCAACTG GGATTGAAAC CA – 3'
Phi29HE _{DNA} 3WJc	5' – TGGTTTCAAT CCCAGTTGCG ATGGACCTCC <u>CGGGGATCCC GCCTGTCAAT</u> <u>CATGGCAAGC TACGCTCTAG AGGCTTGTC</u> TTCTACATTC ATCATAGGAT TACGGAAAGA TGATATTTTA GTTAAGGTGA GGAGGCATAA TACAGATCTG TTGATATGGA – 3'

Table 2 Underlined nucleotides represent sequences in the previously designed phi29 3WJ.

Table 3 Predicted free energies for phi29HE_{DNA}.

Strand(s)	Predicted ΔG_{37} (kcal mol ⁻¹)
Phi29HE _{DNA} 3WJa	-28.7
Phi29HE _{DNA} 3WJb	-22.9
Phi29HE _{DNA} 3WJc	-20.5
Phi29HE _{DNA} 3WJa-3WJb	-136.6
Phi29HE _{DNA} 3WJb-3WJc	-90.5
Phi29HE _{DNA} 3WJc-3WJa	-153.1
Phi29HE _{DNA} 3WJa-3WJb-3WJc	-313.3

Table 3 Gibbs free energy predictions for phi29HE_{DNA} single strands, pairwise combinations, and 3WJ using RNA Structure ¹, where dashes indicate 5' – aaaa – 3' tetraloop linkers.

Table 4 Family and helical coaxial stacking predictions for 3WJs using Junction Explorer².

3WJ	3WJa-3WJb-3WJc		3WJb-3WJc-3WJa		3WJc-3WJa-3WJb	
	Family	Stacking Helices	Family	Stacking Helices	Family	Stacking Helices
Phi29	C	A/D	C	A/D	C	A/D
GA1	C	CE/D	C	A/CE	C	A/CE
SF5	C	CE/D	C	A/CE	A	CE/D
M2	C	CE/D	C	A/D	B	A/CE
Phi29 _{ΔU29}	C	A/CE	C	A/D	C	A/D
Phi29 _{ΔU29/ΔU72}	C	A/CE	C	A/D	C	A/D
Phi29 _{ΔU29/ΔU72-73}	C	A/CE	C	A/D	C	CE/D
Phi29 _{ΔU29/ΔU72-73-74}	C	A/CE	C	A/CE	C	CE/D
Phi29 _{ΔU72}	C	CE/D	C	A/D	C	A/D
Phi29 _{ΔU72-73}	C	CE/D	C	A/D	C	CE/D
Phi29 _{ΔU72-73-74}	C	CE/D	C	A/D	C	A/CE
SF5 _{ΔG31}	C	CE/D	C	A/CE	A	CE/D
SF5 _{ΔG69}	C	CE/D	C	A/CE	A	CE/D
SF5 _{ΔG31/ΔG69}	C	CE/D	C	A/D	C	A/CE
Phi29HE _{DNA}	C	A/D	C	A/D	C	A/D

Table 4 Predictions for each input sequence 5' – 3WJa-3WJb-3WJc – 3', 5' – 3WJb-3WJc-3WJa – 3', and 5' – 3WJc-3WJa-3WJb – 3' are provided, where dashes between strands 3WJa, 3WJb, and 3WJc indicate 5' – aaaa – 3' tetraloop linkers.

References

1. Mathews, D. H.; Disney, M. D.; Childs, J. L.; Schroeder, S. J.; Zuker, M.; Turner, D. H., Incorporating chemical modification constraints into a dynamic programming algorithm for prediction of RNA secondary structure. *Proceedings of the National Academy of Sciences of the United States of America* 2004, 101 (19), 7287-92.
2. Laing, C.; Wen, D.; Wang, J. T. L.; Schlick, T., Predicting coaxial helical stacking in RNA junctions. *Nucleic Acids Research* 2012, 40 (2), 487-498.